UNIVERSITÀ DELLA CALABRIA

DIPARTIMENTO DI INGEGNERIA INFORMATICA, MODELLISTICA, ELETTRONICA E SISTEMISTICA

DIMES

Dottorato di Ricerca in

Information and Communication Engineering for Pervasive Intelligent Environments

Ciclo

XXIX

Tesi di Dottorato

Design of back contact solar cells featuring metallization schemes with multiple emitter contact lines based on TCAD numerical simulations

Settore Scientifico Disciplinare: ING-INF/01 ELETTRONICA

Coordinatore:

Ch.mo Prof. Felice CRUPI

Tutor:

Ch.mo Prof. Felice CRUPI

Dottorando:

Marco V. GUEVARA G.

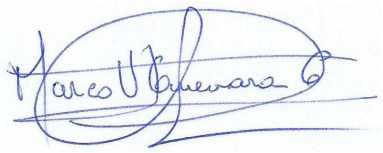

2017

Declaration of Authorship

I, Marco V. GUEVARA G., declare that this thesis titled, "Design of back contact solar cells featuring metallization schemes with multiple emitter contact lines based on TCAD numerical simulations" and the work presented in it are my own. I confirm that:

- This work was done wholly or mainly while in candidature for a research degree at this University.
- Where any part of this thesis has previously been submitted for a degree or any other qualification at this University or any other institution, this has been clearly stated.
- Where I have consulted the published work of others, this is always clearly attributed.
- Where I have quoted from the work of others, the source is always given. Except for such quotations, this thesis is entirely my own work.
- I have acknowledged all main sources of help.
- Where the thesis is based on work done by myself jointly with others, I have made clear exactly what was done by others and what I have contributed myself.

Signed: 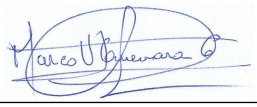

Date: 03/11/2017

"Vast Power of the Sun Is Tapped by Battery Using Sand Ingredient"

Front page headline, New York Times, 26 April 1954.

Abstract

Design of back contact solar cells featuring metallization schemes with multiple emitter contact lines based on TCAD numerical simulations

by Marco V. GUEVARA G.

The most hard-working goal within PV community is to design and manufacture devices featuring high-efficiency at low-cost with the better reliability as possible. The key to achieving this target is to optimize and improve the current fabrication processes as well as the layouts of the devices. TCAD modeling of PV devices turns out to be a powerful tool that lowers laboratory manufacturing costs and accelerates optimization processes by bringing guidelines of how to do it. The modeling in TCAD examines the designs before their implementation, accurately predicting its real behavior. When simulations are correctly calibrated, by changing simulations' parameters, allow finding ways to improve designs' parameters or just understand better the internal functioning of these devices. In this regard, this Ph.D. thesis fairly treats the electro-optical numerical simulations of interdigitated back-contact (IBC) c-Si solar cells, which nowadays is the architecture to which industry is trying to pull forward because of its numerous advantages. Among the benefits of this design are their improved efficiency due to the absence of front optical shading or the relative simplicity regarding their massive production.

The aim of this thesis, it is focusing on providing guidelines of the optimal design parameters of IBC solar cells, based on the state-of-the-art of advanced numerical simulations. Two main topics are treated, *(i)* the development of a simplified method to compute the optical profiles ten times faster than the traditional one and *(ii)* an extensive study on the impact of adding multiple striped metal contacts throughout the emitter region improving the efficiency by reducing the inner series resistance. It was performed a large number of ad-hoc calibrated simulations that sweep wide ranges of modeling parameters (i.e., changing geometric sizes, doping profiles, carriers' lifetimes, and recombination rates) to investigate their influence over the device operation, allowing to identify the most critical ones. This insight leads a better understanding of this kind of solar cells and helps to appraise ways to refine structures and enhance layouts of real devices for either laboratory or industry.

Sommario

Uno degli obiettivi principali nel settore fotovoltaico riguarda la progettazione e la produzione di dispostivi ad alta efficienza, massima affidabilità e basso costo. La chiave per raggiungere tale obiettivo è ottimizzare e migliorare i processi di fabbricazione attuali e le architetture usate per la realizzazione delle celle solari. In questo contesto, la modellazione TCAD dei dispositivi fotovoltaici rappresenta un potente strumento per accelerare i processi di ottimizzazione e ridurre allo stesso tempo i costi di testing e produzione. Difatti, esso consente di esaminare architetture innovative e avanzate di celle solari prima della loro implementazione. Pertanto, calibrando opportunamente il modello TCAD, è possibile comprendere in maniera più approfondita il funzionamento delle celle solari sotto esame e di conseguenza identificare adeguate strategie di ottimizzazione dei parametri di progetto. A tal proposito, la presente tesi è focalizzata sull'analisi e l'ottimizzazione di celle solari di tipo IBC (Interdigitated Back Contact) basate su substrati di silicio cristallino mediante simulazioni numeriche elettro-ottiche di dispositivo. Attualmente, le celle solari IBC rappresentano una tra le più promettenti architetture innovative per celle solari al silicio grazie all'elevata efficienza garantita e alla relativa semplicità di implementazione a livello industriale.

In particolare, lo scopo principale di questa tesi è quello di individuare e definire alcune linee guida per l'ottimizzazione delle celle solari IBC tramite l'utilizzo di simulazioni numeriche avanzate. Sono trattati due temi principali: *(i)* lo sviluppo di un metodo semplificato per la simulazione ottica del dispositivo fotovoltaico e *(ii)* un ampio studio sull'impatto dell'aggiunta di più contatti metallici a strisce nella regione di emettitore di una cella IBC. E' stato eseguito un numero elevato di simulazioni ad hoc, variando diversi parametri geometrici e/o di processo (ad esempio, le dimensioni dei contatti metallici, i profili di drogaggio, il tempo di vita dei portatori e i tassi di ricombinazione) al fine di analizzare il loro impatto sul funzionamento del dispositivo e quindi individuare quelli più critici. Dunque, l'analisi svolta in questa tesi consente una migliore comprensione del funzionamento delle celle solari di tipo IBC e fornisce un supporto per identificare soluzioni tecnologiche e architetturali migliorative finalizzate all'ottimizzazione dei dispostivi reali.

Acknowledgements

Firstly, I would like to express my sincere gratitude to my advisor Prof. Felice Crupi for the continuous support of my Ph.D. study and related research, for his patience, motivation, and immense knowledge. His guidance helped me in all the time of investigation and writing of this thesis. I could not have imagined having a better advisor and mentor for my Ph.D. study.
Besides my advisor, I would like to thank the Ecuadorian government, that through the SENESCYT, supported my research activities on both logistic and financially, as well as my accommodation during my stage in Italy. I thank my fellow lab mates in for the stimulating discussions, for the sleepless nights we were working together before deadlines, and for all the fun we have had in the last three years. Thanks for being part of this amazing experience: Paul Procel, Noemi Guerra, Silvio Pierro, Ramiro Taco, Vincenzo Maccaronio, Sebastiano Strangio, and Lorena Guachi. Of course. I cannot forget to mention Paul Romero, Eliana Acurio, Raffaele De Rose, and Prof. Marco Lanuzza. I also deeply thank my friend Paulina Aguirre for the company, and encouragement to keep moving forward.
Last but not the least, I would like to thank my lovely wife, for always laying beside me, even with an ocean of distance, *¡eres el amor de mi vida!*. Thank my dear family: my parents and to my brother and sister for always supporting me in everything throughout all my life ...

Marco

Contents

List of Figures

List of Tables

List of Abbreviations

1D	**One-Dimensional**
2D	**Two-Dimensional**
3D	**Three-Dimensional**
Ag	**Silver**
Al	**Aluminum**
AM1.5G	**Air Mass 1.5 Global Spectrum**
ARC	**Anti-Reflective Coating**
a-Si	**Amorphous Silicon**
BGN	**Band-Gap Narrowing**
BSF	**Back-Surface Field**
BSR	**Back Surface Reflection**
BTE	**Boltzmann Transport Equation**
CPV	**Concentrated Photovoltaics**
***c*-Si**	**Monocrystalline Silicon**
CVD	**Chemical Vapor Deposition**
Cz-Si	**Czochralski Silicon**
DESSIS	**Device Simulation for Smart Integrated Systems**
DD	**Drift-Diffusion**
DoE	**Design of Experiments**
EDA	**Electronic Design Automation**
FDTD	**Finite-Difference Time-Domain**
FEM	**Finite-Element Method**
FMM	**Fourier Modal Method**
FSF	**Front-Surface Field**
Fz-Si	**Float-zone Silicon**
GaAs	**Gallium Arsenide**
GHE	**Green House Effect**
GHGs	**Green House Gasses**
GISS	**Goddard Institute for Space Studies**
GISTEMP	**GISS Surface Temperature Analysis**
HE	**Homogeneous Emitter**
HOOP	**Highly-Doped**
I-V	**Current-Voltage**
LID	**Light-induced degradation**
LOOP	**Lowly-Doped**
LOTI	**Land-Ocean Temperature Index**
NASA	**National Aeronautics and Space Administration**
PECVD	**Plasma Enhanced Chemical Vapor Deposition**
PERC	**Passivated Emitter and Rear Cell**

PERL	**Passivated Emitter Rear Locally diffused**
POE	**Partial Differential Equation**
PV	**Photovoltaics**
QNR	**Quasi-Neutral Region**
RCWA	**Rigorous Coupled Wave Analysis**
RT	**Ray-Tracing**
SCAP1D	**Solar Cell Analysis Program, One-Dimensional**
SEM	**Scanning Electron Microscope**
Si	**Silicon**
Si0$_2$	**Silicon Dioxide**
SiN$_x$	**Silicon Nitride**
SQ	**Shockley-Queisser**
SRH	**Shockley-Read Hall**
SRV	**Surface Recombination Velocity**
TCAD	**Technology Computer Aided Design**
TMM	**Transfer Matrix Method**
USNW	**University of North South Wales**

Physical Constants

c_0	speed of light in vacuum	$(299\,792\,458\,\mathrm{m\,s^{-1}})$
ϵ_0	vacuum permittivity	$(8.854\,187 \times 10^{-12}\,\mathrm{A\,s\,V^{-1}\,m^{-1}})$
F	Faraday constant	$(96\,485.3365\,\mathrm{A\,s\,mol^{-1}})$
h	Planck constant	$(6.626\,069 \times 10^{-34}\,\mathrm{J\,s})$
k_B	Boltzmann constant	$(1.380\,649 \times 10^{-23}\,\mathrm{J\,K^{-1}})$
μ_0	vacuum permeability	$(4\pi \times 10^{-7}\,\mathrm{V\,s\,A^{-1}\,m^{-1}})$
q	elementary charge	$(1.602 \times 10^{-19}\,\mathrm{C})$
σ	Stefan-Boltzmann constant	$(5.670\,373 \times 10^{-8}\,\mathrm{W\,m^{-2}\,K^{-4}})$
Z_0	impedance of free space	$(367.7\,\Omega)$

List of Symbols

$\alpha(\lambda)$	Absorption coefficient	cm^{-1}
$\Delta\eta$	Efficiency variation	$\%_{abs}$
Δn	Variation electron density	cm^{-3}
Δp	Variation hole density	cm^{-3}
ε	Electromagnetic permittivity	$\mathrm{F\,cm}^{-1}$
ξ	Electric field intensity, or correlation length	$\mathrm{V\,m}^{-1}$ or µm
ξ_m	Maximum electric field intensity	$\mathrm{V\,m}^{-1}$
η	Power conversion efficiency	%
η_c	Quantum collection efficiency	%
θ	Angle of incidence of the radiation	°
λ	Wavelength	nm
μ_n	Electron mobility	$\mathrm{cm}^2\,\mathrm{V}^{-1}\,\mathrm{s}^{-1}$
μ_p	Hole mobility	$\mathrm{cm}^2\,\mathrm{V}^{-1}\,\mathrm{s}^{-1}$
ρ	Charge density	$\mathrm{C\,cm}^{-3}$
ρ_c	Specific contact resistivity	$\Omega\,\mathrm{cm}^2$
ρ_m (or ρ_f)	Metal finger resistivity	$\Omega\,\mathrm{cm}$
σ_A	Standard deviation of the finger cross-section	$\mu\mathrm{m}^2$
σ_H	Standard deviation of the finger height	µm
σ_n	Electron capture cross-section	cm^2
σ_p	Hole capture cross-section	cm^2
φ	Electrostatic potential	V
φ_0	Built-in electrostatic potential	V
$\Phi(\lambda)$	Incident photon flux	$\mathrm{s}^{-1}\,\mathrm{cm}^{-2}$
Φ_b	Barrier height at metal/semiconductor interface	eV
Φ_F	Fermi potential	V
Φ_n	Quasi-Fermi potential for electrons	V
Φ_p	Quasi-Fermi potential for holes	V
T_{Bulk}	Bulk minority carrier recombination lifetime	s
τ_{eff}	Effective minority-carrier recombination lifetime	s
τ_n	Recombination lifetime for electrons	s
τ_p	Recombination lifetime for holes	s
ν	Frequency	s^{-1}
χ	Electron affinity	eV
$A(\lambda)$	Absorbance	%
A_m	Finger cross-section area	$\mu\mathrm{m}^2$
B	Radiative recombination coefficient	$\mathrm{cm}^3\,\mathrm{s}^{-1}$
CF_{rear}	Rear contact fraction	%
C_n	Auger coefficient for electrons	$\mathrm{cm}^6\,\mathrm{s}^{-1}$
C_p	Auger coefficient for holes	$\mathrm{cm}^6\,\mathrm{s}^{-1}$
C_{peak}	Peak surface doping concentration	cm^{-3}
D_n	Electron diffusion coefficient	$\mathrm{cm}^2\,\mathrm{s}^{-1}$
D_p	Hole diffusion coefficient	$\mathrm{cm}^2\,\mathrm{s}^{-1}$
D_{sub}	Wafer thickness	µm
E_C	Conduction band edge energy	eV
E_F	Fermi level	eV
E_{Fn}	Quasi-Fermi level for electrons	eV
E_{Fp}	Quasi-Fermi level for holes	eV

E_g	Energy band-gap	eV
$E_{g,eff}$	Effective energy band-gap	eV
$E_{ph}(\lambda)$	Photon energy	eV
$EQE(\lambda)$	External quantum efficiency	$\%$
E_V	Valence band edge energy	eV
F	Finger area factor	*num.*
F_n	Geometric factor for electrons	*num.*
F_p	Geometric factor for holes	*num.*
FF	Fill factor	$\%$
G	Net generation rate	$\mathrm{cm^{-3}\,s^{-1}}$
G_{opt}	Optical generation rate	$\mathrm{cm^{-3}\,s^{-1}}$
H_{bb}	Busbar height	$\mu\mathrm{m}$
H_{fm} (or H_m)	Front finger height	$\mu\mathrm{m}$
I_{in}	Incident solar irradiance	$\mathrm{W\,m^{-2}}$
$IQE(\lambda)$	Internal quantum efficiency	$\%$
J_0 (or $J_{0,tot}$)	Saturation current density	$\mathrm{A\,cm^{-2}}$
$J_{0,b}$	Base saturation current density	$\mathrm{A\,cm^{-2}}$
$J_{0,BSF}$	BSF saturation current density	$\mathrm{A\,cm^{-2}}$
$J_{0,e}$	Emitter saturation current density	$\mathrm{A\,cm^{-2}}$
$J_{0,min}$	Minimum saturation current density	$\mathrm{A\,cm^{-2}}$
J_{depth}	Junction depth	$\mu\mathrm{m}$
J_{in}	Incident photon current density	$\mathrm{A\,cm^{-2}}$
J_L (or J_{ph})	Photogenerated current density	$\mathrm{A\,cm^{-2}}$
J_{mpp}	Current density at maximum power point	$\mathrm{A\,cm^{-2}}$
J_n	Electron current density	$\mathrm{A\,cm^{-2}}$
J_p	Hole current density	$\mathrm{A\,cm^{-2}}$
J_{sc}	Short-circuit current density	$\mathrm{A\,cm^{-2}}$
$J_{sc,max}$	Maximum short-circuit current density	$\mathrm{A\,cm^{-2}}$
κ_{lambda}	Extinction coefficient (imaginary part of the refractive index)	*num.*
k	Boltzmann constant	$\mathrm{J\,K^{-1}}$
L_{bb}	Busbar length	cm
L_{fm} (or L_m)	Front finger length	cm
L_n	Diffusion length for electrons	cm
L_p	Diffusion length for holes	cm
L_T	Transport length	cm
m_e^*	Effective mass for electrons	g
m_p^*	Effective mass for holes	g
n	Electron concentration	$\mathrm{cm^{-3}}$
$\tilde{n}$	Complex refractive index	*num.*
$\tilde{n}_\lambda$	Real part of the complex refractive index	*num.*
n_i	Intrinsic carrier density	$\mathrm{cm^{-3}}$
$n_{i,eff}$	Effective intrinsic carrier density	$\mathrm{cm^{-3}}$
n_{n0}	Electron equilibrium concentration in n-type semiconductors	$\mathrm{cm^{-3}}$
n_{p0}	Electron equilibrium concentration in p-type semiconductors	$\mathrm{cm^{-3}}$
N_A	Acceptor density	$\mathrm{cm^{-3}}$
N_C	Effective density of states in the conduction band	$\mathrm{cm^{-3}}$
N_D	Donor density	$\mathrm{cm^{-3}}$
N_{dop}	Net doping density	$\mathrm{cm^{-3}}$
N_s	Surface doping concentration	$\mathrm{cm^{-3}}$
$N_{s,chem}$	Chemical surface doping concentration	$\mathrm{cm^{-3}}$
N_{sub}	Substrate doping density	$\mathrm{cm^{-3}}$
N_t	SRH trap density	$\mathrm{cm^{-3}}$
N_V	Effective density of states in the valence band	$\mathrm{cm^{-3}}$
p	Hole concentration	$\mathrm{cm^{-3}}$
P_{in}	Incident solar power	$\mathrm{W\,cm^{-2}}$
P_{mpp}	Maximum output power	$\mathrm{W\,cm^{-2}}$
P_{n0}	Hole equilibrium concentration in n-type semiconductors	$\mathrm{cm^{-3}}$

P_{p0}	Hole equilibrium concentration in p-type semiconductors	cm^{-3}
q	Electronic charge	C
R	Net recombination rate	$\mathrm{cm}^{-3}\,\mathrm{s}^{-1}$
$R(\lambda)$	Reflectance	%
R_b	Bulk semiconductor resistance	Ω
R_{bb}	Resistance of the front busbars	Ω
R_{bc}	Back contact resistance	Ω
R_{ch}	Characteristic resistance of a solar cell	Ω
$R_{ext,front}$	External front reflectivity	*num.*
R_{fc}	Front contact resistance	Ω
$R_{fm}(or R_m)$	Resistance of the front metal fingers	Ω
$R_{int,back}$	Internal back reflectivity	*num.*
$R_{int,front}$	Internal front reflectivity	*num.*
R_s	Series resistance	Ω
R_{sh}	Shunt resistance	Ω
R_{sq}	Emitter sheet resistance	$\Omega \cdot sq^{-1}$
S	Interruption size	µm
S_n	Surface recombination velocity for electrons	$\mathrm{cm}\,\mathrm{s}^{-1}$
S_p	Surface recombination velocity for holes	$\mathrm{cm}\,\mathrm{s}^{-1}$
$SR(\lambda)$	Spectral response	$\mathrm{A}\,\mathrm{W}^{-1}$
ν_{oc}	Normalized open-circuit voltage	*num.*
t	Time	s
$T(\lambda)$	Transmittance	%
T	Temperature	K
V_a	Applied bias voltage	V
V_{mpp}	Voltage at maximum power point	V
Voc	Open-circuit voltage	V
ν_{oc}	Normalized open-circuit voltage	*num.*
ν_{th}	Thermal velocity	$\mathrm{cm}\,\mathrm{s}^{-1}$
W_{bb}	Busbar width	mm
W_{fm} (or W_m)	Front finger width	µm
W_{se}	Lateral width ofthe SE diffusion	µm
W_{sub}	Front contact pitch	µm
W_{wafer}	Wafer width	cm
χ_F	Interruption position	µm
ω	angular frequency	rad

To Cristina, my lovely wife...

Chapter 1

Introduction and research objectives

1.1 Introduction

The irradiation from the Sun to Earth's surface is about $1368\,\mathrm{W\,cm^{-2}}$, which is as much power as about twenty-three 60-watt light bulbs per square meter that results in $3800\,\mathrm{TW}$ in the exposed Earth's area to the Sun. It is more than 300 times the power produced by gas, coal, and other fossil's fuels at the same time, [1]. Besides, the solar generation is a low-carbon technology with a broad scalability range, e.g., small stand-alone devices like small calculators or large-scale energy production plants like Longyangxia Dam Solar Park with $320\,\mathrm{MW}$ PV in China. Therefore, massive expansion of global solar generating capacity to multi-terawatt scale is so likely an essential component of a workable strategy to mitigate climate change. In recent years, there has seen rapid growth in installed solar generating capacity, advances in materials, fabrication technology, and price reduction. Nonetheless, further advances are needed to enable an increasing contribution to solar power generation. Solar energy technology requires become cost-competitive compared with fossil generation, and, of course, it also needs the governments all around the world encourage their use, for example, by applying local policies and tax reduction to use of photovoltaic devices.

1.1.1 Progress review of *c*-Si solar cells

In a very brief history revision of solar cells, the early years date back to 1939 when the physic French Alexandre-Edmond Becquerel observed the dependence of voltage between two plates immersed into an electrolyte to the illumination intensity. After few years, Otmar Geisler patented the first "light sensitive device" in 1941 [2], but it was not until 1954 that formally began the solar cells development research [3]. The first design proposals of solar cells were developed and introduced into the early days of the photovoltaic

(PV) community, which, since then, always is looking for bettering the conversion efficiencies (η) of solar cells devices and make them industrially viable with a cost-effective manufacturing. During three years, i.e. 1958, 1959 and 1960, Hoffman Electronics presented commercial PV cells with 9%, 10%, and 14% efficiencies each year, every time improving the manufacturing process. In 1975, R.J. Schwartz started the study of full back-contacted cells, as an alternative to cells with contacts on front and back [4]. In 1985, the Center for Photovoltaic Engineering at the University of New South Wales (UNSW) presented silicon cells with efficiencies rounding the 20%, and 14 years later the same research center announced, in 1999, a world record efficiency for *c*-Si cells with a verified efficiency of 25% [5, 6]. In 2014, almost simultaneously but independently, Panasonic and SunPower crossed the 25% efficiency threshold with revised efficiencies of 25.6% [7] and 25.0% [8], respectively, both using industrially-sized silicon wafers. In September 2016, Kaneka Corporation achieved, in the called NEDO project, the current world's highest conversion efficiency ever seen in a solar cell with 26.33%, in a practical size (180 cm^2) of crystalline silicon (*c*-Si) [9].

Device	Area [cm^2]	V_{OC} [mV]	J_{SC} [mA/cm^2]	FF[%]	η [%]	Test Center (Date)	Reference
Ideal, 110 µm-thick		761	43.3	89.3	29.4	Modeled	[10]
Kaneka IBC HIT	180.43 (da)	744	42.3	83.8	26.3	FhG-ISE (7/16)	[9]
Panasonic IBC HIT	143.7 (da)	740	41.8	82.7	25.6	AIST (2/14)	[7]
SunPower IBC	153.5 (ta)	737	41.3	82.7	25.2	Fraunhofer ISE (10/15)	[11]
Kaneka SHJ	151.9 (ap)	738	40.8	83.5	25.1	Fraunhofer ISE (9/15)	[12]
Fraunhofer ISE TOPCon	4.0 (da)	718	42.1	83.2	25.1	Fraunhofer ISE (8/15)	[13, 14]
UNSW PERL (*p*-type)	4.0 (da)	706	42.7	82.8	25.0	Sandia(3/99)	[5, 15]
Panasonic HIT	101.8 (ta)	750	39.5	83.2	24.7	AIST (12/12)	[16]
EPFL MoOx SHJ	3.9 (ap)	725	38.6	80.4	22.5	Fraunhofer ISE (2015)	[17]
IMEC PERT (*n*-type)	238.9 (ta)	695	40.2	80.5	22.5	Fraunhofer ISE (2015)	[18, 19]
Trina solar mono-Si PERC (*p*-type)	243.7	680	40.5	80.3	22.1	Fraunhofer ISE (2015)	[11]

TABLE 1.1: Performance parameters of certified *c*-Si solar cells.
(*da: Designated area, *ta: Total area, *ap: Aperture area)

Compared to other PV technologies, silicon solar cells have the advantage of using a photoactive absorber material that is abundant on Earth, stable, nontoxic, and well understood. Silicon has an energy band gap of 1.12 eV, corresponding to a light absorption cut-off wavelength rounding 1.16 µm. This band gap matches pretty well with the solar spectrum, and it is near to the optimum value for solar-to-electric energy conversion using a single semiconductor optical absorber. Only considering the radiative recombination mechanism inside the semiconductor (the so-called detailed balance) [20], the theoretical limit of conversion efficiency for a semi-infinitely thick silicon solar cell is 33.5 % at 25° [21].

Silicon was one of the first semiconductors in which very accurate optical measurements of the band gap were obtained. An investigation field called *"silicon photonics"* was responsible for the in-depth study of everything related to the optical properties of this material [22]. The interest of these studies came from the idea to provide to any electronic device, in a single manufacturing process, the ability to generate or sense light by using silicon as an optical medium. According to the studies of silicon photonics, it was shown that silicon is an indirect bandgap semiconductor, i.e., the minimum of the

conduction band does not occur at the same wave vector as the maximum of the valence band. It implies that it has an inefficient radiative recombination, which, for defect-free material, the photogenerated electrons and holes can exhibit very long lifetimes. In fact, rather than its radiative equivalent, the intrinsic Auger recombination is the dominant recombination mechanism in silicon (on ideally defect-free devices). Auger recombination refers the case in which an electron recombines with a hole by transferring their energy difference to a third charge carrier, either a second free electron or hole, which later dissipates the acquired energy as heat. Further, because of its indirect band gap, silicon also has a relatively small light absorption coefficient compared to other materials. However, silicon wafers featuring texturing in the surface, combined with the use of well-designed anti-reflection coatings and rear surface mirrors, efficient light absorption, including the infrared part of the solar spectrum, is possible even with comparatively thin-wafers ($\sim$100 $\sim$150 nm) [10].

The work reported by Richter et al. in [10], purely based on an empirical parameterization of experimental measurements of both radiative and Auger recombination rates [23], calculates the intrinsic efficiency-limit for conversion energy of a silicon solar cell, featuring a (110 µm-thick substrate of undoped silicon, in 29.4 %, by considering Lambertian light-trapping [24]. This value is significantly lower than the detailed balance limit (33.5 %) [20]. Regarding efficiencies of real solar cells, Fig. 1.1 shows a comparison of the *J-V* curves of the actual world record efficiency solar cell, developed by Kaneka, which features most of the currently advanced improvements in the PV field, with the ideal defect-free solar cell mentioned above.

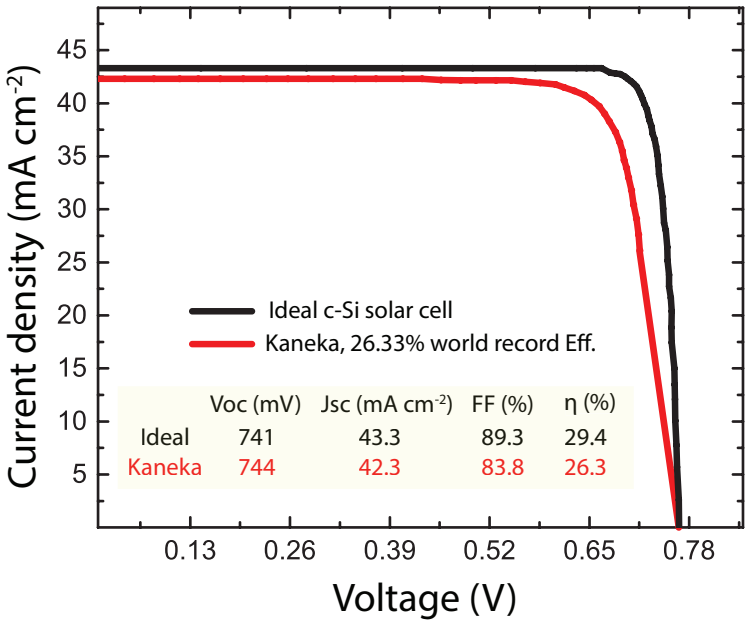

FIGURE 1.1: *J-V* curves of ideal solar cell simulation (*black* line) [10], and current world's record efficiency solar cell using heterojunction IBC technology (by Kaneka) (*red* line) [9].

1.1.2 Passivation and charge extraction techniques

A perfect solar cell device has not yet been created, i.e., one that is entirely free of manufacturing imperfections or recombinations inside. It is well known that most of these recombinations, of photo-excited electron-hole pairs, occur at surfaces and interfaces of the devices. Therefore, there are a lot of efforts to incorporate, to the future generations of high-efficiency solar cells, low-cost techniques for producing semiconductor/dielectric interfaces with the lowest possible recombination rates. The metal/silicon interfaces contribute adversely with recombinations but are necessary to extract the generated charges from the device. Currently, there are many efforts for developing carrier-selective passivating contacts based on tunneling to mitigate the losses and efficiently take-out the photogenerated charges [25].

In practice, in silicon substrates, the recombination of carriers in silicon devices is affected or even dominated by either the presence of crystallographic defects or undesirable external impurities. Nevertheless, nowadays thanks to improvements in silicon ingot growth processes, most of the crystallographic defects are eliminated, and due to contamination control during fabrication, the bulk electronic quality of crystalline silicon wafers reached to such a point that further device advances now rely on interface passivation, carrier-selective contact structures, and tunnel oxide contacts.

The primary purpose of surface passivation is to keep the surface recombination as low as possible by the deposition/growth of appropriate passivation-films on the semiconductor surface or by immersing the sample into polar liquids [26–28]. The process of passivation what it does is to eliminate the harmful surface defects [29–32], which are predominantly broken silicon-silicon bonds, called dangling bonds, or by modifying the relative concentration of photogenerated carriers near to the silicon edges [33, 34].

Among the useful materials, employed to create thin passivation layers are some dielectrics such as silicon oxide [33, 35–39], silicon nitride [40–43], silicon carbide [44, 45], and aluminum oxide [26, 46–48]. Other used materials are semiconductors with a disordered structure like intrinsic hydrogenated amorphous silicon [49, 50] or others discussed in [51]. The passivation layers cannot extract carriers for itself, as they are either insulating or insufficiently conductive. To obtain the photogenerated carriers efficiently to the external metal terminals it is required two-carrier-selective contact structures. Ideally, these inner structures exhibit efficient transport of only one type of carrier (e.g., electrons) while hindering the transport (i.e., blocking) of the other type of carrier (e.g., holes).

The recombination mechanism process requires the interaction of both types of carriers, hindering the transport of one of them reduces the recombination probability in the device. Nevertheless, to suppress recombination more efficiently, it is necessary to place over the structure an inter-facial passivation layer. Therefore, a highly-selective contact presents simultaneously high

conductivity for just one of the two carriers while minimizing the recombination rate. In the design of high-efficiency solar cells, it is possible chose to cover most of the wafer surface with a passivation dielectric material and extract photogenerated carriers selectively by local openings in the insulator [5] or depositing carrier-selective materials on the full wafer surface using a proper interface-passivation strategy. In the latter approach, the two simultaneous requirements of surface passivation and preferential conduction are frequently achieved using a stack of two or more layers, for example, intrinsic and doped hydrogenated amorphous silicon, as in silicon heterojunction solar cell technology [52–54]. It is important carefully select the required material for contact formation considering the optical properties of each material. Indeed, layers blanket-deposited on the wafer surfaces (either for interface passivation or selective transport) should also maximize light coupling into the silicon absorbing by minimizing reflection and parasitic absorption losses. In fact, developing contact layers that satisfy these electronic and optical requirements simultaneously is the key for high-efficiency solar cells.

1.2 Basic operation and performance indicators of solar cells

To better understanding the challenge of fabricating high-efficiency PV cells, it is important to start from the basics of its structure. For this, results useful to consider the solar cell in its most fundamental form, i.e., as a semiconductor with a given energy band gap and electron- and hole-selective regions that secure the inner charge-carrier separation prepared in a way that allows a consequent charge extraction. When the sunlight strikes the surface and passes inside the semiconductor, photons, with higher energy than the band gap, are absorbed, giving to electrons the enough energy to move from the valence band to the conduction band. The transition of electrons from one band to the other, leaves an equal number of holes in the valence band which leads a large difference in total electron- and hole- concentrations (n and p) under illumination and the thermo-chemical equilibrium in dark conditions (n_0 and p_0, with $n_0 p_0 = n_i^2$, where n_i is the intrinsic carrier density which is equal to 9.7×10^9 cm at 300 K for silicon [55, 56]).

The total electric current results of the negative (electrons), and positive (holes) charge carriers transport in opposite directions within the device. In the quasi-neutral device regions, the excess carrier densities ($\Delta n = n - n_0$, and $\Delta p = p - p_0$) are approximately the same, $\Delta n \approx \Delta p$. Similarly to equilibrium, in which the Fermi energy (E_F) describes the carrier populations, in non-equilibrium conditions the electron and hole quasi-Fermi energies E_{Fn} and E_{Fp} depict the carrier populations [57].

$$n = n_0 + \Delta_n = N_C \exp\left(\frac{E_{Fn} - E_C}{k_B T}\right) \tag{1.1}$$

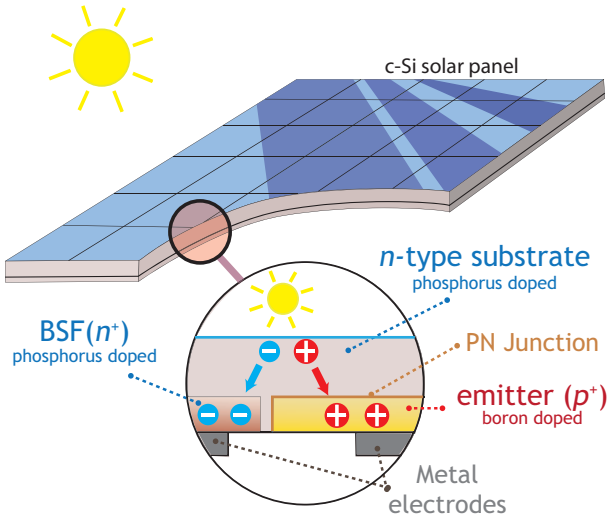

FIGURE 1.2: General sketch of a *c*-Si solar panel, featuring both contacts at the rear part, illustrating the idea of separate the generated charges.

$$p = p_0 + \Delta_p = N_V \exp\left(\frac{E_V - E_{Fp}}{k_B T}\right) \tag{1.2}$$

Where E_C and E_V represent the energetic positions of the conduction band minimum and the valence band maximum. The parameters represented by N_C and N_V are the effective density of states in the conduction and valence band respectively, k_B is the Boltzmann constant, and T is the semiconductor temperature. The difference between the electron and hole quasi-Fermi energies, which is equal to the sum of the electrochemical potential of an electron E_{Fn} and the electrochemical potential of a hole E_{Fp}, determines the maximum voltage V that the solar cell can provide, [57]:

$$V \equiv \frac{E_{Fn} - E_{Fp}}{q} = \frac{k_B T}{q} \ln\left(\frac{np}{n_0 p_0}\right) \tag{1.3}$$

where q is the elementary charge.

1.2.1 Working under illumination conditions

In steady-state illumination, the photogenerated charge carriers leave the device in the form of electric current through two low-resistance selective contacts, one for the electrons and other for the holes. Under open-circuit conditions, the level of carriers gathers, so that the recombination rate perfectly counterbalances the photogeneration rate. As in Eq. 1.3, such large concentration of carriers produces the maximum voltage measured across the cell electrodes, the so-called open-circuit voltage (V_{OC}). The highest current is at short circuit (zero voltage) when the concentration of carriers inside the

device and, therefore, the recombination rates are relatively small. The electrons and holes flow out to the metal contacts, even when there is not a tension between electrodes, neither concentration of carriers nor a difference in the quasi-Fermi energies. In good solar cells, the short circuit current density J_{SC} is only slightly lower than the number of photons absorbed in the semiconductor per-unit-time and area, multiplied by the elementary charge, which can be called the photogenerated current density J_{ph}. The ratio between J_{SC} and J_{ph} is an indicator of the *"collection efficiency"*, i.e., the rate of electrons that comes out and the photons going inside the cell. This quantum collection efficiency is usually a function of the wavelength, or energy, of the incident photons. Ideally, for silicon, with its bandgap of $1.12\,\mathrm{eV}$, the highest J_{ph} value for an $110\,\mu\mathrm{m}$-thick wafer is $43.3\,\mathrm{mA\,cm^{-2}}$ under standard test conditions (STC). In a real device, the currently maximum J_{SC} reached is $42.3\,\mathrm{mA\,cm^{-2}}$, (Table 1.1).

A solar cell, in working conditions, delivers electric power with a particular voltage and current density. The total output current density could be expressed as $J_{out} = J_{ph} + J_{eq} - J_{rec}$, where the photogenerated current density(J_{ph}) was defined as the net cumulative generation in excess of the equilibrium thermal generation, represented by (J_{eq}). The recombination current density, (J_{rec}), refers to all generated-carriers not collected per unit time and area. The recombination of charges originates from the higher concentration of electrons and holes required to deliver voltage, compared to short circuit, (see Eq. 1.3).

In Fig. 1.3, two *J-V* characteristic curves are sketched, each one representing the working of a solar cell under dark and illuminated conditions. Both curves illustrate the superposition principle, which says that the illuminated *J-V* of the *pn* junction is the same as the dark *J-V*, but it is shifted down by the photogenerated current density J_{ph}. The detailed derivation of the photogenerated current density of the pn junction is well described in [58].

1.2.2 Loss mechanisms

The most fundamental loss mechanism in semiconductors is the radiative band-to-band recombination, which is the inverse process of absorption. An efficient external luminescence due to radiative recombination is a characteristic of high-efficiency solar cells [59, 60], because it indicates low internal optical losses. The radiative recombination is proportional to the concentrations of the two "reactant species", i.e., to the *pn* product of the concentrations of holes and electrons, [57]. The proportionality constant is called the band-to-band recombination coefficient, which for silicon is $B = 4.73 \times 10^{-15}\,\mathrm{cm^3\,s^{-1}}$ at $300\,\mathrm{K}$ [61]. Although, as mentioned in previous sections, radiative recombination is not the dominant recombination mechanism in silicon, focusing on it helps to elucidate the basic operation principles of solar cells. Therefore, using Eq. 1.1 and Eq. 1.2, the total band-to-band recombination current

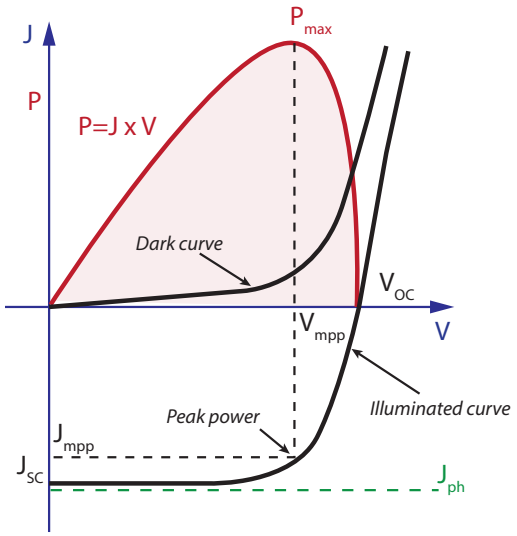

FIGURE 1.3: *J-V* characteristics of a *pn* junction in the dark and under illumination.

density of a silicon wafer, featuring certain thickness *W* could be expressed as:

$$J_{rec} = q \cdot B \cdot pn = q \cdot W \cdot B \cdot n_i^2 \exp\left(\frac{E_{Fn} - E_C}{k_B T}\right) \tag{1.4}$$

In equilibrium, Eq. 1.4 simplifies to:

$$J_{eq} = q \cdot B \cdot p_0 n_0 = q \cdot W \cdot B \cdot n_i^2 \tag{1.5}$$

Then, the output current density of the solar cell would be written as:

$$J_{out} = J_{ph} - q \cdot W \cdot B \cdot n_i^2 \left[\exp\left(\frac{E_{Fn} - E_C}{k_B T}\right) - 1\right] \tag{1.6}$$

Equation 1.6 relates the output current density with the sum of the electrochemical potentials of electrons and holes. These electrochemical potentials are responsible for the existence of an output voltage, and their gradients correspond to the driving forces that cause the movement of charges [57]. Furthermore, Eq. 1.6 shows that the output current density has a link with the *pn* product (see Eq. 1.3), which means that have a relationship with the recombinations.

As mentioned above, there is a non-zero difference between the quasi-Fermi energies, even in short-circuit conditions, and this makes $J_{SC} \leq J_{ph}$. In practice, the potential between the cell terminals is the measure what characterized the solar cell, but it is smaller than $(E_{Fn} - E_{Fp})/q$. Hence, from Eq. 1.6 is possible derive an expression to describe the solar cell is:

$$J_{out} = J_{SC} - J_0 \left[\exp\left(\frac{qV}{nk_BT}\right) - 1 \right] \tag{1.7}$$

where, in the case of band-to-band recombination, the exponential factor J_0 is given by Eq. 1.5. It is usually referred to as saturation current density in the dark, with the ideality-factor equal to 1. Additionally, it could say that J_0 represents the generation-recombination current per unit area that takes place in thermal equilibrium, hence the subscript 0.

The exponential dependence of the current density on voltage directly derives from the fact that Fermi–Dirac statistics govern the concentrations of electrons and holes. Reason why, many different types of solar cells display qualitatively very similar *J-V* characteristics curves, independent of the absorber materials and carrier extraction schemes[62]. For simplicity, the concentrations are usually approximated by Boltzmann statistics, i.e., by an exponential dependence of the sum of the electrochemical potentials of an electron and a hole, which eventually translates into a voltage.

Although the above derivation comes from the band-to-band radiative mechanism deduction, in silicon, it is important considering other contributing processes to J_0. Such is the case of both Auger and defect-assisted recombination mechanisms. These recombinations are also dependents on the *pn* product. Indeed, real devices are usually dominated by non-radiative recombination. The Auger recombination mechanism involves three carriers, even though its result is to annihilate one free electron and one free hole. In principle, Auger recombination is proportional to the *pn* product multiplied by the concentration of the majority carriers, p or n, but in practice, it deviates slightly from an ideal p^2n (or n^2p) dependence due to the Coulombic interaction between carriers [23, 63]. Defect-assisted, or Shockley–Read–Hall [64, 65], recombination is a two-particle process that can have a complex dependence on the carrier concentrations themselves and the properties of the defects. Including these additional recombination losses into the solar cell, equation requires adapting the J_0 factor and the ideality factor n, which can become either smaller or greater than one [66]. Usually, J_0 and n are determined experimentally [67], and their values may reflect a combination of several mechanisms. Small values of J_0, implying fewer recombination, and low values of n are desired for high-efficiency solar cells.

1.2.3 Typical electrical indicators of solar cells

The maximum power-generation of a solar cell occurs when there is an optimal trade-off between the current flowing out of the device (low as possible recombination), and voltage in the device terminals (higher as possible the carrier concentration). This optimum operating circumstance, it was defines the so-called maximum power point (mpp), which is associated with the values of J_{mpp} and V_{mpp} in Fig. 1.3. The fill factor (*FF*), on the other hand, is

the ratio between the maximum power ($P_{max} = J_{mpp}V_{mpp}$) generated by a solar cell and the product of V_{OC} with J_{SC}. The *FF* indicates what fraction of the separate highest current J_{SC} and voltage V_{OC} can be delivered simultaneously by the solar cell.

$$FF = \frac{J_{mpp} \cdot V_{mpp}}{V_{OC} \cdot J_{SC}} \cdot 100\% \tag{1.8}$$

Ideally, considering only the intrinsic-recombination processes, i.e., Auger and radiative recombinations, the theoretical maximum value of the *FF* of a silicon solar cell is 89.3% [10]. In real devices, the actual record of highest *FF* was reached by Kaneka with 83.8%, see Table 1.1. By using an improved substrate with excellent minority carrier lifetimes and a reduced series resistance [68]. Commonly, the *FF* is adversely affected by other internal recombination losses and external shunts, but it is further lowered by the resistive losses caused by the charge transport through materials with finite conductivity (cross-sectional area), or across interfaces between different materials (e.g., contact resistance at metals-semiconductors interfaces). These effects are represented electrically as two resistances a lumped series and a shunt, R_s and R_{sh}, respectively, which can be incorporated into an expanded form of Eq. 1.7. The resistive losses are typically harsher than shunts and can be intensified by poor cell designs, [69]. An accurate evaluation of the R_s parameter [70] is essential in high-efficiency solar cell development [71].

The delicate balance, between the parameters described above, is determined by the power conversion efficiency $\eta = V_{OC} \cdot J_{SC} \cdot FF$, which is typically measured with a solar radiation simulator under STC for terrestrial applications, i.e., air mass 1.5 Global Spectrum ($1000\,\mathrm{W\,cm^{-2}}$ at $300\,\mathrm{K}$) [72]. The efficiency is the most critical parameter at the time to characterizing a PV device. Fundamentally, it refers to the portion of energy, in the form of sunlight, that a solar cell can transform into electricity.

1.3 Solar cell structure, performance modeling and simulation approach

1.3.1 Silicon substrates

For many years, due to some historical and technological factors, the fabrication of commercial homojunction solar cells has been in *p*-type substrates. One of them recounts back to the birth of firsts photovoltaic devices. In 1950, with the development of space technology, it was necessary to create systems able to supply power the satellites launched into space. And it was mainly because the advantages of *p*-type substrates over those of *n*-type to outer-space conditions, regarding space-radiation resistance, that the photovoltaic technology was developed around *p*-type. These earliest solar cells

used substrates either 10 or 20 $\Omega\,\mathrm{m}$, combined with back surface reflectors (BSR), typically featuring two weldable contacts in front and back. The average production lot efficiency was $\sim 13\%$ at 1 AM0 [73–75].

On the other hand, in the past decade, a lot of scientific research has been carried out on *n*-type (mainly phosphorus-doped) substrates, confirming that compared to classic *p*-type (boron doped), *n*-type silicon cells feature two significant advantages. First, this kind of substrates does not suffer light-induced degradation (LID) caused by the simultaneous presence of boron and oxygen in wafers, a phenomenon that in standard *p*-type cells reduces the efficiency (two to three percent less), becoming evident within the first weeks after the installation of these modules. Second, *n*-type wafers are less sensitive to impurities commonly present in silicon feedstock; consequently, fewer efforts have to be made to obtain *n*-type wafers with a high electronic quality. Accordingly, *n*-type wafers, featuring high solar cell efficiency potential, can be made with a better cost-effectiveness than high-quality *p*-type wafers.

In terms of efficiency, well designed *p*-type solar cells, with a homogeneous emitter and aluminum back surface field (Al-BSF), reach efficiencies rounding $20\,\%$ with the current passivation and metallization concepts [76]. Going further, applying structural changes on the back side, like passivated emitter and rear cell (PERC), efficiencies of $20.3\,\%$ are plenty possible [77]. But examples of the current *n*-type efficiencies going beyond the $22\,\%$ are already mentioned in Table 1.1 clearly showing the advantage of *n*-type substrates.

1.3.2 The inner working of solar cells

There are several techniques to implement electron- and hole-selective contacts on silicon wafers. The most common one, it is by creating highly doped regions near the metal contacts. In Fig. 1.4 a) is sketched the structure of a simulated interdigitated back contact (IBC) *n*-type ($5\,\Omega\,\mathrm{cm}$) *c*-Si solar cell featuring two phosphorus diffusions (n^+). At the front, it is the so-called front surface field (FSF), and at rear-side the called back surface field (BSF). It is worth noting that the junction is at the back by the injection of Boron in the emitter region. The description of the inner working of this architecture is well explaining in the next section, including more details of specific important parameters. The main idea of this sketch is to illustrate the band diagram operation of a solar cell.

Figure 1.4 b) show the band diagram when the cell is in equilibrium. The band bending near both diffused regions indicates the strong dependence of the concentrations of electrons and holes to the position (gradient of their chemical potentials), and also indicates the presence of an electric field (gradient of the bands). These two forces (chemical gradients and electrical potentials) are identical in magnitude but opposite in direction. It means there is not a total force acting on the carriers (so, there is no net movement of the charges), and the Fermi level E_F remains constant through all the cut. In

Fig. 1.4 c), the band diagram when the cell is working in maximum power point, the Fermi energy splits into two quasi-Fermi energies, as a consequence of the excess concentration of carriers generated by the one-sun illumination. A small gradient of the quasi-Fermi energies drives electrons to the left and holes to the right. The reason for such directional flow of the two charge carriers can be seen in Fig. 1.4 d) showing that electron density is several orders of magnitude higher than hole density on the left (FSF, region n^+), and opposite the right (emitter, region p^+). It drives out of the device the holes through the emitter metal contact placed down as well as it happens for electrons through metal contact on the BSF (the band diagram it is not sketched).

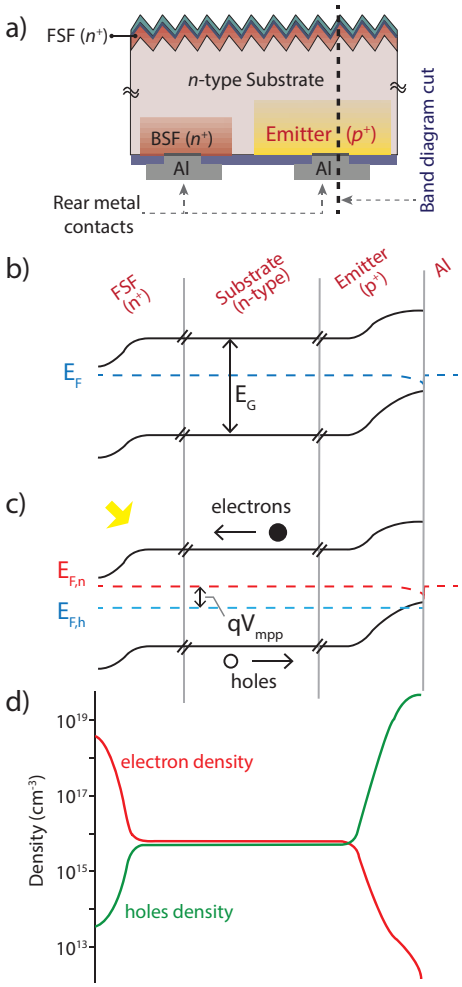

FIGURE 1.4: Energy band diagrams of an interdigitated back contact (p-type) c-Si solar cell. *a)* Sketch of the structure, including the main regions FSF, substrate, BSF, and emitter. On the right, is the band diagram cut line. *b)* Band diagram in equilibrium and *c*) Band diagram in the maximum power point operation. *d)* Concentrations of both electrons and holes, indicating the FSF, substrate and emitter regions, preferentially transport holes to the emitter metal contact.

1.3.3 Conventional solar cell

Solar cells with a conventional design are presently the dominant cell type in large-scale industrial manufacturing [78]. A conventional solar cell structure is based on a semiconductor *pn*-junction diode that operates under solar illumination as sketched in Fig. 1.5. The *n*-type layer on the top of the *p*-wafer is much thinner than the wafer; it typically has a thickness of around $0.3\,\mu\mathrm{m}$. Often, this layer is called the emitter layer. In the current commercial devices the whole wafer has a thicknesses between 100 and $300\,\mu\mathrm{m}$. In this devices, the contact formation with heavily doped silicon regions requires a high temperature firing process in a furnace at about $800\,^{\circ}\mathrm{C}$ [79].

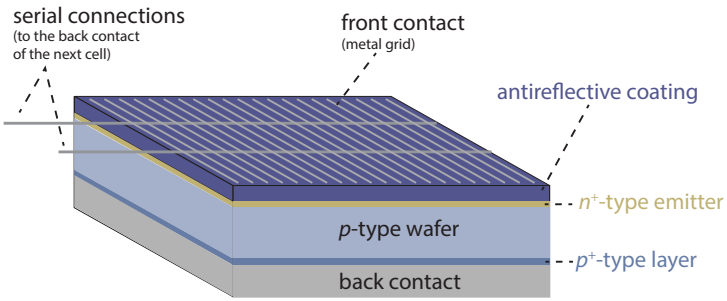

FIGURE 1.5: Sketch of a conventional *p*-type solar cell.

One of the main disadvantages of this type of solar cell architecture is the optical shadowing effect due to the presence of the front metal coverage. This lack strongly affects the ability of the device capturing photons, which reflects in a reduced J_{SC}. However, most of the fabricated silicon solar cells features this architecture with an average stabilized efficiency close to $17\,\%$ (156x$156\,\mathrm{mm}^2$) [78].

1.3.4 High-efficiency solar cells architectures

Different photovoltaic technologies have been classified as a generation: the first one consists of the crystalline silicon solar cells, exploiting one or another of the innovations previously described in this section. It is worth noticing that silicon can be single crystal or multi-crystalline. The second one has simpler and cheaper production techniques than those of monocrystalline wafer-based solar cells. However, the material quality of the second generation is lower because crystal lattice is not overall regular but only a short-range order within regions of the semiconductor called grains is ensured. The boundaries between grains are recombination centers. Therefore, to avoid excessive recombination rates, a minimum grain size in the millimeters range is required.

Since the introduction of second-generation devices, new semiconductor materials have been investigated, such as amorphous silicon, polycrystalline silicon, cadmium telluride and many others. Besides, thin-film, selective emitter, local point and others solar cell structures have been introduced. The third generation consists of technologies as nanocrystal and polymer materials' solar cells, which are promising but currently are not reliable.

As already discussed, different types of silicon wafers could be used to fabricate solar cell devices. To achieve the highest efficiencies, it is necessary that the bulk recombination must be as small as possible. Therefore, the high-efficiency concepts use monocrystalline wafers.

PERL solar cell

The first high-efficiency concept was developed in the late 1980s and the early 1990s at the University of New South Wales. Figure 1.6 illustrates the idea behind the PERL concept, which commonly uses a *p*-type float zone silicon wafer. With this architecture, conversion efficiencies of $25\,\%$ were achieved [5, 15]. The abbreviation PERL stands for Passivated Emitter Rear Locally-diffused. This abbreviation indicates two important concepts integrated into this technology: first, the optical losses of the PERL solar cell at the front side are minimized (but not avoided) using three techniques:

1. The top surface texturing is with inverted pyramid structures, allowing a fraction of the reflected light to be incident on the front surface for a second time, which enhances the total amount of light absorbed by the semiconductor.
2. The texturing is also covered with a double-layer anti-reflective coating (ARC), which results in a reduced top-surface reflection. Often a double-layer coating of magnesium fluoride (MgF_2) and zinc sulfide (ZnS) is used as an ARC.
3. To avoid the optical shading losses, the contacts at the front are small as possible. Hence the metal contacts are prepared using photolithography technology.

The second concept refers to the emitter design. The emitter region is highly-doped underneath the contacts, which in the PERL concept is achieved by heavily phosphorus-diffused areas. The rest of the emitter is lightly diffused to preserve an excellent blue response and avoid recombination losses. The emitter is passivated with a SiO_2 layer on top of the emitter to suppress surface recombination as much as possible. With the PERL architecture, the surface recombination velocity could be reduced so far that open circuit voltages with values of above $700\,\mathrm{mV}$ could be obtained, see Table 1.1.

At the rear surface of the solar cell, the devices feature point contacts in combination with thermal oxide passivation layers, which passivate the non-contacted area and hence reduce the undesirable surface recombination. A

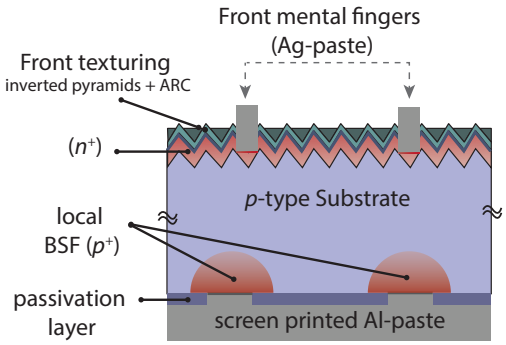

FIGURE 1.6: Sketch that shows the typical structure of a PERL cell.

highly doped boron region, created by local boron diffusion, operates as a local back-surface field to limit the recombination of the minority electrons at the metal back contact.

The interdigitated back contact solar cell

A second successful cell concept is the interdigitated back contact (IBC) solar cell. The main idea of the IBC concept is to have no shading losses at the front metal contact grid at all. All the contacts responsible for collecting charge carriers at the $n-$ and $p-$sides are at the back of the crystalline wafer solar cell. A sketch of such a solar cell is shown in Fig. 1.7 a).

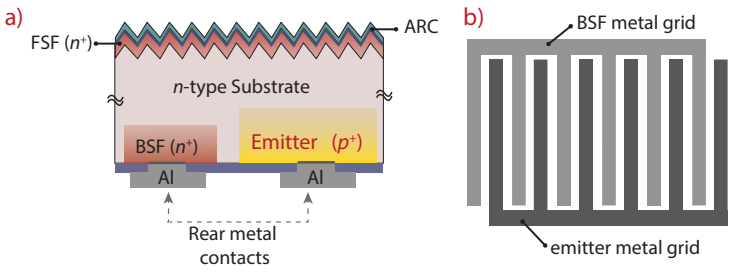

FIGURE 1.7: a) Sketch of the typical structure of an IBC cell. b) Sketch of the rear metallization of an IBC.

An advantage of the IBC architecture, it is that allows the use of monocrystalline float-zone (FZ) n-type wafers. This feature includes all the benefits discussed on Sec. 1.3.1. But, on the other hand, p-doped wafers have the advantage that the boron doping is more homogeneously distributed across the wafer as this is possible for n-type wafers. It means that within one n-type wafer the electronic properties can vary, which lowers the yield of solar cell products based on n-type monocrystalline wafers.

Although IBC cells are made from n-type wafers, they lack one large $p - n$ junction. Instead, IBC cells have many localized junctions. The holes are separated at a junction between the p^+ silicon and the n-type silicon, whereas

the electrons are collected using n^+-type silicon. The semiconductor-metal interfaces are kept as small as possible to reduce the undesired recombination at this defect-rich interface. Another advantage is that the cross-section of the metal fingers can be made much larger because they are at the back, avoiding shading losses. Thus, resistive losses at the metallic contacts can be reduced. Since both electric contacts are on the back side, it contains two metal grids, as illustrated in Fig. 1.7 b). The passivation layer should make from a low refractive index material such that it operates like a backside mirror. It will reflect the light above $900\,\mathrm{nm}$, which is not absorbed during the first pass back into the absorber layer. Thereby, this layer enhances the absorption path length.

At the front side of the IBC cell, losses of light-excited charge carriers due to surface recombination are suppressed by a front surface field similar to the back surface field discussed earlier. This field is created with a highly doped n+ region at the front of the surface. Thus, an n+-n junction is created that acts like an n-p junction. It will serve as a barrier that prevents the light-excited minority holes in the n-region from diffusing towards the front surface. The front surface field behaves like a passivation for the defects at the front interface and allows higher levels of the hole minority density in the n-doped bulk. Reflective losses on the front side are reduced in a similar way as for PERL solar cells: deposition of double-layered anti-reflection coatings and texturing of the front surface.

This solar cell architecture is analyzed deeply throughout this thesis and in the following chapters will be described in-depth each of the points mentioned here.

Heterojunction solar cell

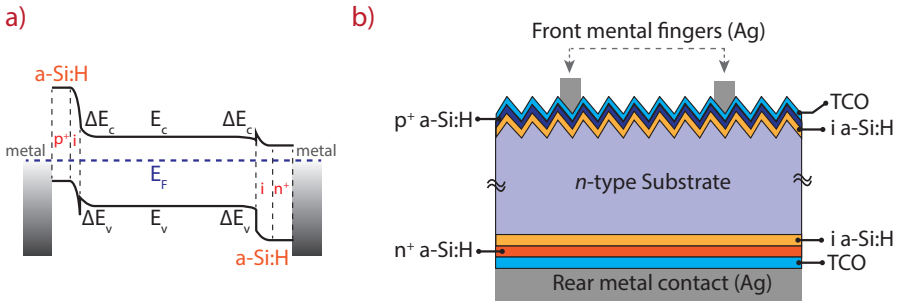

FIGURE 1.8: **a)** band diagram of a heterojunction in the dark and thermal equilibrium. **b)** Sketch that shows the typical structure of an heterojunction cell.

The third high-efficiency concept is the silicon heterojunction (SHJ) solar cell. Homojunctions, present in all the *c*-Si, are formed by the placement of different doping types inside the same semiconductor material. Hence, the bandgap in the *p*- and *n*-regions is the same. A junction consisting of a *p*-doped semiconductor material and an *n*-doped semiconductor made from

another material is called a heterojunction. In SHJ cells, the heterojunction is formed in-between two different silicon-related materials. For instance, it could be forming by an *n*-type FZ monocrystalline silicon wafer and other material such as hydrogenated amorphous silicon (*a-Si:H*), which is a silicon-based material in where the atoms are not ordered in a crystalline lattice but in a disordered one. The *a-Si:H* is a material with a bandgap of $1.7\,\mathrm{eV}$, which is considerably higher than that of *c*-Si ($1.12\,\mathrm{eV}$).

Figure 1.8 a) illustrates the band diagram of a heterojunction between *n*-doped crystalline silicon and *p*-doped amorphous silicon in the dark and thermal equilibrium. It is worth noting that next to the induced field, because of the space-charge region, some local energy steps are introduced. The two different bandgaps cause these steps for the *p* and *n* regions. The valence band is positioned higher, in the *p*-type amorphous silicon, than in the *n*-type crystalline silicon. This will allow the minority charge carriers in the *n*-type *c*-Si, the holes, to drift to the *p*-type silicon. However, the holes experience a small barrier. While they could not travel across such a barrier, according to classical mechanics, the quantum mechanics allows them tunneling across this small barrier.

The SHJ concept, initially developed by the Japanese company Sanyo and later acquired the Japanese Panasonic Corp., is currently commercialized under the HIT trademark (heterojunction with intrinsic thin-layer) [52, 80] since 2010, . Figure 1.8 b) shows the SHJ cell configuration with two junctions: the junction at the front side is formed using a thin-layer (typically $\sim 5\,\mathrm{nm}$) of intrinsic amorphous silicon, labeled as *"i a-Si:H"*. A thin-layer of *p*-doped amorphous silicon is deposited on top, labeled as *"p^+ a-Si:H"*. The heterojunction forces the holes to drift to the *p*-layer. At the back side, a similar junction is made. First, a thin layer of intrinsic amorphous silicon is deposited on the wafer surface *"i a-Si:H"*. On top of the intrinsic layer, an *n*-doped amorphous silicon is deposited, *"n^+ a-Si:H"*.

As discussed earlier, for high-quality wafers, like *n*-type FZ c-Si, the recombination of charge carriers at the surface determines the charge-carrier lifetimes. An advantage of the SHJ concept, it is the amorphous silicon layer acts as an excellent passivation layer. This feature allows reaching the highest possible charge carrier lifetimes. As a consequence, *c*-Si wafer-based heterojunction solar cells achieve the highest open circuit voltages of all the different c-Si technologies. The current record cell has an open-circuit voltage of $744\,\mathrm{mV}$and an efficiency of $26.3\,\%$. A comparison of all technologies is presented in Table 1.1.

The conductive properties of the *p*-doped amorphous silicon are comparatively weak. While in homojunction solar cells, the lateral diffusion to the contacts takes place in the emitter layer, in SHJ solar cells this occurs through a transparent conducting oxide material (TCO), such as indium-tin-oxide (ITO), deposited on top of the *p*-doped layer. The same contacting scheme is applying at the *n*-type backside. It means, this kind of solar cell uses a bifacial configuration: it can collect light from the front, and scattered and

diffused light falling on the back side of the solar cell. Another advantage of the SHJ technology comes from the fact that for the formation of amorphous silicon layers uses plasma-enhanced chemical-vapor-deposition (PECVD) technique, at low temperatures. Therefore, in SHJ solar cells, making both surface fields on front and back is a relatively cheap process.

1.4 Motivation and thesis outline

The PV industry has not relied on device modeling as much as the electronics industry. Indeed, it was common to make design improvements in solar cell devices only aided by intuition, general understanding of the device physics, trial-and-error adjustments or by empirical studies, without a quantitative analysis by computer device modeling. Nevertheless, since 2008, the improvement of energy conversion efficiency became an essential driver in the competition among solar cells manufacturers [81], which seek to offer the best devices. Since then, numerical device simulation started to grow-up and spread through the PV community, increasingly becoming a strategic and helpful partner who accelerates the optimization and reduces the costly and time-consuming of tests wafer runs. Especially now, the help, of simulations tools, is fundamental to explore modern complex concepts of solar cells, novel architectures, and application of new materials. In fact, the photovoltaic industry is experiencing tremendous growth and continues to push toward higher efficiencies and innovative cell designs.

Technology Computer-Aided Design (TCAD) refers to the use of computer simulations to develop and optimize semiconductor processing technologies and devices. Sentaurus is a TCAD software, by Synopsys, which solves the fundamental physical equations, such as diffusion and transport equations, to model the structural properties and electrical behavior of semiconductor devices. This in-depth physical approach gives TCAD simulation predictive accuracy for a broad range of technologies, including PV devices. Currently, all leading semiconductor companies use Synopsys TCAD tools throughout all its technology development cycle. At the early stage of technology development, TCAD tools allow to engineers the opportunity of exploring new design, prove alternatives such as engineering the substrate to enhance the position of metal contacts, test the quality of passivation-layers or varying the charges lifetimes. During the process-integration stage, TCAD tools enable engineers to execute simulations and split runs such as Design of Experiment (DOE), to evaluate, characterize, and optimize the process, saving time and money by reducing experimental runs on real devices. As the process is introduced into manufacturing, TCAD tools provide a mechanism for advanced process control during mass production, thereby improving parametric yield.

The IBC structure is currently one of the most promising technologies for low-cost high-efficiency silicon cells. To the point that the industry is very focused on their improvement although its fabrication process is more complicated and more expensive than the conventional counterparts. It is because, IBC solar cells have demonstrated the highest efficiencies for single-junction silicon cells, for one-sun applications (up to $25.2\,\%$) in investigation centers [11]. Figure 1.9 present a comparison of an IBC solar cell with a conventional one. SunPower corporation continues manufacturing IBC solar cells with continues improvements to reach commercial devices rounding the $24.2\,\%$ [82]. Recently, the combination of IBC designs with heterojunctions result in IBC HJ cells that have demonstrated the highest efficiency to date with $26.3\,\%$ [9]. And in short time, efficiencies greater than $26\,\%$ seem completely achievable. However, spite of the numerous advantages of IBC cells, there are some prerequisites to archive high-efficiency devices with this architecture. Some of this advances concern the quality of materials and others as a matter of the process fabrication. Furthermore, there is another aspect that is part of high-efficiency solar cells, which is the design. IBC solar cells are quite sensitive to geometrical parameters, doping concentrations and other parameters, which their perfect balance leads the optimal efficiency. In this regard, TCAD simulations perfectly match with the objective of bettering the designs. Several previous works, of computer device simulations, have been already presented, focusing mainly on the optimization of IBC cells or improvement of design parameters [83–86].

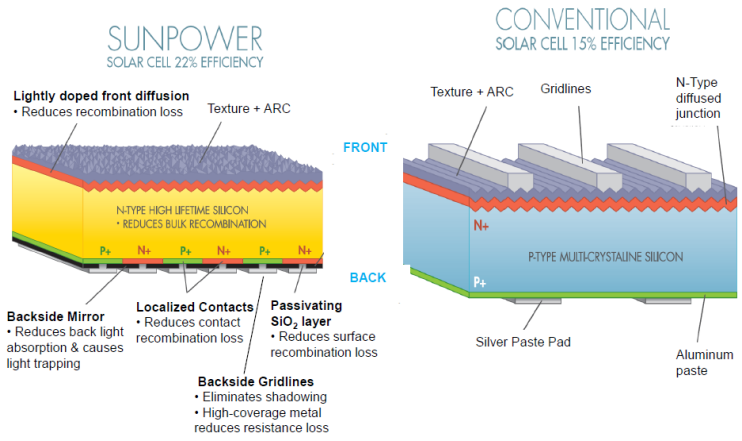

FIGURE 1.9: Illustration comparing the structures of a commercial IBC solar cell with a conventional one. On left, the sketch of an IBC structure. On the right, the diagram of a conventional solar cell. Image from [87]

One of the main issues, that IBC solar cells have to face, is the so-called electrical-shading effect [88], which adversely affects the behavior of the solar cell. The electrical-shading effect is a result of a reduced minority-charge carrier collection probability due to an increased recombination in the non-collecting base region, which consists of those areas without *pn* junction, i.e., generally, the BSF and the gap region. This unfavorable effect can be defeated by the addition of multiple contacts in the emitter region, which

reduces the device inner series resistance, and allows to increase the emitter sizes (rising with that, the *pn* junction). Nevertheless, the increment of metal/semiconductor interfaces' area also increments the recombinations, or on the contrary, small contacts size raise the resistive losses. Hence, it is essential to find a good trade-off between contacts' position, contacts number and determinate an adequate width of each metal-line. In literature, several works employ simulation tools to study the impact of metallization in solar cells, e.g., [89] compares the effects of the metallization on both PERL and PERC architectures, [90] analyzes the effect of resistive and recombination losses in a metal-wrap through (MWT) solar cell. But before this thesis, there are not works investigating the metallization on IBC solar cells by means TCAD tools.

This thesis aims to provide guidelines of the numerical simulation of IBC solar cells, using Sentaurus TCAD tools combined with the state-of-the-art of the physical modeling, to investigate the metallization schemes and optimization of design parameters. To achieve this goal, it was required performing a large number of calibrated simulations that sweep wide ranges of modeling parameters (i.e., changing geometric sizes, doping profiles, lifetime, and recombination rates) to investigate their influence over the device operation, and with that, allowing to identify the most critical ones. This work starts firstly, with the development of an adequate technique to evaluate the optical behavior, followed by the electrical analysis of IBC devices.

The remainder of this work is organized by chapters as follows:

Chapter 1 begins with a brief progress review of *c*-Si solar cells, in a way that put in context the main objective of this thesis, which is to provide guidelines of the numerical simulations of IBC solar cells. The chapter continues with a short but consistent introduction to concepts of the working of solar cells, based on an extensive bibliography. It introduces the physics behind its operation and reviews the principal figures of merit that characterize the solar cells. Besides, the thesis structure is detailed.

Chapter 2, titled as "Modeling Overview of *c*-Si solar cells", makes a detailed review of solar cell modeling in Sentaurus TCAD, as well as the state-of-the-art ob both parameters and models of *c*-Si. This Chapter presents the followed strategy and steps carried-out through all the thesis to accurate perform electro-optical simulations. It is described, in general, how to simulate several kinds PV architectures. The Chapter proceeds to describe the particularities of the IBC architecture, to continue with the introduction and definitions of the implemented simulation domains that evaluate the electro-optical functioning, leaving a full overview of the simulation process.

Chapter 3 describes in detail the numerical evaluation of the optical behavior of IBC solar cells by using Sentaurus TCAD and present some interesting results regarding ARC optimization. Simulation of PV devices under illumination requires an accurate modeling of light propagation and optical carrier generation within the absorbing semiconductor materials that later are coupled with the electrical simulation. This chapter details the method

used to determinate the optical generation profiles, $G(\zeta)$, by using a raytracer solver that accounts for the thin layers of the ARC. It discussed the traditional method to extract $G(\zeta)$ and presents a new methodology that is $\sim$ 10x faster than conventional. Later, it shows the optimization of ARC thickness. Finally, it reveals an analysis of the front surface texturing between flat, regular pyramids, and random pyramids.

Chapter 4 presents an analysis of the electrical modeling of IBC solar cells, concerning directly two topics:

- Optimization of the emitter coverage in IBC solar cells.
- Design guidelines for a metallization scheme with multiple emitter contact lines in IBC solar cells.

The description of each simulation setup, as well all details are carefully presented.

Chapter 2

Modeling overview of *c*-Si solar cells

As discussed previously, in Chapter 1, *c*-Si solar cells are simple *pn* junction diodes that cover the whole wafer area (see Fig. 1.2), but despite the *"simplicity"* of its structure, their performance cannot be fully described by using only analytical theories. In fact, it is impossible analytically consider all the non-idealities, neither include all the design variables of the real device structures (e.g., surface imperfections, contacts position, metallization schemes [91], and others). Even when the devices are simplified as one-dimensional (1D) structures, an analytical approach quickly becomes a challenge difficult to address, especially if parameters such as variable doping profiles, surface electrostatics fields, bulk trap-states, or the dependence of mobility and carrier lifetime on doping concentrations enter into consideration to solve the problem. On the other hand, properly implemented, the forecast precision of numeric simulations is limited only by the calibration fidelity of the input equations and parameters. Indeed, numerical approximations allowing evaluate with high accuracy the optical behavior of complex geometries [92, 93], analyze novel metallization schemes [94], or appraise the electrical performance of advanced architectures. This chapter makes a detailed review of solar cell modeling in Sentaurus TCAD as well as the state-of-the-art either *c*-Si parameters and models.

2.1 The simulation software

Whereas some of the most widely used one-dimensional solar cell simulators are available for free as research tools for the PV community, many of the today most robust and reliable three-dimensional (3D) device-physics simulators have been developed and commercialized for the semiconductor microelectronics industry by electronic design automation (EDA) software firms. Many of TCAD software include by default a broad variety of numerical and mathematics methods to solve the semiconductors physics, which the engineering designer can quickly select or modify respectively. Many of the now available TCAD software, for industry or research centers, allows simulating all the cycle of the device from the first drafts of the design to the

final manufacturing process of any semiconductor device at a micro- or even nano-dimensional scale. Sentaurus TCAD was the software selected for this thesis, which is a family of tools that include Sentaurus "Device," a state-of-the-art device physics simulator [95]. Sentaurus TCAD after many years, it is now within the EDA industry as a referent in semiconductors' simulation software. The genealogy of this software family can be traced back to several other commercial simulation tools, prominently featured, in prior solar cell modeling, including ISE DESSIS [96–98] and SIMUL [99–101].

2.2 Strategy of the modeling approach

The modeling strategy followed throughout this work is presented in the flowchart of Fig. 2.1, that describes how to simulate several kinds of solar cell architectures. Among the more remarkable are the conventional *p*-type cells, PERC (Passivated Emitter and Rear Cell), PERL (Passivated Emitter, Rear Locally-doped), or PERT (Passivated Emitter, Rear Totally-diffused) [5, 102]. By using this strategy, it is also possible modeling silicon heterojunction (SHJ) solar cells [52, 103]. It is a particular interest in this thesis to focus mainly on IBC (interdigitated back contact) structure.

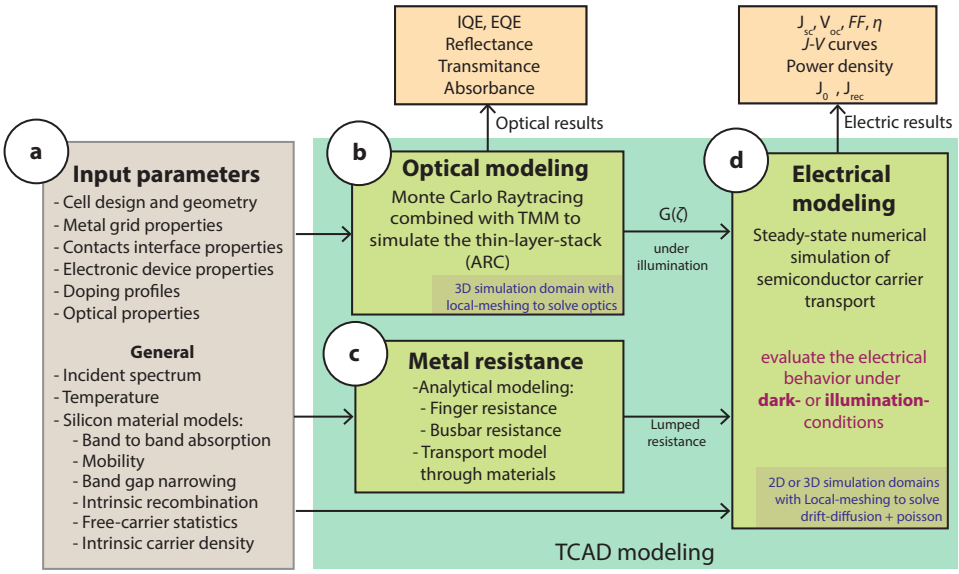

FIGURE 2.1: Flowchart describing the modeling approach implemented in Sentaurus TCAD for this thesis [104].

The first step to simulating any device starts by collecting and adjusting the physical parameters and models, that define the materials and structure, in such format that simulator recognizes, a) in Fig. 2.1. Every year Synopsys upgrade the software, including the state-of-the-art physics and allowing to the designer a quick access to them. However, other specific parameters must be

locally calibrated or adjusted using either literature or real device measurements. It is important to clarify that solar cells simulations could be evaluated either dark or under illumination conditions. In dark conditions, the cell behavior is assessed electrically applying a forward bias voltage. On the other hand, to evaluate the illuminated solar cell, the optical response is first characterized and then linked with the electrical modeling through an optical generation profile.

The optical modeling, block b) in Fig. 2.1, takes the solar radiation incident on the cell and the optical parameters (refractive index and extinction coefficient) of all the materials to calculate the absorption of the light in the device, as well as the reflection and transmission through the anti-reflective coatings and the surface texturing. With that results is calculated a 1D generation profile of electron–hole pairs within the semiconductor, ($G(\zeta)$), which simplify the complex geometry of the texturing to an equivalent flat surface. This step greatly simplifies the following electrical modeling to treat the solar cell as having a planar surface. Details for the calculation of $G(\zeta)$ are presenting in the corresponding optical section.

To maintain the complexity of the modeling at an adequately high-level, but not extraordinarily complex, contour losses are compacted in an analytical calculated lumped resistance in the block c) in Fig. 2.1. Among the parameters, not explicit included in the simulator, but considered in this lumped resistance are for instance the distributed nature of the metal fingers (in the case of 2D simulation approach) or the perimeter losses in busbars [105].

Concerning the electrical modeling, the main inputs for solar devices are the doping profile $N(\zeta)$, the surface Shockley–Read–Hall (SRH) recombination parameters S_n and S_p and at times empirical correction factors in the case. It is worth mentioning that the textured surface is approximated by a planar electrical solution domain, which for the detailed modeling requires the introduction of correction factors to reproduce experimentally measured characteristics.

2.3 Physical models and material parameters

As was introduced in Sec. 1.2, once photons with an energy greater or equal than the bandgap of the cell are absorbed, generate electron-hole pairs within the absorber layer. The pn junction creates the built-in field that drives out the photogenerated carriers, thereby producing current in an external circuit. The effectiveness of this process depends on the balancing between carrier generation, recombination, and transport.The carrier generation rate directly depends on the wavelength, intensity of incident light and semiconductor type. Under lighting conditions or generally when the carrier concentration exceeds the thermodynamic equilibrium, the system wants to be at its lowest

potential (the most stable condition). Therefore, to reach equilibrium, recombination of charge carriers comes into play, and the recombination rate is described by:

$$\left(\frac{d\Delta n}{dt}\right)_{rec} = -\frac{\Delta n}{\tau_{eff}} \tag{2.1}$$

where τ_{eff} is the carrier lifetime which characterizes the level of recombination in the system. Since solar cells are devices of transport, the ultimate collection efficiency depends on either carrier lifetimes and diffusions concentrations. Whereby the carrier lifetimes mechanisms in solar cells should carefully implemented in the simulator. Several recombination mechanisms determine the minority carrier lifetime such as radiative, Auger, and Shockley–Read–Hall (SRH) that where introduced in Chapter 1. The studies of the properties of silicon have been on the scene for a long time, and all these recombination models are well detailed in the state-of-the-art literature. To accurately simulate silicon cells all the recombination mechanisms are considered, so the overall effective-lifetime τ_{eff} is then calculated from:

$$\frac{1}{\tau_{eff}} = \frac{1}{\tau_{intr}} + \frac{1}{\tau_{bulk,SRH}} + \frac{1}{\tau_{surf}} \tag{2.2}$$

where τ_{int} is the intrinsic lifetime extracted from [23], and the other two $\tau_{bulk,SRH}$ and τ_{surf} are the SRH in bulk and surface lifetimes respectively. As mentioned earlier, carrier transport is crucial in determining the extraction or the collection efficiency. Therefore, in addition to carrier lifetime, carrier mobility and diffusion lengths are important.

2.3.1 *c*-Si modeling and parameters

The input parameters common to all the performed simulations, including the choice of parameterization for modeling silicon properties, are summarized in Table 2.1. It is worth mentioning that, to be consistent with the implemented model for the Auger and radiative recombination of Ritcher et al. [23], the temperature for all the simulations is set up to $300\,\mathrm{K}$.

As mentioned above, most models are implemented by default in the simulator, but this is not the case for Auger and radiative recombination. The model was introduced in the simulator using a physical model interface (PMI) which allows adding models to express physical properties. To validate the implemented model, Figure 2.2 shows the intrinsic lifetime in a *p*-type substrate τ_{intr} picked-up from the paper and the modeled results from TCAD, with the same characteristics as are defined in it. It can be seen that for a Δn ranging from 10^{10} to $10^{20}\,\mathrm{cm}^{-3}$ and for a N_{dop} (net dopant concentration) ranging from 10^{15} to $10^{19}\,\mathrm{cm}^{-3}$ both are in very good agreement.

Regarding the implementation of the surface SRH recombination velocity (SRV) model, in the phosphorus-doped regions (FSF, BSF, and substrate), is

Input	Description	Reference
Free-carrier statistics	Fermi-Dirac	[104]
Bandgap narrowing	Model proposed by Schenk	[106]
Free-carrier mobility	Klaassen's unified mobility model	[107]
Recombination velocity at Metal/Silicon interface	$S_n = S_p = 1 \times 10^7\ \mathrm{cm\,s^{-1}}$	[104]
Intrinsic carrier density	$n_i = 9.7 \times 10^9\ \mathrm{cm^{-3}}$ at 300 K	[55, 56]
Intrinsic recombination: radiative and Auger	Semi-empirical model by Richter et al.	[23]
SRH lifetime	Scharfetter relation (by default in Sentaurus TCAD) ($\tau_n = \tau_p$)	[108]
Surface recombination velocity (SRV)	Semi-empirical models for phosphorous- and boron-doped regions by Altermatt et al.	[109, 110]
Specific contact resistance	BSF (n^+): $\rho_{c,BSF} = 2.2\,\mathrm{m\Omega\,cm^2}$, Emitter ($p^+$): $\rho_{c,em} = 3.9\,\mathrm{m\Omega\,cm^2}$	[111]
Aluminum resistivity	$\rho_{al} = 2.65\,\mu\Omega\,\mathrm{cm}$	[112]
Incident spectrum	AM1.5G	[113]

TABLE 2.1: General input parameters and models used in the thesis. The temperature for all the simulations is set to 300 K.

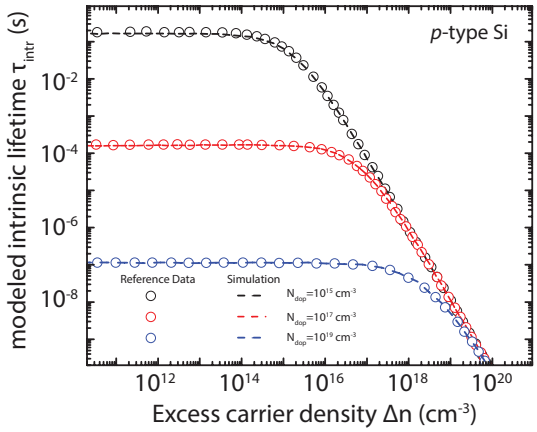

FIGURE 2.2: Validation of the implemented intrinsic lifetime τ_{eff} in Sentaurus TCAD with the data presented in [23].

based on work of Altermatt et al. in [109]. They derived a semi-empirical model for surface recombination velocity dependent of doping concentration (N_{dop}), considering Fermi–Dirac's statistics, outlined in the following equation:

$$S_{po} = S_{p1}\left(\frac{N_{dop}}{N_{p1}}\right)^{\gamma_{p1}} + S_{p2}\left(\frac{N_{dop}}{N_{p2}}\right)^{\gamma_{p2}} \tag{2.3}$$

This model is numerically evaluated in the pre-processing, reading the doping parameter at the interface N_{dop} and assigning a value of surface recombination. Figure 2.3 shows the approximation for the data reported by Glunz et al. [114], that displaying the differences in surface recombination velocities between flat and textured surfaces in function of the doping concentration. Regarding the emitter region (boron-doped) the values of SRV are reported in [110].

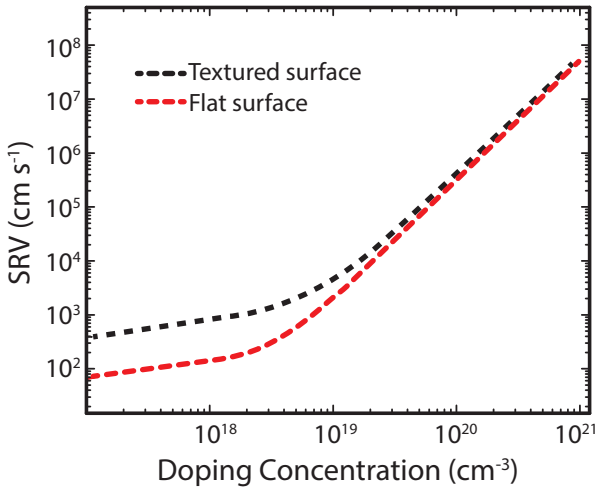

FIGURE 2.3: Surface recombination velocity of a planar and textured surface in function of the doping concentrations in n^+-doped regions, approximating the measurements reported in [114].

2.3.2 The architecture: Interdigitated Back-Contact (IBC)

As mentioned above, the aim of this thesis is mainly focusing on the analysis of the interdigitated back-contact (IBC) solar cells design because of its great potential for achieving high efficiencies. One of the most outstanding advantages of this architecture which improves their performance lies behind the fact that it has no optical shading, caused by front metal grids (Fig. 2.4), commonly observed in conventional solar cells. The absence of optical-shading in IBC cells reflects in its enhanced short-circuit currents. Since the collection of charges occurs at the rear side of the device, the designers have a certain necessary degree of freedom in the front-side to extend and improve their optical or electronic designs. Due to significant improvements on the front, the Kaneka designers achieved $42.3\,\mathrm{mA\,cm^{-2}}$ of short circuit current in the current IBC cell with the best efficiency (see Table 1.1).

Front surface passivation with, e.g., silicon oxide combine with silicon nitride as an anti-reflection layer (ARC), can be complemented by a lightly diffused n-type layer, which suppresses the concentration of holes near the pyramidal texturing in the surface. Other possibilities for maximizing light-coupling into the wafer include the use of black silicon as a broadband anti-reflection coating [115–118] and multi-scale surface texture [119]. Nevertheless, it is essential that such optical schemes be compatible with high-quality surface passivation. In Fig. 2.5 are the plots of recombination currents either dark and illumination, as functions of FSF-doping with and without featuring front texturing, which the surface recombination velocities are in Fig. 2.3. A comparison of the curves reveals the importance of correct FSF doping since it

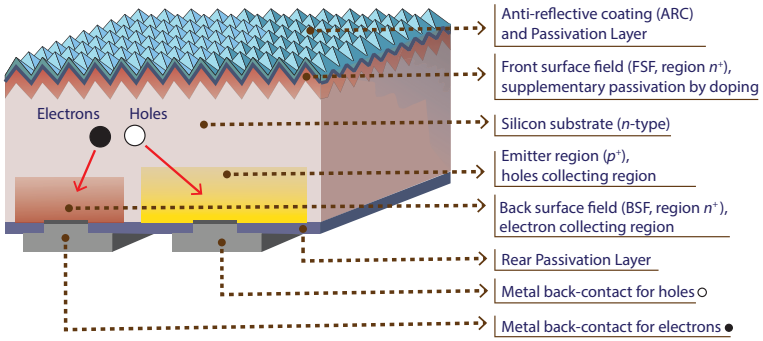

FIGURE 2.4: Schematic of the components of an interdigitated-back-contact cell. Both electrons and holes are extracted through the rear locally diffused phosphorus- and boron- regions (BSF and Emitter), metallized with stripe lines through local openings in the back dielectric passivation layer.

reduces the surface recombination velocity in front, although the recombination rate in the textured cell is greater than the flat one.

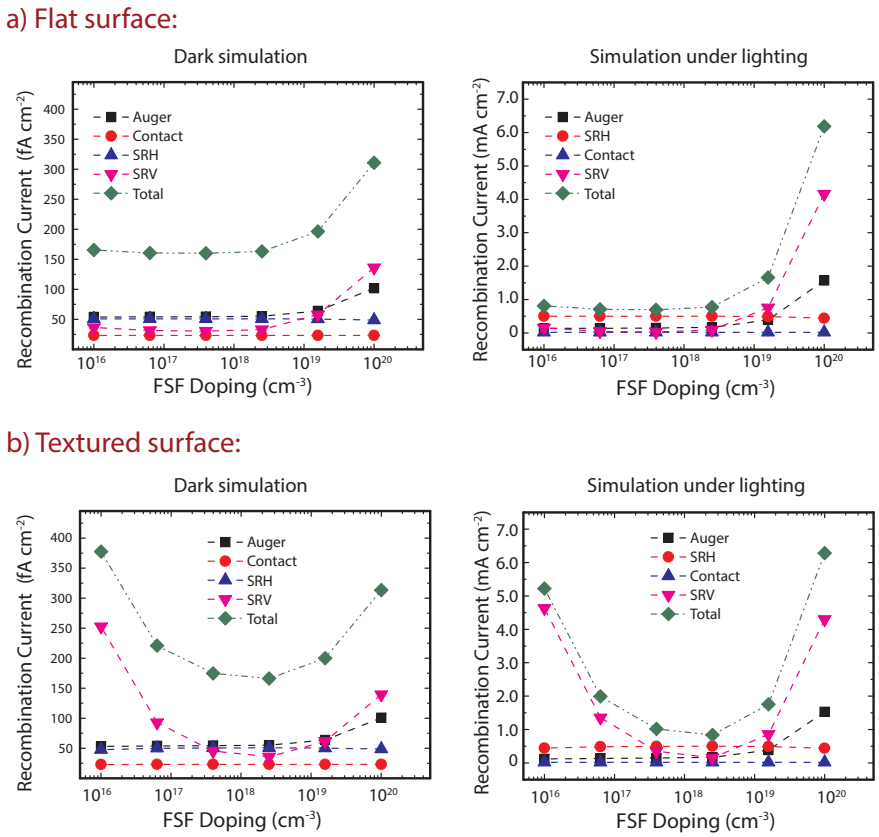

FIGURE 2.5: Recombination current losses analysis, for a cell featuring and not surface roughness, in function of the doping peak in FSF. The SRV for these simulations are in Fig. 2.3. The FSF-doping is a Gaussian-spatial function with the maximum at the edge of the device, with a junction depth $1\,\mu\mathrm{m}$.

In a likely production chain, the diffusions formation either boron and phosphorus are alternated at the rear part to create regions that collect electrons

and holes selectively. Hence the cell structure consists of alternating, or interdigitated, stripes of n- and p-type doped regions as in Fig. 2.6. The optimization of the doped-strip widths is essential for an efficient carrier collection, which depends on the carrier diffusion length, the recombination properties of both phosphorus- and boron-doped regions, as well as its peak concentrations. Since electron mobility is approximately three times higher than hole mobility in moderately doped silicon, the p^+ region covers a larger fraction of the rear pitch and thereby increase the area of collection (pn junction). It is worth mentioning that a wider emitter (p^+ region) reduces the build-up of hole concentration at the front surface, which would intensify recombination there. Electrons flow mostly laterally towards the n^+ rear stripes, not only through the n-type wafer but also through the front n^+ diffusion, when it is present.

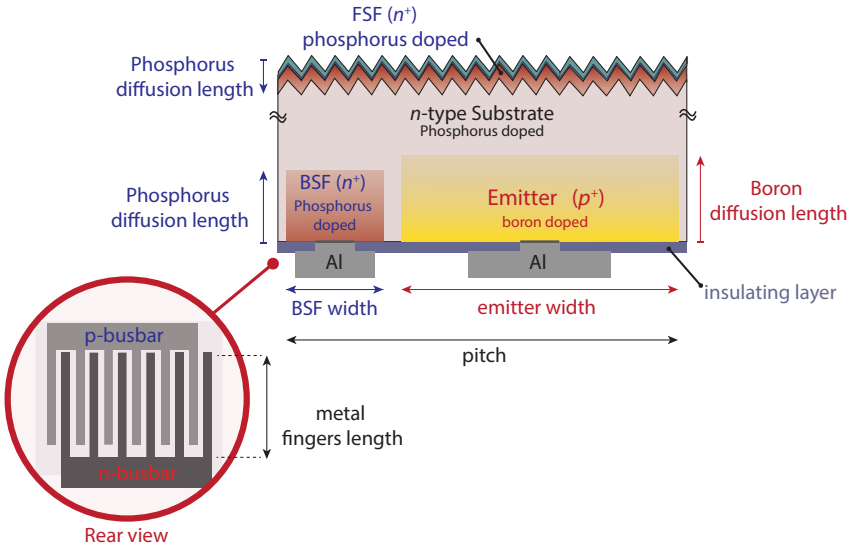

FIGURE 2.6: IBC solar cell structure with geometric parameters.

Nevertheless, each IBC cell structure needs to a specific optimization for a given set of recombination and transport properties (more details discussed in the following chapters). A thin insulating layer is used to passivate the back surface of the wafer [120]. Metal stripes make electrical contact through local openings etched into the passivation layer. The metal contact lines are slightly narrower than the doped regions and are finely aligned and placed below each of these sections, trying to avoid overlaps with the neighboring stripes. The openings must be sizable enough to extract current with minimum contact resistance losses and small sufficiently to minimize recombination losses caused by the direct contact between the metal and silicon. One of the difficulties of fabricating high-efficiency IBC solar cell is to reduce the high electrode resistivity losses. Several proposed works suggest optimizing the number of busbars, number of contact points per busbar, busbar-width, metal resistivity, and metal thickness [105, 121].

A high fill factor of $83.8\,\%$ was achieved by the best Kaneka's IBC solar cell, despite its large area, with this local contact design. As described above, a

significant advantage of placing both metal contacts at the back lean on the fact that optimization of geometry does not include any trade-off with optical shading. In fact, metal stripes can almost entirely cover the rear surface, and thus simultaneously act as a back reflector. The thin dielectric layer between the silicon and the metal lines helps to minimize parasitic plasmonic absorption of infrared light in the metal layer [122]. An alternative to reducing the contact area between the doped silicon and the metal-stripes is by incorporating passivate contacts based on doped poly-silicon layers [123], which can relax those requirements. With an open-circuit voltage of $744\,\mathrm{mV}$ the best IBC cell of Kaneka, demonstrates a remarkable bulk-lifetime, and an excellent surface- and contact passivation. However, regarding open circuit voltage, silicon heterojunction technology can provide even better performance because the metal contacts, which are highly recombination active in traditional, diffused-junction cells, are electronically separated from the absorber by insertion of a wider bandgap layer [52–54].

2.4 Simulation domains

Compared with many other kinds of semiconductor devices, solar cells are larger; in fact, its area covers several square centimeters. Despite, it is not necessary to simulate the full device area because taking advantage of high-symmetry of semiconductors it is possible to consider for simulations only a small and periodic standard domain that contains most of the physics, representing the whole device. In this way, the calculation resources are better used, and the results are obtaining out faster, without compromise accuracy.

A broad diffuse practice, in the PV community, consists of evaluating the optical and electric simulations independently, which is practical in several ways. For instance, the meshing resolution size required to solve the optic response necessities to be much finer than the needed to resolving the electrical behavior, in most regions of the device. Even the considerations of sizing and shape are different for each one. Regarding the optical analysis, it is important considering the effects of surface texturing over the charge collection. However, it is enough to take a look only in a portion that characterized the full surface roughness instead of unnecessary modeling the whole device area. In the case of a cell with an isometric texturing, it is sufficient to model just the optic of one pyramid to extrapolate the result to the others, as a) in Fig. 2.7.

On the other hand, the electric-simulation domain is usually bigger than the optical one, and it requires another meshing strategy. The meshing procedure, in the electrical simulation domain, starts by creating a coarse grid in the whole structure followed by the addition of finer meshing refinements in specific regions. Although meshing refinement strategies varying in dependence of the device structures and simulation purposes, the guidelines are always the same; it is important to reduce the mesh-grid size near to the

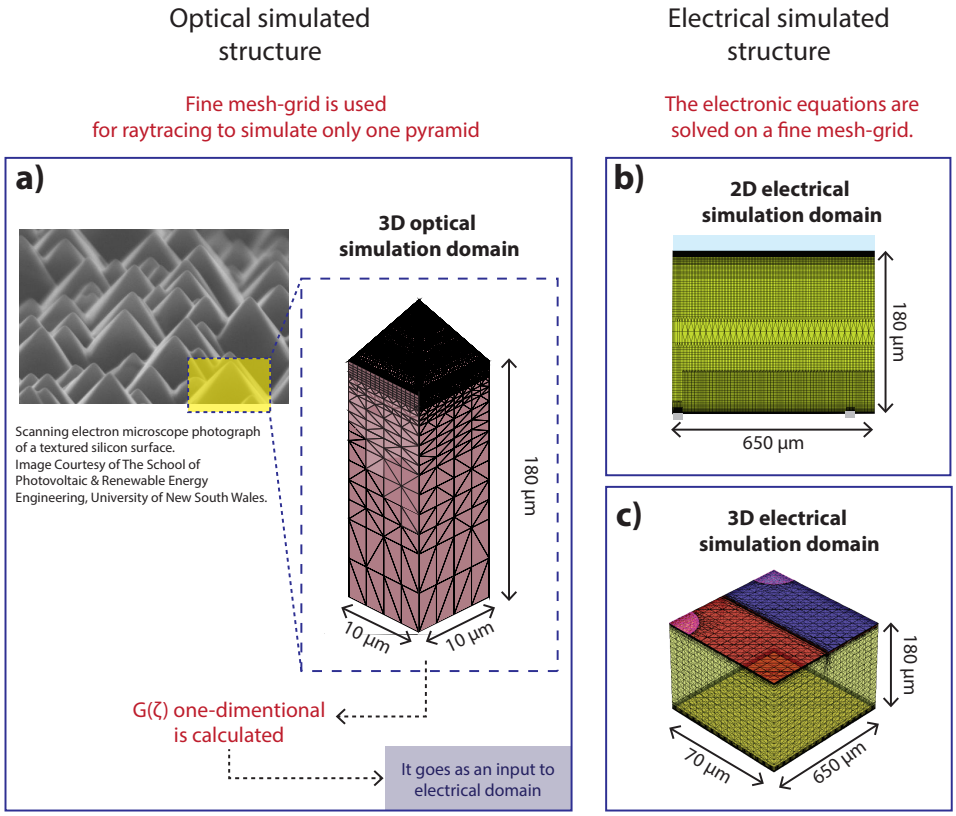

FIGURE 2.7: Simulation domains. **a)** 3D Optical simulation domain computes $G(\zeta)$. **b)** 2D electrical simulation domain. **c)** 3D electrical simulation domain. The link between optical and electrical domains is $G(\zeta)$

junctions and metal contacts, as well as, in the uppermost part of the device, where most of the generation occurs.

For many solar cell structures, it is enough to approach the electric device in two-dimensional (2D), saving a lot of computational effort and time, Fig. 2.7 b). Nevertheless, in the case of point-contact metallization, the standard domain must be 3D because cannot be approximated with by a 2D approach, for two important reasons: (i) the power resistive losses in solar cell are proportional to ρj^2, where ρ is the contact resistivity and j is the local current density, which differs significantly between finger [124, 125] and point-like geometries [91]; (ii) the recombination losses depend sensitively on the minority carrier density, given by the quasi-Fermi level $E_{F,min}$, and is connected to j by $j \propto \nabla E_{F,min}$, Fig. 2.7 c). Hence, approximating a point-contact structure with a 2D finger geometry causes errors in both resistive and recombination losses [126].

Therefore, for all that was mentioned above, there is a need to link the obtained optical results (in a small 3D domain) to the electrical wider simulation domain 2D or 3D. The solution is to calculate a 1D optical generation profile ($G(\zeta)$), which is a spatial function that contains the number of the

carrier generated through all the layer stacks and goes as input to the electrical simulation. Even though the mesh-grid for both domains is different, the electric-simulation domain receives the 1D optical generation profile and gives value to each 2D- or 3D-mesh-grid (spatially non-uniform) by vertex-based linear interpolation.

2.5 Optical modeling

The first step to evaluate a solar cell under illumination conditions is to model the light propagation and calculate the carrier generation rate (of electron-hole pairs) within the device through all the absorbing layers. The photogeneration rate is not uniform in the semiconductor, in fact, strongly depends on the position. As it will see below, most of the photogeneration occur on the first microns from the up surface. The optical simulation computes the photogeneration as a function of position, $G(\zeta)$ where ζ is the equivalent distance of the textured surface to a flat surface. The purpose of using ζ rather than depth is that it converts the generation profile under a complicated geometry (e.g., random pyramids) to an equivalent generation profile of a planar surface, [127]. The optical generation profiles are calculated taking as input the simulated AM1.5G solar spectrum with data chosen per international standard IEC 60904-3-Ed2 [113] and an integrated irradiance of $1000\,\mathrm{W\,m^{-2}}$ in the wavelength range 0 to infinity. Once calculated $G(\zeta)$, it goes as an input to electrical modeling, which uses this information to give each mesh-point a generation rate value. This information, coupled with electrical modeling predicts the behavior of the device and will be explained in the Sec. 2.7.

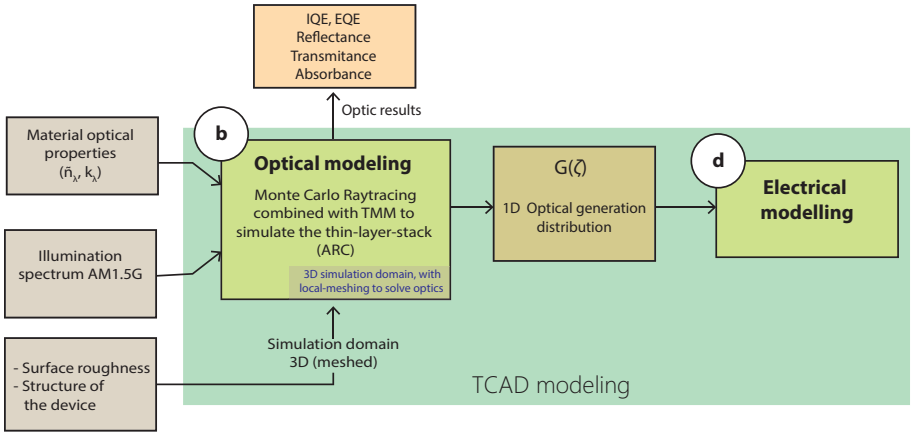

FIGURE 2.8: Optical modeling flowchart implemented in TCAD. The link between the optical **(b)** and electrical modeling **(d)** is the 1D photogeneration rate $G(\zeta)$.

Texturing the surface of solar cells is an effective way to increase efficiency by enhancing the light absorption capability [128–131]. Nevertheless, from the simulation point of view, the modeling complexity increases with it and still more with the broad variety of types of textures and shapes formed in

real devices, such that presented in Fig. 2.9. Many of these texturing, due to its irregularity, are only properly analyzed in 3D [132].

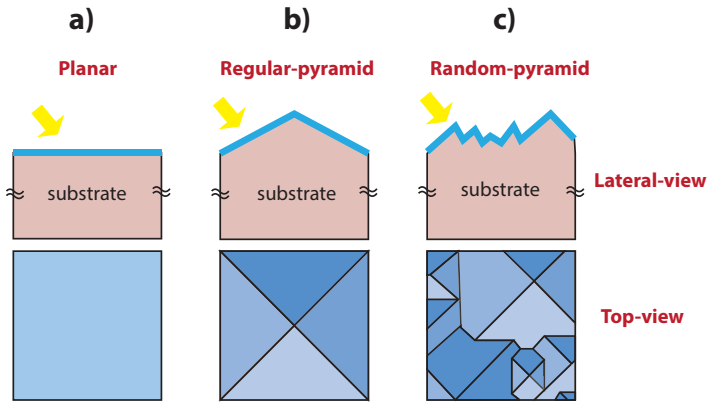

FIGURE 2.9: Surface texturing in *c*-Si solar cells. **a)** Surface without texturing, **b)** regular pyramid-texturing, and **c)** random-pyramid texturing.

To solve the optical modeling, it was implemented a 3D ray tracing technique combined with a Monte Carlo approach, allowing to determine the optic inner-interactions of solar cells featuring different patterns of surface texturing. The advantage of using Monte Carlo ray tracing instead of the regular ray tracing method, it is that the first one only analyzes one propagating beam rather than all split rays for the calculations. So, by far, Monte Carlo ray tracer is much faster, but to be statistically consistent it requires an enough higher ray density. For the structures analyzed in this thesis, a distribution of $400\,\mathrm{rays}/\mu\mathrm{m}^2$ over the surface produces comparable results with literature and measurements.

It is important mentioning that Ray tracing is an indirect method that determines the total absorption inside the device by obtaining the total reflectance and transmittance without considering the interfaces [133]. For this reason, the anti-reflective coating (ARC) in front- and back surfaces are handled in a particular way (as boundary conditions) to account their effects into the simulations, see Fig. 2.10. The angle at which the rays are incident on the ARC pass as inputs to the TMM (Transfer Matrix Method) solver, which returns the reflectance, transmittance, and absorbance for both parallel and perpendicular polarizations to the ray tracer. The ray tracer calculates each angle of refraction according to Snell's law, details in-depth are cover in [95].

2.5.1 Definition of optical output parameters of a solar cell

The following optical output parameters can help to understand in more detail how the solar cells behave. Starting with the reflectance $R(\lambda)$:

$$R(\lambda) = \frac{P_R(\lambda)}{P_{in}(\lambda)} \tag{2.4}$$

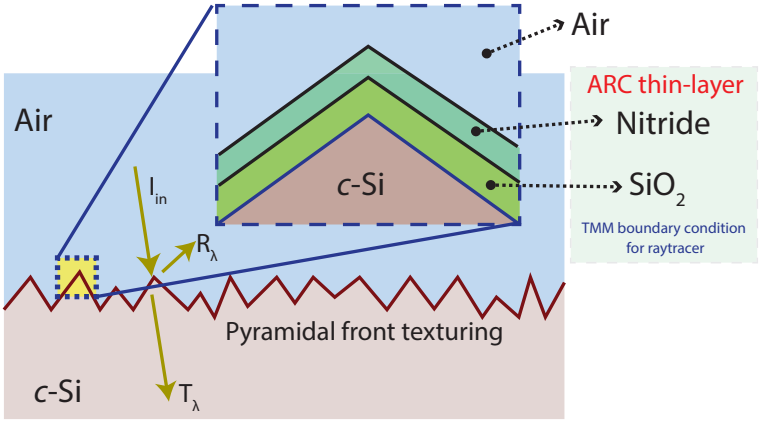

FIGURE 2.10: Illustration of thin-layer-stack boundary condition for simulation of an ARC layer.

where P_R is the reflectance portion of the incident solar power.

the transmittance $T(\lambda)$, given by:

$$T(\lambda) = \frac{P_T(\lambda)}{P_{in}(\lambda)} \tag{2.5}$$

where P_T is the transmitted portion of the incident solar power.

the absorbance $A(\lambda)$, given by:

$$A(\lambda) = \frac{P_A(\lambda)}{P_{in}(\lambda)} \tag{2.6}$$

where P_A is the absorbed portion of the incident solar power.

$R(\lambda) + T(\lambda) + A(\lambda) = 1$

the spectral response $SR(\lambda)$, typically expressed in $\mathrm{A\,W^{-1}}$, is defined as the ratio of the current generated by the solar cell under short-circuit current conditions $J_{SC}(\lambda)$ to the incident irradiance $I_{in}(\lambda)$, as a function of the wavelength λ of the radiation:

$$SR(\lambda) = \frac{J_{SC}(\lambda)}{I_{in}(\lambda)} \tag{2.7}$$

The external quantum efficiency $EQE(\lambda)$, representing the probability that carriers are generated and collected at the cell terminals under illumination, which is defined as the ratio of the number of carriers collected by the solar cell under short-circuit conditions to the number of incident photons of a given energy:

$$EQE(\lambda) = \frac{\eta_{sc}(\lambda)}{\eta_{in}(\lambda)} = \frac{J_{SC}(\lambda)}{J_{in}(\lambda)} \tag{2.8}$$

where $\eta_{SC}(\lambda)$ is the rate of carriers collected by the solar cell under short-circuit conditions, $\eta_{in}(\lambda)$ is the incident photon rate (i.e., the number of incident photons per unit time), $J_{SC}(\lambda)$ is the short-circuit current density, and

$J_{in}(\lambda)$ is the incident photon current density, respectively, as a function of the wavelength λ of the radiation.

The incident photon flux $\Phi(\lambda)$ (i.e., the number of photons per time and area unit) is given by:

$$\Phi(\lambda) = \frac{I_{in}(\lambda)}{E_{ph}(\lambda)} = \frac{I_{in}(\lambda)}{h\nu} \tag{2.9}$$

where $E_{ph}(\lambda)$ is the photon energy as a function of the wavelength λ of the radiation. The collection rate of carriers under short-circuit conditions is given by $J_{SC} \cdot A/q$, while the incident photon rate is $\Phi(\lambda) \cdot A$, where A is the area of the solar cell.

2.6 Metal resistance modeling

With the aim of keeping complexity at a moderate level, this approach overlooks some full-size effects, e.g., perimeter losses, busbar recombination, the distributed nature of the metal grid resistance, and inhomogeneities wafer or metal-silicon interface. Figure 2.11 b) sketches the full metallization of an IBC cell, including the representations of busbars and the perimeter diodes (formed in the region between fingers-end and the busbars). Altermatt et al. [134] numerically quantified the edge losses and show design guidelines to reduce it, meanwhile in [105], by exploiting TCAD simulations, analyzed the influence of busbars in large-area cells with this architecture. Both works showed the importance of these parameters in IBC solar cells simulations, and the importance to incorporate a parameter that accounts for these losses, especially if are not directly considered in the simulations modeling.

The block c) in the flowchart of Fig. 2.1 calculates the equivalent lumped resistance (R_s) of the metal grid. This model neglects distributed nature of the metal through all silicon, but it is a good approximation that saves a lot of solving time, allowing reducing the simulation domain to a 2D approach instead of a complex 3D modeling. The value of R_s is analytically calculated as describes [135], taking into account the metal resistivity, the number of fingers and the contact resistance. All along this thesis, the busbar resistance is neglected, which is consistent with a high number of measurements throughout the busbar, during *J-V* testing [104]. It is worth mentioning that for all the simulations, it is considered the metal fingers shape as rectangular, as is sketched in Fig. 2.11 a).

The electrical contacts at the rear which form the boundary conditions can be either ohmic or Schottky type, whereas parallel and series resistances are extern to the TCAD simulations [95].

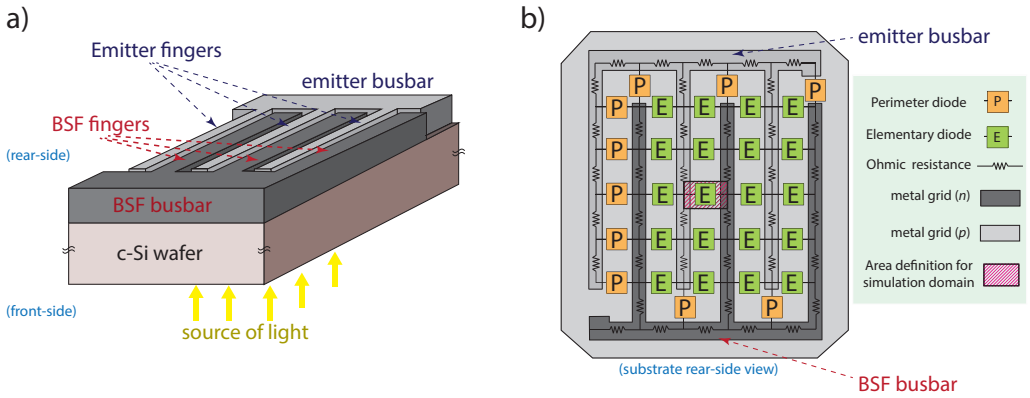

FIGURE 2.11: Sketch of rear-view showing the metal grid of an IBC solar cell.

2.7 Electrical modeling

Sentaurus Device employs a numerical discretization with the Finite-Element Method (FEM) to solve the constitutive equations of device physics over a finite-element mesh that could represent any semiconductor device [95, 99]. The mesh-grid stores the values of all physical quantities throughout the geometry device, including impurity concentrations (N_D, N_A), carrier concentrations (n, p), and electrostatic potential (Ψ); and also specifies which boundaries of the device are electrodes. Once calculating the state of the mesh that satisfies the device physics equations, Sentaurus records the current and voltage of each electrode. By repeating this procedure, sweeping certain range of electrode biases, the *J-V* behavior of the device is reproduced. The device physics equations, which Sentaurus solves, depend upon the kind of simulations to be carried out, e.g., in the case of solar cells, either illumination conditions or applying a forward bias (named *dark simulation*). But are represented by the following system of semiconductor differential equations fully coupled and self-consistently:

$$\nabla \cdot (\xi \nabla \Psi) = -q \left(p - n + N_D^+ - N_A^- \right) \tag{2.10}$$

$$\frac{\partial n}{\partial t} = \frac{1}{q} \nabla \cdot \overrightarrow{J_n} + G - R \qquad \frac{\partial p}{\partial t} = -\frac{1}{q} \nabla \cdot \overrightarrow{J_p} + G - R \tag{2.11}$$

$$\overrightarrow{J_n} = -q\mu_n n \nabla \Psi + q D_n \nabla n \qquad \overrightarrow{J_p} = -q\mu_p p \nabla \Psi + q D_p \nabla p \tag{2.12}$$

where ξ is the permittivity and q is the elementary charge. J represents the electron and hole currents, μ the electron and hole mobilities, D is the diffusivities, and finally, G and R the photogeneration and recombination rates respectively.

Alternatively, analytical theories solve these equations only under specific conditions and with certain assumptions. For example, these equations may

be de-coupled (e.g., without the Poisson's equation in quasi-neutral regions), or inputs may be simplified (such as constant quasi-Fermi levels). Simulations, whether numerical or analytical, are used (i) to analyze experiments; (ii) to quantify losses in test samples or fabricated cells; (iii) for parameter studies; and (iv) to provide a roadmap for further experiments.

Chapter 3

Optical Modeling

The roughness formation over the surface, typically micrometer-sized pyramids, is an essential step to reach high-efficiency and cost-effectiveness *c*-Si solar cells, that PV industry satisfactory included in theirs production lines with the aim of minimizing light reflection, which is one of the principal optical loss factors on this kind of devices. Figure 3.1 illustrates some of the light-trapping concepts that photovoltaic manufacturers use nowadays to enhance the performance of their devices.

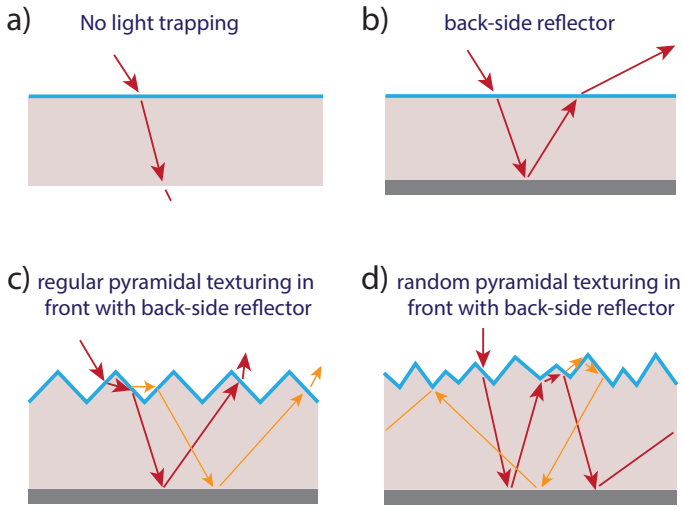

FIGURE 3.1: Illustration of light-trapping arrangements that industry use nowadays to improve light capture. **a)** No light trapping, **b)** back-side reflector, **c)** regular pyramidal texturing in front, and **d)** random front surface texturing.

The sketch in Fig. 3.1 a) shows a flat-surface type without any light enhancement mechanism. Meanwhile, Fig. 3.1 b) is also a cell with a polished surface, but it features a back-reflector that increases the light-path twice. On the other hand, solar cells presenting surface texturing, compared with polished ones, shown a better capability to absorb light, in fact, exhibit a reflectance reduction from $\sim$30 % (typically in flat surfaces) to less than 10 % when the light is incident from the air [136]. Rough-textured surfaces have a lesser reflective degree since the incident rays interact with the outer shapes of texturing several times, and already inside the device, the path length enlarges because

of the encouraging of multiple internal reflections. Figure 3.1 c) depicts a cell with a surface textured by regular upright pyramids, a ray that before to pass in that strikes the surface but bounces, it does in a particular angle (given by geometry of pyramids) causing to hit once more time a neighboring pyramid, which reduces the total reflection. On the other hand, within the device, long-wavelength photons (infrared light) that reflected from the rear surface back to front, encounter the angled silicon surface and again returns inside of the semiconductor, this effect is called "light trapping" [137], which is the mechanism that improves the absorption probability. In randomized surfaces, as in Fig. 3.1d), the light trapping is more efficient since the inner reflection path is larger because this surface structure better encloses the light within the device, [128, 129].

Currently, most of the commercial mono-crystalline silicon solar cells feature front surfaces textured with random arrays of pyramids with a height ranging from $1 - 10\ \mu\text{m}$. Commonly, the flat surface of the c-Si wafer is texturing by applying a wet anisotropic chemical etching process over the planar {100} surface of the devices that obtain a pyramidal roughness because it reveals the planes {111} of the silicon [138], as the Fig. 3.2 illustrates.

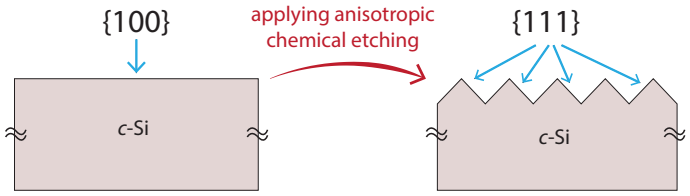

FIGURE 3.2: Illustration of the etch profile of the front surface of a solar cell {100} oriented after immersion in an anisotropic wet etching solution.

After the texturing step, a double-layer antireflection coating (ARC), formed either silicon nitride (SiN_x) or titanium oxide (TiO_x) combined with silicon oxide (SiO_2) is applied in such a way that covers the surface. The ARC is created by deposition, one on top of another, over the textured silicon surface to reduce even more the reflection losses [139, 140] and also passivate the semiconductor's surface.

The combination of both, surface texturing with the ARC layers, improve a lot a solar cell's ability to absorb light but, on the other hand, complicate the numerical assessment of its optics required to computational evaluate its inner working. The surface texture causes that light to reflect many times from the front surface. Thus, reflection, absorption, and transmission must be calculated for each "bounce" of light and combined correctly to determine the total reflection, absorption, and transmission. In so doing, it is necessary to calculate how the texture alters the angle of incidence and the polarization of the light. The complexity of the optical structure can be resolved by means geometrical ray tracing solver as long as the features of the simulation domain are significant enough to render diffractive effects negligible. To complicate matters further, the ARC layer introduces interference; therefore,

reflection, absorption, and transmission are dependents of the thickness, refractive index $\tilde{n}(\lambda)$ and extinction coefficient $\kappa(\lambda)$ that characterizes each material. Moreover, the interference depends on $\tilde{n}(\lambda)$ of the overlying layer and $\tilde{n}(\lambda)$ and $\kappa(\lambda)$ of the underlying semiconductor. Besides, the interference depends on the angle and polarization of the incident light, an ARC can consist of multiple thin-films, and $\tilde{n}(\lambda)$ and $\kappa(\lambda)$ can vary significantly with wavelength. In this chapter, it is in-depth analyzed the numerical evaluation of the optical behavior of IBC solar cells by using Sentaurus TCAD and present some interesting results regarding ARC optimization.

3.1 Determining the optical generation profiles

Simulation of PV devices under illumination requires an accurate modeling of light propagation and optical carrier generation within the absorbing material of solar cell. As discussed earlier in Sec. 2.5, the Illumination source file numerically coupling, by Sentaurus TCAD, to the simulation domain that contains the geometry structure, meshing and optical physics information of materials to calculate the photogeneration rate of electron-hole pairs by solving the transport equations. Before to resolving the semiconductor device equations for a device operating under illumination, it is necessary first to determine the spatial distribution of the optical generation rate as a function of the wavelength (λ) of the radiation. The solar spectrum file sweeps the wavelength of incident sunlight from the blue region of the spectrum ($300\,\mathrm{nm}$) up to the infrared region ($1200\,\mathrm{nm}$). The solar radiation goes into the simulator as a file created in base the conventional one-sun AM1.5G spectrum with an incident power of $1000\,\mathrm{W\,m^{-2}}$, defined in a text file that has a two-column format. The first column contains the wavelength in $\mu\mathrm{m}$ and the second one contains the intensity in $\mathrm{W\,cm^{-2}}$. This file is calculated based on the air mass 1.5 global tilted irradiance, by the spectral radiation model called SMARTS v 2.9.2 with inputs chosen per international standard IEC 60904-3-Ed2 [141]. The algorithm model allows selecting the frequency interval as well as the step to calculate the irradiance and cumulative photon flux to each wavelength keeping the integral of the intensity as close as possible to the measured. Figure 3.3 shown an example of the data input from $300\,\mathrm{nm}$ to $1200\,\mathrm{nm}$ with a frequency step of $40\,\mathrm{nm}$. The optical simulator also calculates the effectiveness in transmitting radiant energy (i.e., reflectance, transmittance, and absorbance) as a function of the wavelength (λ) of the radiation.

The key physical parameter, regarding optics, is the complex refractive index $\tilde{n}^*(\lambda)$, that describes how light propagates through the materials. The real part of it accounts for refraction, while the imaginary handles the attenuation. The complex refractive index model used in Sentaurus TCAD is expressed as:

$$\tilde{n}^*(\lambda) = \tilde{n}(\lambda) + i\kappa(\lambda) \tag{3.1}$$

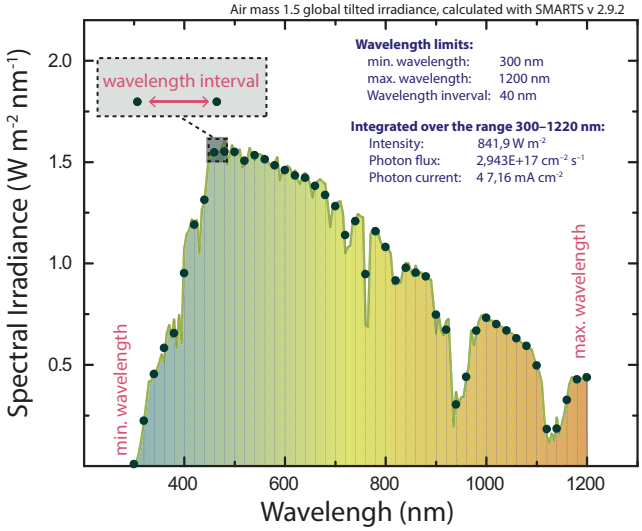

FIGURE 3.3: Air mass 1.5 global tilted irradiance, calculated with SMARTS v 2.9.2 acidifying to the standard IEC 60904-3-Ed2, from 300 to 1200 nm, with a wavelength step interval of 40 nm.

with:

$$\tilde{n}(\lambda) = n_0 + \Delta n_\lambda + \Delta n_T + \Delta n_{carr} + \Delta n_{gain} \tag{3.2}$$

$$\kappa(\lambda) = \kappa_0 + \Delta \kappa_\lambda + \Delta \kappa_{carr} \tag{3.3}$$

The real part, $\tilde{n}(\lambda)$, is composed of the base refractive index n_0, and some correction parameters including the dependency on wavelength, temperature, carrier density, and gain. The imaginary part, $\kappa(\lambda)$, is composed of the base extinction coefficient κ_0 , and the correction terms $\Delta\kappa_\lambda$ and $\Delta\kappa_{carr}$, correspond to the dependency on wavelength and carrier density. More details of the correction factors are discussed in [95].

Furthermore, the absorption coefficient α is computed from κ and wavelength λ according to:

$$\alpha = \frac{4\pi}{\lambda} \cdot \kappa \tag{3.4}$$

The absorption coefficient determines how far inside a material the light, with a particular wavelength, can penetrate before being absorbed to create electron-holes pairs. In materials with a low absorption coefficient or thin enough, light is inefficiently absorbed, and those will appear as transparent (depending on the wavelength). Semiconductor materials can only absorb energy from particles that have sufficient energy to excite an electron from the valence band to the conduction band.

A detailed and practical approach to optically modeling combines TMM method to account for thin-film effects with geometrical raytracing within the silicon,

previously mentioned in Sec. 2.5. It is important to highlight that the analysis limited to sufficiently large enough structures in which the diffraction effects are negligible [142].

3.1.1 Description of "raytracer" algorithm

In Sentaurus Device, the raytracer has been implemented based on linear polarization and optimized for fast calculation linked with the complex refractive index model introduced previously at the end of Sec. 3.1. Each material has a complex refractive index section defined in the parameter file. The raytracer solver uses a recursive algorithm: It starts with a source of rays and builds a binary tree that tracks the transmission and reflection of the rays. A reflection/transmission process occurs at interfaces with refractive index differences, illustrated in Fig. 3.4:

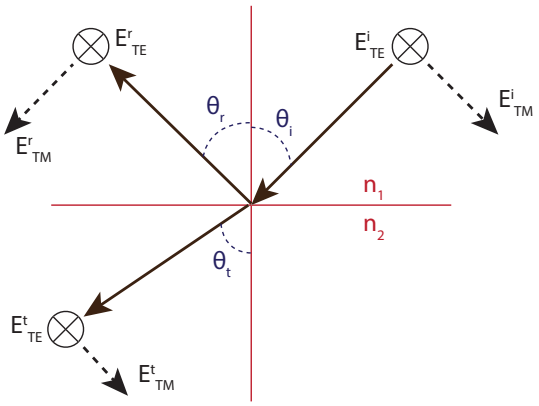

FIGURE 3.4: Incident ray splits into reflected and transmitted rays at an interface: the TE component of the polarization vector maintains the same direction, whereas the TM component changes direction. Image taken from [95].

Incident ray hits on the interface of two different refractive indexes (n_1 and n_2) regions, resulting in a reflected ray and a transmitted ray. The incident, reflected, and transmitted rays are denoted by the superscripts i, r, and t, respectively. Likewise, the incident, reflected, and transmitted angles are denoted by θ_i, θ_r, and θ_t, correspondingly. These angles can be derived from the concept of the interface tangential phase-matching (commonly called *Snell's law*) using:

$$n_1 \sin(\theta_i) = n_2 \sin(\theta_t) \tag{3.5}$$

To define these angles, a plane of incidence must be clearly determined. It is apparent that the plane of incidence is the plane that contains both the normal to the interface and the vector of the ray. When the plane of incidence is defined, the concept of TE and TM polarization can then be established. A ray can be considered as a plane wave traveling in a particular direction with

its polarization vector perpendicular to the direction of propagation. The length of the polarization vector represents the amplitude, and the square of its length denotes the intensity. The TE polarization (s-wave) applies to the ray polarization vector component that is perpendicular to the plane of incidence. On the other hand, the TM polarization (p-wave) refers to the ray polarization vector component that is parallel to the plane of incidence. In Fig. 3.4, the TE and TM components of the ray polarization vector are denoted by E_{TE} and E_{TM}, respectively.

The TE and TM components of the ray polarization vector experience different reflection and transmission coefficients. These coefficients are:

Amplitude reflection coefficients:

$$r_{TE} = \frac{\kappa_{1z} - \kappa_{2z}}{\kappa_{1z} + \kappa_{2z}} \tag{3.6}$$

$$r_{TM} = \frac{\epsilon_2\kappa_{1z} - \epsilon_1\kappa_{2z}}{\epsilon_2\kappa_{1z} + \epsilon_1\kappa_{2z}} \tag{3.7}$$

Amplitude transmission coefficients:

$$t_{TE} = \frac{2\kappa_{1z}}{\kappa_{1z} + \kappa_{2z}} \tag{3.8}$$

$$t_{TM} = \frac{2\epsilon_2\kappa_{1z}}{\epsilon_2\kappa_{1z} + \epsilon_1\kappa_{2z}} \tag{3.9}$$

Power reflection coefficients:

$$R_{TE} = |r_{TE}|^2 \tag{3.10}$$

$$R_{TM} = |r_{TM}|^2 \tag{3.11}$$

Power transmission coefficients:

$$T_{TE} = \frac{\kappa_{2z}}{\kappa_{1z}} |t_{TE}|^2 \tag{3.12}$$

$$T_{TM} = \frac{\epsilon_1\kappa_{2z}}{\epsilon_2\kappa_{1z}} |t_{TM}|^2 \tag{3.13}$$

where:

$$\kappa_0 = 2\pi/\lambda_0 \tag{3.14}$$

$$\kappa_{1z} = n_1\kappa_0 \cos(\theta_i) \tag{3.15}$$

$$\kappa_{2z} = n_2\kappa_0 \cos(\theta_t) \tag{3.16}$$

$$\epsilon_1 = n_1^2 \tag{3.17}$$

$$\epsilon_2 = n_2^2 \tag{3.18}$$

where λ_0 is the free space wavelength, and k_0 is the free space wave number. Note that for amplitude coefficients, $1 + r = t$. For power coefficients, $R + T = 1$. These relations can be verified easily by substituting the above definitions of the reflection and transmission coefficients of the respective TE and TM polarizations. For normal incidence when $\theta_i = \theta_t = 0$, $r_{TE} = -r_{TM}$, and $R_{TE} = R_{TM}$. The raytracer automatically computes the plane of incidence at each interface, decomposes the polarization vector into TE and TM components, and applies the respective reflection and transmission coefficients to these TE and TM components.

3.1.2 Simulation setup and definitions to extract the optical generation profiles

The optical simulation domains are 3D structures that consider three types of top surface geometry: flat, regular pyramid, and random pyramid, Fig. 3.5. The substrate is an *n*-type ($5\,\Omega\,\mathrm{cm}$) *c*-Si that features 10 x 10 x 280 µm with a back flat surface in all three cases. The doping profiles are Gaussian functions characterized by the parameters in Table 3.1.

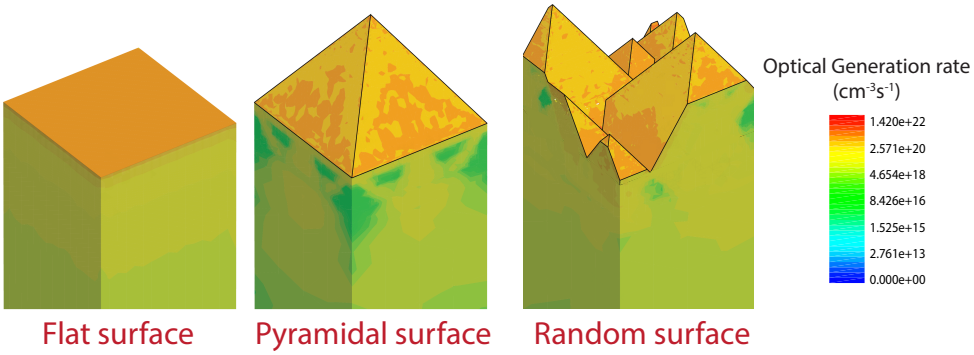

FIGURE 3.5: Visualization of the optical generation rate in three domains featuring different front texturing: flat, regular upright pyramidal, and random pyramidal.

Region	Doping peak	Junction depth
FSF	2.0×10^{19}	0.45 µm
BSF	1.7×10^{20}	1.00 µm
Emitter	5.0×10^{19}	1.00 µm

TABLE 3.1: Doping profiles parameters used for the optical simulations.

It is a common practice to select only a representative portion of a symmetric structure, often half of a symmetric element in two dimensions or a quarter

of the symmetric element in three dimensions. However, in this section, due to the asymmetric nature of the random-pyramid textured structure and considering the intention to maintain the same simulation domain for all three cases, such a simplification is omitted in the flat surface and regular-pyramid surface. It is worth mentioning that all the simulations have a gas layer on the top surface, and the anti-reflective coating (ARC) thin-layer composed of both silicon nitride (SiN_x) and silicon oxide (SiO_2) is introduced later as a raytracer boundary condition. The optical solver gives a photogeneration value to each mesh-grid point.

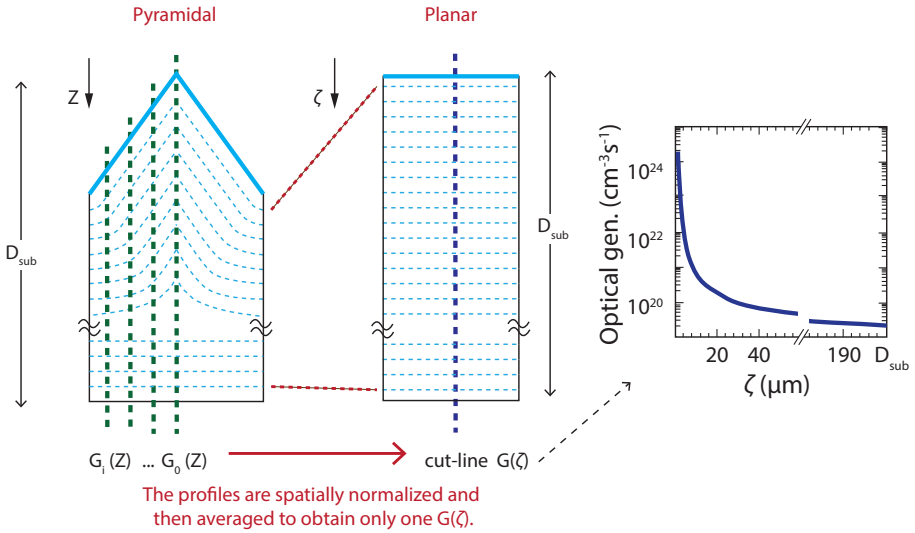

FIGURE 3.6: 2D representation of the normalization and averaging process to extract G(z) in the optical domain.

The generation rate $G(z)$, resulting from the optical simulation, is a 3D spatial function that expresses the inner charge generation produced by the light radiation in the optical domain. By interpolation through all the 3D mesh-grid points, and after averaged and normalized $G(z)$ becomes a one-dimensional spatial function $G(\zeta)$ [92, 143]. This resulting function becomes an input in the electrical domain which does not have texture but instead is flat, as in Fig. 3.6. Since the optical and electrical modeling does not have the same dimensions, neither equal meshing, the simulator interpolates $G(\zeta)$ to give each mesh-point a generation value. Currently, there are not precise analytical methods to predict the 1D profile, because of the complexity of the surface roughness. The analytical expression that defines $G(\zeta)$ is:

$$G(\zeta) = \frac{1}{MN} \sum_{i=1}^{N} \sum_{j=1}^{M} G(x_i, y_j, z) \frac{t_{i,j}}{D_{sub}} \tag{3.19}$$

where $G(x_i, y_j, z)$ is the profile extracted in the point (i, j) (of the plane $x - y$) with an depth from the surface to bottom $t_{i,j}$. The term D_{sub} refers to the substrate thickness of the electrical simulation domain. Meanwhile, M and N are the number of picked points in the axes x and y respectively.

Figure 3.7 show several examples of cut-lines taken from a regular pyramid, where the cuts are equally spatially distributed over the plane (x, y). It is worth seeing the different lengths caused by the irregularity in front shape, and the magnitude of the generation differ according to the position, generally is higher just in the middle of the pyramid, this effect is more notable in Fig. 3.9.

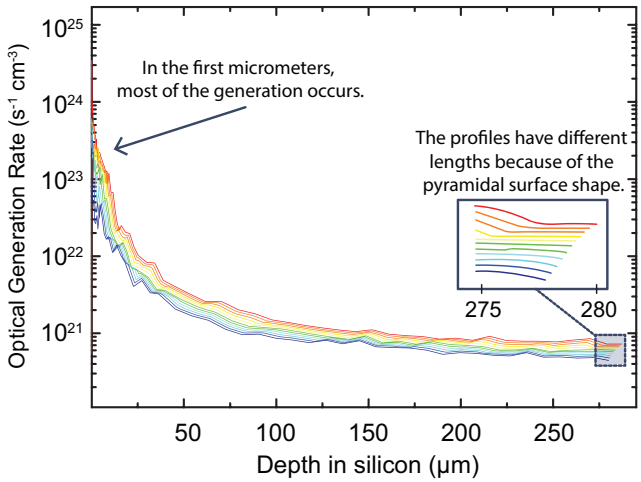

FIGURE 3.7: Optical generation profiles extracted in several positions of a pyramidal simulation domain, from the top of the pyramid to the bottom.

3.1.3 A faster method to extract optical profiles

This section presents a faster way to extract the optical generation profiles of a regular upright pyramid by using a linear interpolation only using two samples of the photogenerated current instead of normalizing and averaging, thousands $G(z)$ spatial cuts, previously discussed. The definition of photocurrent in a coordinate (x, y) is:

$$j_{ph}(x, y) = q \int_0^{t_{x,y}} G(x, y, z) dz \tag{3.20}$$

where q is the elemental charge, and $t_{x,y}$ is the silicon thickness in the point (x, y) from the top of the pyramid to the bottom, see Fig 3.8 b).

Sweeping the entire area (x, y) (through all the length L for both axes since the base is a square) of the pyramid, results in a contour map shown in Fig. 3.9 a). It is worth noting the photocurrent is higher right in the center of the pyramid and is due to the length of z is largest in the center for the pyramidal shape, and also there is an optical effect that concentrates the light at the focal point, that matches with the center of the pyramid. In Fig. 3.9 b), a longitudinal cut of the photogenerated current that pass just for the middle of pyramid is represented as spatial function of x.

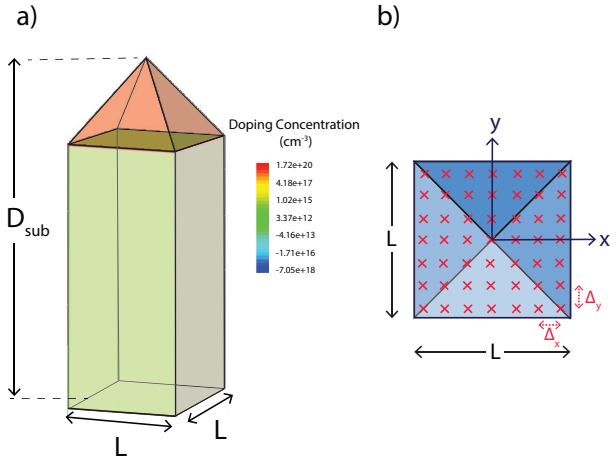

FIGURE 3.8: 3D Sketch of the optical simulation domain of of a cell with a upright pyramid and top view showing the coordinates of cut lines to extract the $G(x_i, y_j, z)$.

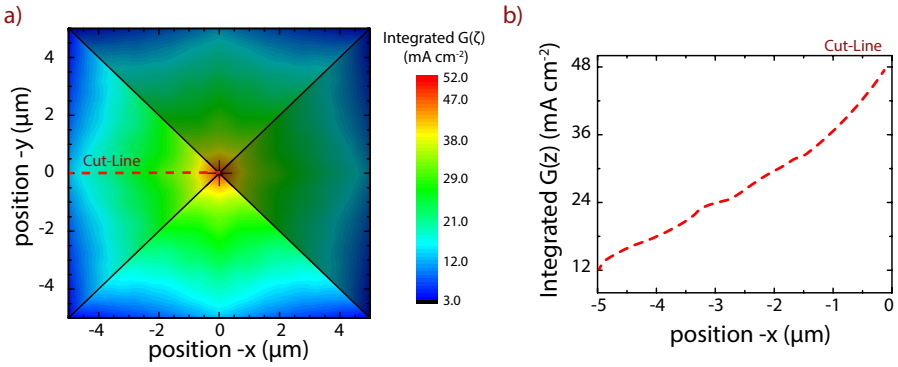

FIGURE 3.9: **(a)** Contour plot of photogenerated current integrating optical generation cut points, $G(x_i, y_j, z)$ in the whole pyramid, **(b)** Photogenerated current as a function of the position x along the center of the pyramid.

Keeping $y = 0$, and varying x from $-5\,\mu m$ to $0\,\mu m$ follows a linear trend as well as pyramidal shape that can be approximated with a straight-line equation as:

$$j_i = mx_i + j_0 \tag{3.21}$$

where j_0 is the photocurrent at the center of the pyramid (P_0) and $m = (j_1 - j_0)/x_1$.

By exploiting the high symmetry of the pyramid, Fig. 3.8 a), the total current in all the simulation domain can be expressed as the integral of j_i in one quadrant of pyramid multiplied by 4 as follows:

$$I_{TOT} = \int_0^{L/2} 4 d_i j_i(x) dx \tag{3.22}$$

where $d_i = 2x$, and L is the base length of the pyramid.

Solving this integral, the total current is:

$$I_{TOT} \approx L^2 \left(\frac{1}{3} mL + j_0 \right) \tag{3.23}$$

Keeping on mind all of these definitions, $G(\zeta)$ is expressed as:

$$G(\zeta) = G_0(z) \frac{I_{TOT}}{j_0} \tag{3.24}$$

Where the $G_0(z)$ is optical profile at P_0, I_{TOT} evaluated according Eq. 3.23, (j_0) is the photocurrent evaluated at P_0.

Calcualting the optical generation profile in that way reduces the computational time by a factor of 10x. This result is especially useful evaluating the optical effects when changes the size of the pyramids or quickly assesses variations in the thickness of the ARC layers to calibrate simulations with laboratory devices. A comparison between experimentally measurements, and extracted photogenerated currents by both methods traditional and proposed are practically identical as Table 3.2 shows. The calibration process

Photocurrent	**Symbol**	**Value** ($\mathrm{mA\,cm^{-2}}$)
Optical measure	j_{ph}	41.70
Electrical measure	j_{SC}	40.10
Classic simulation	j_{TOT}	40.54
Proposed simulation	j_{TOT}	40.52

TABLE 3.2: Photocurrent comparison between measurements, classic and proposed extraction models.

consists of entering in the simulations the measures of the complex refractive index and slightly adjusts the thickness of the ARC layers to reach the more similar reflectance and transmittance curves or calibrate by matching the photocurrent by wavelength as in Fig. 3.10.

The comparison of the two methods, traditional and new, are shown in Fig. 3.11. As shown in the figure the two profiles $G(\zeta)$ are quite similar, except in the calculation time. The corresponding photocurrent value is $40.54\,\mathrm{mA\,cm^{-2}}$ and $40.52\,\mathrm{mA\,cm^{-2}}$ for the standard and proposed method respectively. This validation confirms the accuracy of the approach suggested in this section, in spite of its significantly lower computational time.

Figure 3.12 shows the comparison between measured and simulated R and T spectra. Such frequencies are related to many simulations based on regular upright pyramidal front texturing. A good matching between experimental data and simulations confirms the high statistical robustness of the proposed optical model. After validating the optical approach the next step is to proceed with the electrical simulations.

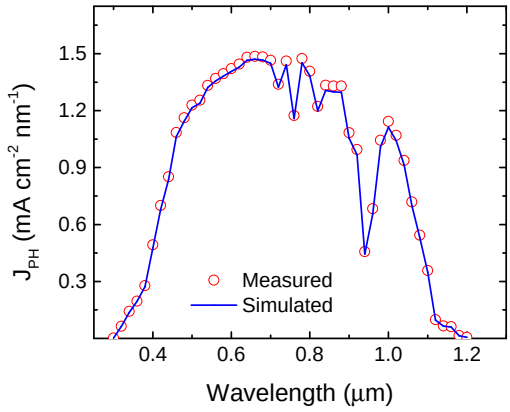

FIGURE 3.10: Photocurrent calibration.

3.2 Quantifying the Optical Losses

The calculation of the transmittance and the reflectance belongs to the standard tasks in the optical analysis of solar cell. When being incident to a thin-film system (in the case of this thesis the ARC layers), the electromagnetic wave first comes into contact with the coated surface by thin-film layers. Therefore, the first step in the understanding of the optical behavior of solar cells is to analyze what occurs with the light interactions at surfaces and interfaces. In the simulations, Sentaurus TCAD first calculates the reflectance and transmittance of the thin layers by using TMM method and then join this results as boundary conditions with Monte Carlo ray tracing solver. The optic optimization of IBC cell, as in any other kind of PV device, consists in maximize the light transmission from outside to inside the cell and enlarge the optical path length within the absorbent layers, by apply well-designed anti-reflection schemes and ensuring the highest possible back reflection.

The first reflectance results from the refractive index mismatch between the

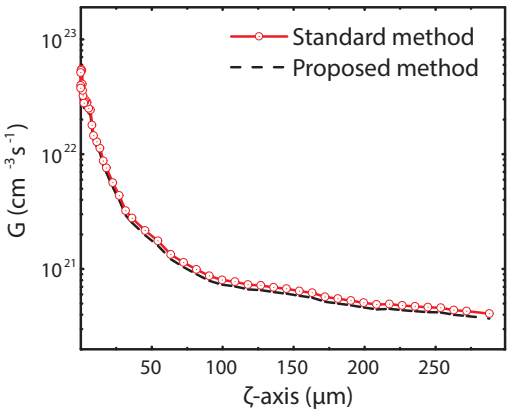

FIGURE 3.11: 1D optical generation profiles. In red line is the proposed method. In blue the classic method.

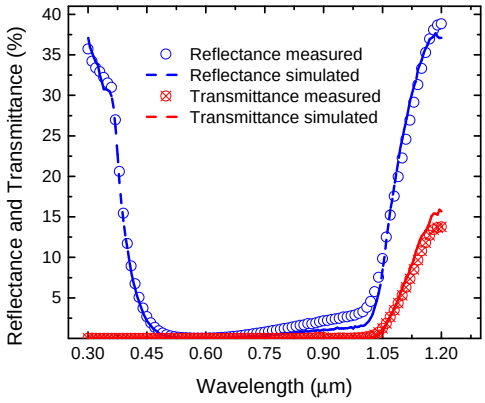

FIGURE 3.12: Simulation validation of reflectance and transmittance.

incident medium and device irradiated. Nevertheless, this undesirable effect can be diminished using either anti-reflective coatings (ARC) or front nano-texturing (Fig. 3.13). In the first case; one or more thin-film layers of the ARC produce a step-wise change of the refractive index from the air ($n_{air} = 1$) to:

$$n_{ARC} = \sqrt{n_{air}\, n_{i-layer}} \tag{3.25}$$

while the thickness d_{ARC} follows the principles of interference:

$$d_{ARC} = \frac{\lambda}{4} = \frac{\lambda_0}{4\, n_{ARC}} \tag{3.26}$$

where λ_0 is the wavelength in the vacuum, and the $\lambda/4$ rule ensures π radian phase shift between the air/ARC and ARC/i-layer reflectance, resulting in their cancellation at the designed wavelength. However, this technique is only indicative, since the ideal index may not correspond to any material and depending on the material chosen, a controlled thickness may be difficult to achieve. Furthermore, the wavelength range for which there is an actual decrease of the first reflectance is usually quite narrow. To widen such wavelength range, a multi-ARC could be fabricated by choosing specific materials and designing their thickness. The ARC coating technique is mostly applied over *c*-Si solar cells, where a thin layer of silicon nitride covers the front side of the wafer.

3.2.1 Optic Optimization of ARC layers in IBC solar cells

The optical optimization of IBC solar cells strongly depends on the materials' complex refractive index as mentioned before. However, from the design point of view, once optic characteristics of materials are characterized; the optimization only relies on the thickness of the ARC coatings [144]. In

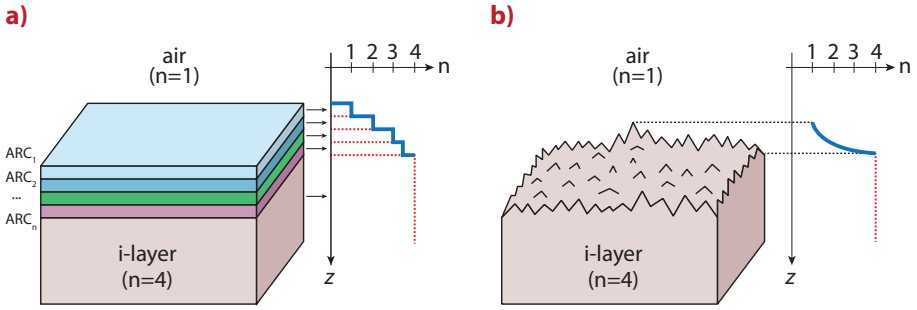

FIGURE 3.13: Anti-reflection schemes between air and i-layer: **(a)** multi ARC, giving step-wise refractive index matching, and **(b)** front nano-textured surface, giving gradual refractive index matching.

this section, it is analyzed the thickness optimization of the frontal ARC, in devices coated in both front and rear with SiO_2 and SiN_x. The optical parameters are reported in Table 3.3 assuming are placed by plasma-enhanced chemical vapor deposition (PECVD).

The considered front-texturing supposes isometric upright pyramids of $10\,\mu m$ in the base with a characteristic angle of $54.7°$. The complex refractive index of SiN_x, taken from literature, are plotted in Fig. 3.14 as functions of wavelength. It is worth mentioning that the SiO_2 do not actively vary for the preparation method [145]. Hence, the complex refractive index for the silicon-oxide remains fixed through all the simulations according to [146], as well as the rest of optical properties in the others of materials. In the front, the thickness of both SiO_2 and SiN_x range from 0.01 to $100\,nm$. Meantime, at rear, thicknesses remain fixed to $15\,nm$ and $100\,nm$ respectively.

Parameter	Name	Reference
c-Si at 300 K	Schinke2015	[147]
SiO_2	Pal85e	[146]
Al	AlPar	[146]
SiN_x	PECVD 1.92	[148]
SiN_x	PECVD 2.15	[148]
SiN_x	PECVD 2.37	[148]
SiN_x	PECVD 2.61	[148]
SiN_x	PECVD 2.71	[148]
SiN_x	PECVD Bak11	[149]

TABLE 3.3: Reference of the Optical parameters used for the simulations.

Figure 3.15 shows the results of the simulated optical losses, expressed as the potential photogeneration current density ($mA\,cm^{-2}$) in function of front-surface ARC thickness. Since PECVD 2.71 has the highest absorption coefficient, it also which most affects the photogenerated current (see the color variation). According to the simulations, a device that has $80\,nm$ SiN_x (PECVD 2.71) and $90\,nm$ of SiO_2 could reach a $27.82\,mA\,cm^{-2}$ of photocurrent. Meanwhile, the same structure, but with and optimized ARC, could give $41.84\,mA\,cm^{-2}$

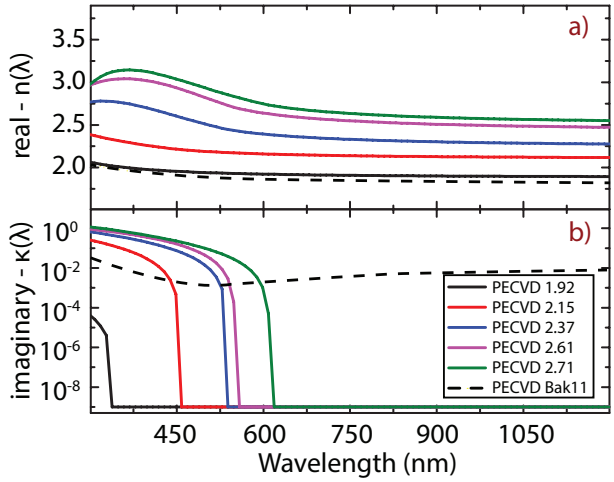

FIGURE 3.14: **a)** Real and **b)** imaginary refractive index of the SiN_x coatings taken from the literature, Table 3.3.

of photocurrent, with $1\,\mathrm{nm}$ SiN_x and $90\,\mathrm{nm}$ of SiO_2. It finally resulting in an improvement of $14.02\,\mathrm{mA\,cm^{-2}}$ respect the structure without optimization.

Optimizing the ARC thickness, of cell featuring PECVD 2.71 in the front, could lead an improvement bigger than $14.92\,\mathrm{mA\,cm^{-2}}$, if it is considered an initial ARC thickness of $80\,\mathrm{nm}$ to a redefined $1\,\mathrm{nm}$ of SiN_x. In Table 3.4 are summarized the optimal thickness values according to the nitrate parameter.

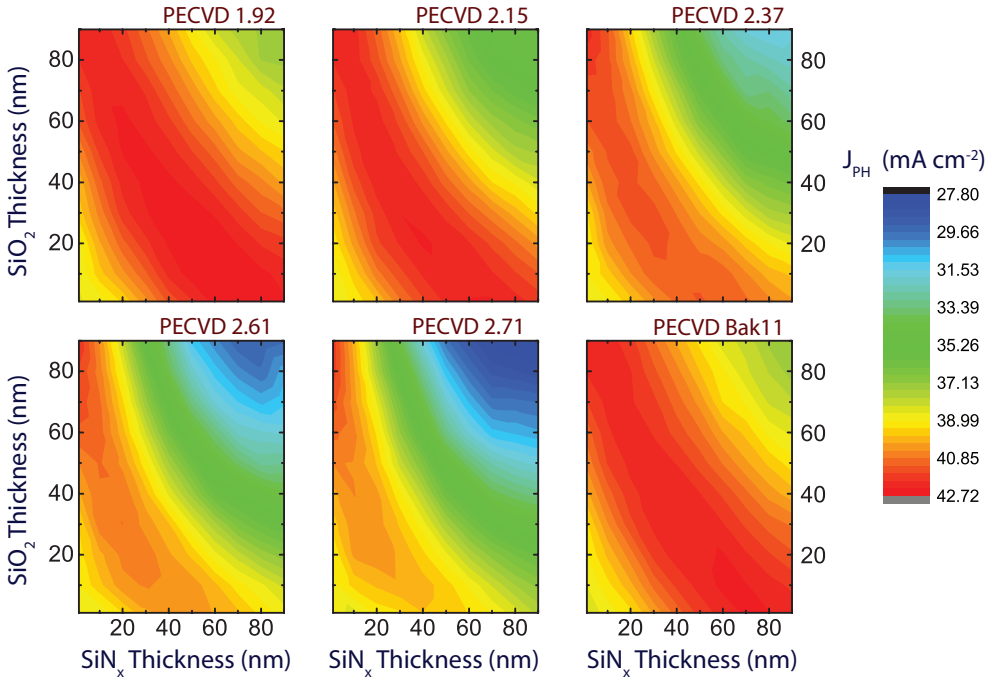

FIGURE 3.15: Modeled optical losses, expressed as a potential photogeneration current density, J_{ph} $(\mathrm{mA\,cm^{-2}})$, as a function of front-surface ARC thickness. The optical parameters of SiN_x are in Table 3.3.

Parameter	SiN_x Thickness (nm)	SiO_2 Thickness (nm)	$J_{ph}(\mathrm{mA\,cm^{-2}})$
PECVD 1.92	60.0	10.0	42.71
PECVD 2.15	40.0	20.0	42.40
PECVD 2.37	1.0	90.0	42.17
PECVD 2.61	1.0	90.0	41.93
PECVD 2.71	1.0	90.0	41.84
PECVD Bak11	60.0	10.0	42.45

TABLE 3.4: Optimum thickness of the ARC layer

3.2.2 Analysis of surface texturing: flat, regular, and random

In Fig. 3.16, the generation profile $G(\zeta)$ is plotted for a range of pyramidal textures under the AM1-5g spectrum: flat, regular upright pyramids, and random uprights pyramids. In each case, the modeled structure is a silicon substrate of $280\,\mu\mathrm{m}$ thickness, coated with an optimal thick layer of reported in Table 3.4 for PECVD 1.92. The feature height of each regular texturing is $10\,\mu\mathrm{m}$. Meanwhile, each randomly distributed pyramid has a height of from 5 to $10\,\mu\mathrm{m}$, where the pyramid heights vary randomly, following a uniform distribution within this range. The model used to approximate the random upright pyramid morphology is discussed [150]. The simulations take into account internal reflections and successive traversals of the substrate by each light ray by assuming that lateral boundaries are perfect reflectors.

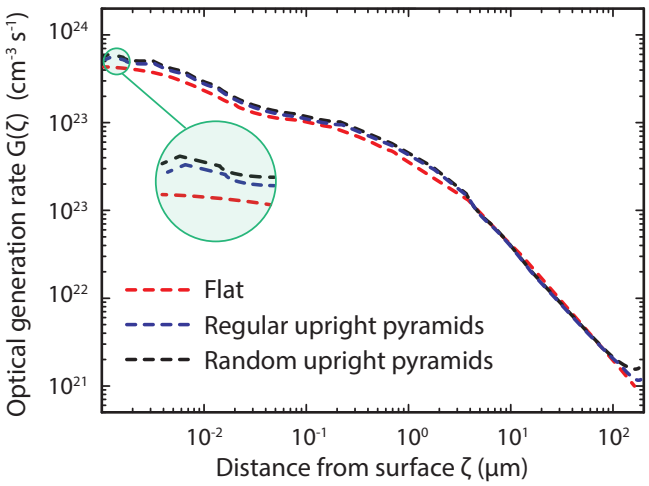

FIGURE 3.16: $G(\zeta)$ of three front surfaces texturing: flat, regular upright, and random using raytracer. The optical simulation feature 10x10x280 µm.

It is worth mentioning that any variation in the back-surface properties in the simulation domains is relatively unimportant in this analysis, in which the aim is centering in the impact of the texturing, rather than absolute values of efficiency. When compared to an equivalent structure with a planar

front surface, all textures increase the density of carrier generation in the several microns of the substrate closest to the foremost surface. This effect, illustrated in Fig. 3.16, is because of the reduction in front surface reflectance due to the multiple encounters of the ray with the absorber material (see Fig. 3.1). However, it is also due to the tendency of the texture to refract rays away from the local surface normal. A random array of pyramids causes the largest increase in G within the near-surface region. For $\zeta < 3\,\mu\mathrm{m}$, the generation rate beneath this texture is higher than the rate beneath other morphologies. This is attributable to the superior transmittance of the pyramids as well as to the refraction of rays into oblique angles of traversal. At $\zeta = 3 - 5$ $\mu\mathrm{m}$, G beneath this morphology decreases steeply because, on average, for a given interval of distance throughout the ray trajectory, ζ increases by a larger amount when that interval is in the bulk region of the cell than in the area of the pyramid.

Chapter 4

Electrical modeling

Once the optical generation profile, $G(\zeta)$, is calculated by the procedure described in the previous chapter, it goes in as an input parameter to the TCAD simulator. As mentioned before, the results in this work are mainly centered on IBC architecture, which is currently one of the most attractive structures that PV community is focused on because all the advantages already mentioned in this thesis. $G(\zeta)$ is a one-dimensional spatial function that by linear interpolation Sentaurus TCAD gives to each mesh point of the simulated structure (either 2D or 3D) a generation value to solve the semiconductor equations (Sec 2.7) of the devices operating under illumination conditions. In dark analysis, the simulator performs voltage sweeps to calculates the output current density in the absence incident sunlight. It is worth noting that the simulation results critically depend on the setting of the boundary conditions at device interfaces (e.g., at contacts and passivated surfaces) and of the physical models and parameters implemented in the simulator, Sec. 2.3.

4.1 Emitter coverage optimization in IBC solar cells

An important design parameter of IBC solar cell is the emitter coverage (R), defined as the ratio between emitter width divided by the rear pitch length. Several works have suggested different optimal values for the emitter coverage ratio (R_{opt}) to reach maximum efficiencies [151, 152], ranging from 0.7 to 0.8. The trade-off between the so-called electrical shadowing effect and series resistance losses explains the existence of R_{opt} [96]. The aim of this section is to present an analysis that heading toward a better understanding of the dependence the dependence of R_{opt} on the main physical and geometrical parameters of IBC solar cells by exploiting TCAD simulations to finally respond the question: is there a single optimal emitter coverage fraction in IBC solar cells?

4.1.1 Simulation setup to evaluate the emitter coverage

This section presents the setup details of simulations to evaluate the emitter coverage impact over the behavior of IBC solar cells by means 2D TCAD simulations. Figure 4.1 shows an illustrative sketch of the implemented element of symmetry of the electrical simulation domain. The model is calibrated as $200\,\mu m$-thick *c*-Si substrate *n*-type, floating zone (FZ). The doping profiles of BSF, FSF and emitter are Gaussian functions of the spatial coordinate featuring its doping-peak at the border edge of the device with an effective in-diffusion in the substrate of $1\,\mu m$ for FSF, and $2\,\mu m$ for both emitter and BSF. The front and rear surfaces consider a double-layer anti-reflective coating (ARC) composed by Si_3N_x and SiO_2 with optimum thickness reported in Table 3.4 for PECVD 2.37. While the uppermost surface texturing has regular upright pyramids featuring a $10\,\mu m$ base and a characteristic angle equal to $54.7°$, the back interface is flat. For all the simulations, both gap space (GAP) between BSF and emitter, and the FSF doping-peak are maintained to $5\,\mu m$ and $2.51 \times 10^{18}\,cm^{-3}$ respectively. The metal resistance, i.e., fingers and busbars are not considered by the TCAD simulation directly but as lumped series resistance in a post-processing calculation.

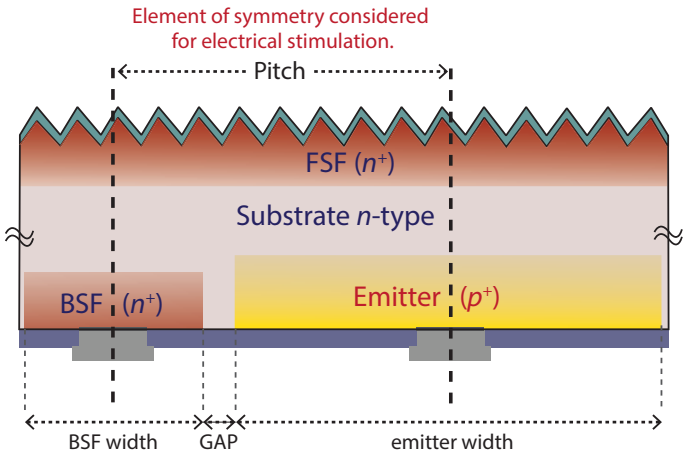

FIGURE 4.1: Sketch of the electrical simulation domain of IBC solar cell used to analyze the emitter coverage.

A wide set of experiments was performed considering the following parameters ranges: both emitter and BSF doping-peaks varying from 1×10^{18} to $1 \times 10^{21}\,cm^{-3}$, the widths of the pair BSF and emitter varying from $55\,\mu m$ to $300\,\mu m$ and from $90\,\mu m$ to $1600\,\mu m$ respectively. The simulations take into consideration two substrate quality: $1\,\Omega\,cm$ and $10\,\Omega\,cm$. Table 4.1 summarizes the mentioned parameters ranges. The main investigated parameter is R_{opt}, which represents the value of R required to maximize the efficiency for each analysis.

The variation of such an extensive number of parameters leads a large nonsense data set, so to comprehensive visualize the results, the graphs represent the shift of only two parameters simultaneously; meanwhile, the others

remain fixed. Therefore, R_{opt} is a relative optimum and not the absolute optimum.

Parameter	Range	Units
Emitter doping-peak	1×10^{18} - 1×10^{21}	cm^{-3}
BSF doping-peak	1×10^{18} -1×10^{21}	cm^{-3}
BSF width	55 - 300	µm
Emitter width	90 - 3000	µm
Bulk resistivity	1 or 10	$\Omega\,\mathrm{cm}$

TABLE 4.1: Summary of the range of parameters used to evaluate R_{opt}.

4.1.2 Emitter coverage: results and discussion

Figure 4.2 shows two contour surfaces of R_{opt} as a function of both emitter and BSF doping-peaks, by keeping fixed the pitch ($685\,\mu\mathrm{m}$) and BSF width ($55\,\mu\mathrm{m}$) in two quality substrates $1\,\Omega\,\mathrm{cm}$ (a) and $10\,\Omega\,\mathrm{cm}$ (b) featuring $1337.8\,\mu\mathrm{s}$ and $1913.7\,\mu\mathrm{s}$ of charges lifetimes respectively. In each graph, the efficiency is represented by dotted lines that enclosing the regions with maximum efficiencies, dependent of doping-peaks. The emitter width varies in such a way that R ranging from 0.6 to 0.95.

The graphs reveal that, for the two qualities of substrates, there exists a stout relationship between the doping-peaks (of both emitter and BSF) and the efficiency, that not follows any trend of R_{opt}. The maximum efficiency is quite insensitive to geometry, in fact, as [85] discussed, there are optimum values of BSF and emitter doping levels, which do not depend on each other and are invariant to geometrical parameters or substrate quality.

Continuing with the analysis, for the substrate quality of $1\,\Omega\,\mathrm{cm}$ ($10\,\Omega\,\mathrm{cm}$) the doping concentrations of BSF and emitter remain fixed to their optimal doping-peaks: $2.51 \times 10^{20}\,\mathrm{cm}^{-3}$ ($6.31 \times 10^{19}\,\mathrm{cm}^{-3}$) and $1.58 \times 10^{19}\,\mathrm{cm}^{-3}$ respectively. Figure 4.3 presents the results of the performed simulations to analyze R_{OPT} as function of three geometric parameters: rear pitch, BSF-width, and emitter width. The value of R_{opt} increases with both pitch and emitter width, while it significantly decreases respect to BSF width. R_{opt} ranges again between 0.60 to 0.95. For the case of a substrate resistivity $1\,\Omega\,\mathrm{cm}$ ($10\,\Omega\,\mathrm{cm}$), the absolute maximum efficiency is $23.08\,\%$ ($22.96\,\%$) which corresponding to R_{opt} of 0.91 (0.81).

Figure 4.4 show the efficiency as a function of variation both sizes: BSF and emitter, keeping constant the doping profiles to their optimal values for the two substrate qualities. It is worth noting that both widths BSF and emitter can be optimized independently from each other. In the case of a substrate resistivity of $1\,\Omega\,\mathrm{cm}$ ($10\,\Omega\,\mathrm{cm}$), the ideal BSF width is $55\,\mu\mathrm{m}$ ($100\,\mu\mathrm{m}$), and the emitter width is $646\,\mu\mathrm{m}$ ($448\,\mu\mathrm{m}$). These optimal dimensions result from the

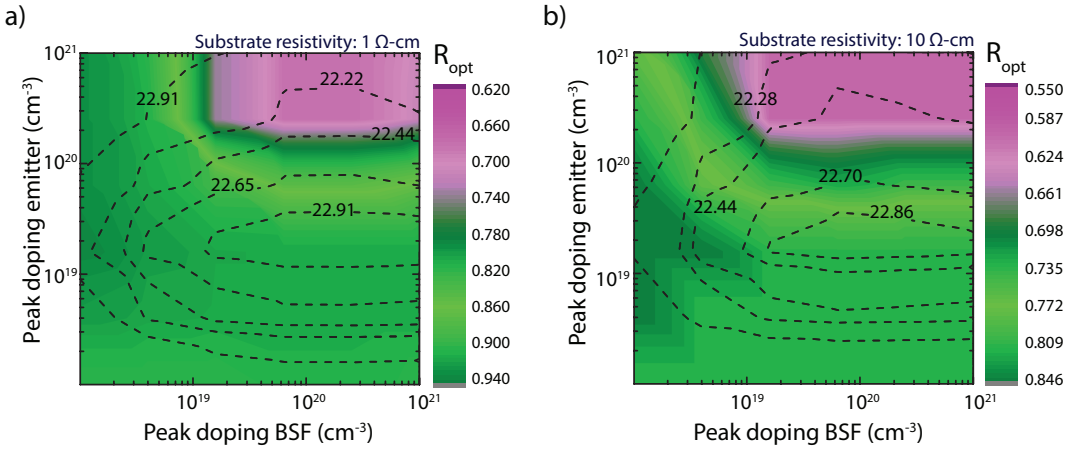

FIGURE 4.2: In color: the simulated R_{opt} as function of both doping peaks BSF and emitter. Dotted lines: efficiency also as a function doping-peaks. **a)** Simulations evaluated in a $1\,\Omega\,\mathrm{cm}$ substrate, featuring a BSF width equal to $55\,\mu\mathrm{m}$. **b)** Simulations results evaluated in a $10\,\Omega\,\mathrm{cm}$ substrate, with a BSF size of $100\,\mu\mathrm{m}$.

trade-off between the so-called electrical shading effect [88, 153] and the internal series resistance of the device. The electrical-shading losses decrease by increasing the emitter width and by reducing the BSF width, while the series resistance losses became higher by enlarging the emitter and reducing BSF dimensions. By comparing Fig. 4.4 a) and 4.4 b), it is evident that by increasing the substrate resistivity, the optimum BSF width increases due to the stronger contribution of substrate to total series resistance losses.

The R_{opt} value exhibits a high-dependence on emitter and BSF doping profiles, pitch, emitter and BSF widths, and bulk resistivity, ranging from 0.60 to 0.95. From the geometry design perspective, it is more efficient optimizing the BSF and emitter widths than optimizing R at fixed pitch or BSF width independently. In the case of a substrate quality of $1\,\Omega\,\mathrm{cm}$ ($10\,\Omega\,\mathrm{cm}$), the obtained absolute maximum efficiency is $23.08\,\%$ ($22.96\,\%$) with a cell featuring a BSF width $55\,\mu\mathrm{m}$ ($100\,\mu\mathrm{m}$) and emitter width of $646\,\mu\mathrm{m}$ ($448\,\mu\mathrm{m}$), which give a pitch of $706\,\mu\mathrm{m}$ ($553\,\mu\mathrm{m}$) and R_{opt} of 0.91 (0.81). Responding to the beginning question if there exists a unique R_{opt}, the answer is: NO.

4.2 Design guidelines for a metallization scheme with multiple emitter contact lines in IBC solar cells

This section presents a study on back contact-back junction solar cells when using a metallization scheme with multiple-emitter contact lines. For this

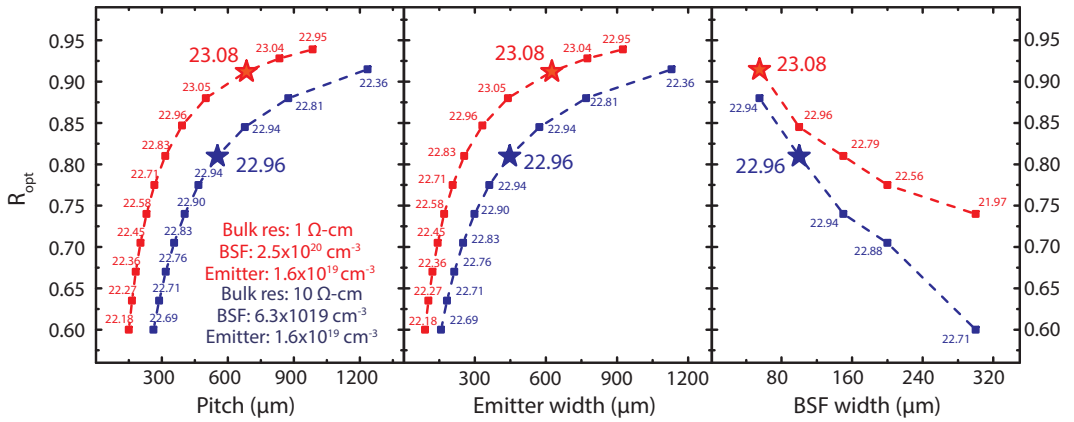

FIGURE 4.3: Curve results of R_{opt} as function of the three parameters: simulation pitch (left), emitter width (middle), and BSF width (right). The numbers above points are the efficiencies. In red, are the results corresponding to a substrate quality of $1\,\Omega\,\mathrm{cm}$, meanwhile in blue those for $10\,\Omega\,\mathrm{cm}$.

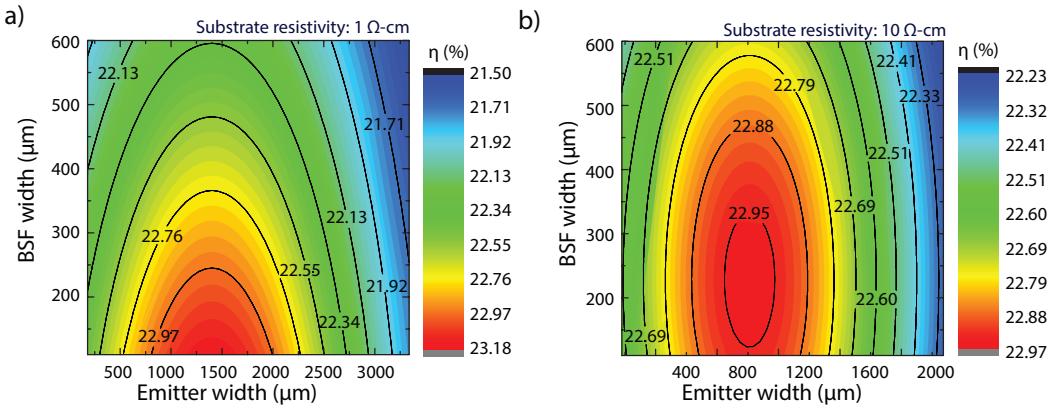

FIGURE 4.4: Results of the efficiency as function both size widths BSF and emitter, independently optimized one each other. **a)** and **b)** corresponds to the substrate quality.

purpose, TCAD based simulations have been carried out by taking into account realistic parameters and state-of-the-art physical models for silicon solar cells. The analysis has been performed by varying different geometrical parameters related to rear metallization, such as the number of the emitter contacts and the emitter metal coverage. In general, an efficiency improvement has been observed by uniformly placing the multiple contacts along the emitter region and by increasing the number of the emitter metal lines. An optimal emitter metallization fraction has been found for different numbers of contacts as a result of the trade-off between recombination losses at metal/silicon interfaces and series resistance losses. Moreover, the effect of the multiple-emitter contacts has been evaluated as a function of the finger length, the emitter width, and the rear pitch.

4.2.1 Simulation setup to evaluate multiple emitter contacts

The developed electrical model assumes a $200\,\mu m$-thick *c*-Si FZ *n*-type substrate, featuring a resistivity $5\,\Omega\,cm$ [154]. the front interface is texturing with typical randomized pyramids starring a characteristic angle $54.7°$, and covered by an anti-reflective (ARC) composed by SiN_x and SiO_2 with the optimum thickness reported in Table 3.4 for PECVD 2.37. The back interface, instead, is flat but passivated with a thin-layer of SiO_2. The doping profiles of BSF, FSF and emitter regions are approaching by Gaussian spatial functions with parameters reported in Table 4.2. For all the simulations the GAP space is fixed to $0.1\,\mu m$.

Region	Doping-Peak	Junction Depth
BSF	$1.70 \times 10^{20}\,cm^{-3}$	$0.80\,\mu m$
FSF	$3.47 \times 10^{18}\,cm^{-3}$	$0.45\,\mu m$
Emitter	$5.00 \times 10^{19}\,cm^{-3}$	$1.00\,\mu m$

TABLE 4.2: Characteristic parameters of spatial Gaussian doping-profiles used to analyze metallization.

As mentioned earlier in Sec. 2.7, the electrical simulation model (sketched in Fig. 4.1) is based on the solution of the drift-diffusion equations' couple with the Poisson's equation limited on the standard simulation domain by applying a finite-element method. Fermi-Dirac statistics has been assumed to properly model the highly doped regions such as BSF, emitter and FSF. Moreover, different physical models and parameters have been accurately tuned to meet the requirements for simulating *c*-Si solar cells by taking into account more realistic state-of-the-art parameterizations [104]. Among these, the chosen one to modeling the band-gap narrowing (BGN) model is that proposed by Schenk in [106], the mobility model proposed by Klaassen [107], the intrinsic recombination related to Coulomb-enhanced Auger and radiative recombination models proposed by Richter *et al.* [23], the doping-dependent trap-assisted Shockley-Read-Hall (SRH) bulk and surface recombination models related to defects in the silicon substrate [108] and at passivated interfaces [109], respectively. The band-gap model parameters have been adjusted to match an intrinsic carrier density of $9.65 \times 10^{9}\,cm^{-1}$ at $300\,K$ [56]. The surface SRH recombination velocity at metal/silicon interfaces has been set to $1 \times 10^{7}\,cm\,s^{-1}$, close to the thermal velocity [104]. All of these parameters were previously detailed through Chap. 2 and summarized in Table 2.1.

With the aim of evaluating the effects of different emitter metallization schemes (introduced in 2.6), the adopted resistive model accounts for the series resistance effect due to metallization as a function of the following parameters: finger length (L_f), metal contact thickness (t_C), contact width (W_C) and number of emitter linear contacts ($N_{C,em}$), as shown in Fig. 4.5.

An extensive set of experiments has been performed by varying the emitter metallization parameters and the emitter width within the ranges reported

Parameter	Range	Units
W_{em}	100 - 1100	0.80 µm
$M_{F,em}$	0.01 - 0.6	0.45 µm
$N_{C,em}$	100 - 1100	1.00 µm
L_f	100 - 1100	1.00 µm

TABLE 4.3: Characteristic parameters of spatial Gaussian doping-profiles used to analyze metallization.

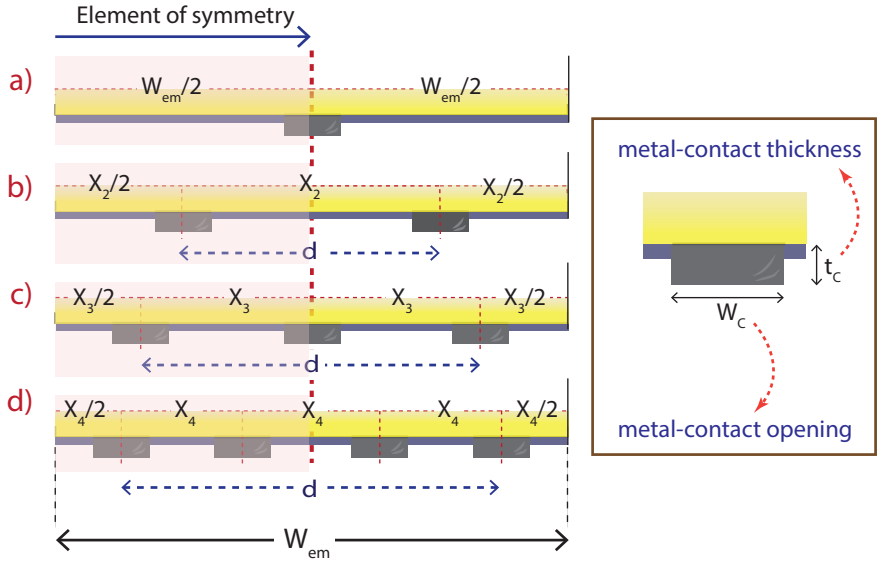

FIGURE 4.5: Illustration of the multiple metallization patterns in the emitter region: **a)** single-emitter contact, **b)** 2-emitter contacts, **c)** 3-emitter contacts, and **d)** 4-emitter contacts. On the right side, it is an sketch graphically showing W_C and L_F.

in Table 4.3. It is worth noting that in the performed analysis the width of the BSF region (W_{BSF}) and of the BSF contact ($W_{C,BSF}$) have been kept constant to the values of$60\,\mu m$ and $50\,\mu m$, respectively, according to the results reported in [155], while the BSF and emitter contact thickness has been set to $2\,\mu m$. Therefore, by the chosen emitter parameters, it is advantageous introducing a parameter called emitter metallization fraction ($M_{F,em}$), which is defined as the ratio of the emitter metallized area to the total emitter area as follows:

$$M_{F,em} = N_{C,em} \cdot \frac{W_{C,em}}{W_{em}} \tag{4.1}$$

where W_{em} is the emitter width and $W_{C,em}$ is the emitter contact width.

In particular, the series resistive losses due to metallization, which include both metal finger and metal/silicon contact resistance contributions, have been modeled through a distributed resistance [156] expressed in $\Omega\,cm^2$:

$$r_L = r_M + r_C \tag{4.2}$$

where r_M is the resistance contribution due to the metal finger and r_C is the resistance contribution due to the contact interface resistance. It is worth noting that these resistance contributions are weighted along the active cell area. In Fig. 4.6 is sketched the metallization structure of an IBC cell with the implemented 2D simulation domain, which supposes is centered on the metal fingers. In average, each metal finger has a resistance expressed as:

$$R_{M,av} = \frac{1}{L_f}\int_0^{L_f} \rho_{Al}\frac{L_f - x}{W_C \cdot t_C}dx \tag{4.3}$$

where ρ_{Al} is the resistivity of the aluminum. After solving the integral:

$$R_{M,av} = \frac{\rho_{al}}{L_f \cdot W_C \cdot t_C}\frac{L_f^2}{2} \tag{4.4}$$

Since the area that is contact with the semiconductor is $A_{cont} = w_C \cdot L_f$, the weighted resistance contribution of each metal finger results in:

$$r_M = \frac{\rho_{Al} \cdot L_f^2}{2 \cdot t_C} \tag{4.5}$$

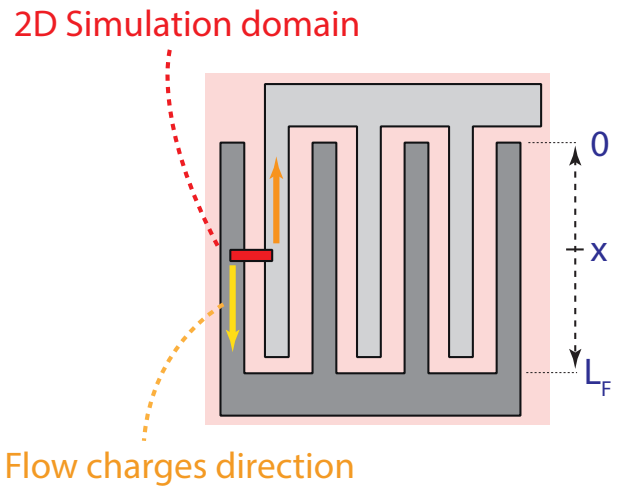

FIGURE 4.6: Sketch of the metallization, it shows the implemented 2D simulation domain with the trajectory of the charges flow.

According to Eq. 4.2, the distributed resistance r_L on each region, either BSF and emitter, are expressed as the sum of both resistance contributions, i.e., the specific-contact and the calculated for each metal finger on Eq. 4.5:

$$r_{L,BSF} = \frac{\rho_{Al} \cdot L_f^2}{2 \cdot t_C} + \rho_{C,BSF} \tag{4.6}$$

$$r_{L,em} = \frac{1}{N_{C,em}} \cdot \left(\frac{\rho_{Al} \cdot L_f^2}{2 \cdot t_C} + \rho_{C,em} \right) \tag{4.7}$$

where $\rho_{C,BSF}$ and $\rho_{C,em}$ are the specific contact resistivity in the BSF and emitter regions, respectively. It is worth mentioning that the extra factor, $1/N_{C,em}$ in Eq. 4.7, is for considering the effect of adding more emitter metal lines, which electrically act like resistors in a parallel configuration. Table 4.4 reports the considered values for such parameters taken from [111].

Parameter	Value	Units
$\rho_{C,em}$	3.90×10^{-3}	$\Omega\cdot cm^2$
$\rho_{C,BSF}$	2.20×10^{-3}	$\Omega\cdot cm^2$
ρ_{Al}	2.65×10^{-6}	$\Omega\cdot cm$

TABLE 4.4: Considered resistivity values to eluate multiple emitter contacts.

4.2.2 Evaluation of multiple emitter contacts: Results and Discussion

With the aim of investigating the dependence of the conversion efficiency versus the contacts position, a set of simulations has been performed by changing the contacts placing along the emitter region for each $N_{C,em}$. It is worth noting that, for symmetry purposes, in the case of a single emitter contact, such a contact is placed in the middle of the emitter region, as shown in Fig. 4.5 a). In the case of multiple contacts, the parameter d represents the distance between the centers of the outermost contacts, as Fig. 4.5 b), 4.5 c), and 4.5 d) illustrate. Fig. 4.7 shows the efficiency as a function of the normalized ratio d/W_{em} ranging from 0.1 to 0.9 for a different number of emitter contacts. The efficiency curves show a bell-shaped trend with a clear optimum at a certain d/W_e value. Notice that, W_{em}=1100 µm and $M_{F,em}$=0.025 remain constants through this analysis, to evaluate the effect of distribution contacts, but without changing recombination losses at the rear side.

In fact, only changing the emitter contacts position, the invariant recombination losses entail constant J_{SC} and V_{OC}. On the contrary, the series resistance losses related to the lateral carrier transport and hence the *FF* are affected by the contacts position, thus leading to the observed bell-shaped trend on the efficiency curves. In particular, we demonstrate that the equidistant distribution of contacts along the emitter region is mandatory to minimize such resistive losses and, consequently, to maximize *FF* and η. As a matter of fact, for the case of 2-emitter contacts and according to [157], the optimum

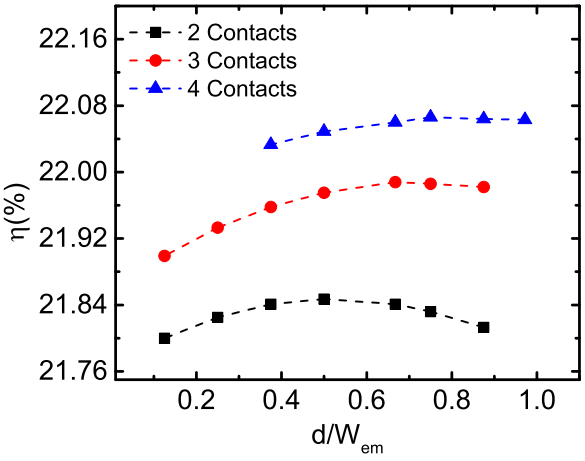

FIGURE 4.7: Efficiency as function of d/W_{em} ratio for the case of multiple-emitter contacts. Black, red, and blue colors represent the cases of 2-, 3-, and 4-emitter contacts respectively. W_{em} =1100 µm and $M_{F,em}$ =0.025 remain fixed.

d/W_{em} is 0.5 (see Fig. 4.7), which corresponds to the equidistant distribution of the two contacts along the emitter region. Accordingly, for the cases of 3- and 4-emitter contacts, the optimum value shifts to be larger d/W_{em} since the equidistant distribution of contacts is obtained by increasing the distance between the outermost contacts, thus leading to an optimal d/W_{em} equal to 0.67 and 0.75, respectively (see Fig. 4.7). As a result of this analysis and according to Fig. 4.5, to maximize the conversion efficiency, the distance between the centers of two adjacent emitter contacts in the case of n linear contacts has to follow this expression:

$$X_n = \frac{W_{em}}{N_{C,em}} \tag{4.8}$$

Moreover, it is worth pointing out that such a result is independent from the considered W_{em}. However, the equidistant distribution of emitter contacts is more effective for larger W_{em}.

4.2.3 Evaluation of emitter metallization fraction and finger length

This section, reports and discuss the results of the performed analysis on the influence of the emitter metallization fraction ($M_{F,em}$) over the principal solar cell figures of merit (FOMs). To this purpose, the analysis has been carried out by varying the emitter contact width ($W_{C,em}$), the number of emitter contacts ($N_{C,em}$) and, consequently, the $M_{F,em}$, and by considering W_{em}= 300 µm and L_f=1.5 cm.

Fig. 4.8 shows the results in terms of J_{SC}, V_{OC}, *FF* and η as a function of $M_{F,em}$. The decrease trend of both J_{SC} and V_{OC} is due to enlargement of recombination losses at rear metallized interfaces ($M_{F,em}$ increases). As expected, observing J_{SC} and V_{OC} trends for different $N_{C,em}$ at the same $M_{F,em}$, negligible changes can be noted because of the alike metal coverage. On the contrary, *FF* exhibits a growing tendency when both $M_{F,em}$ and $N_{C,em}$ increase, which is mainly ascribed to the reduction of series resistance losses, including either contributions due to the emitter metallization and inner carriers' transport, respectively.

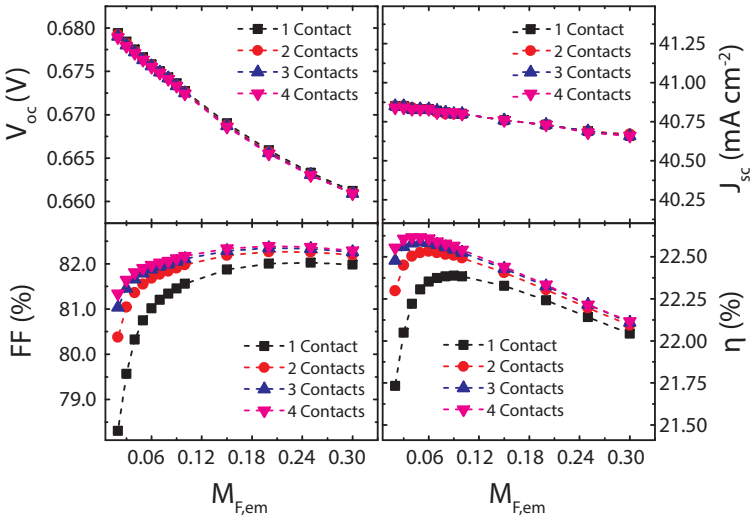

FIGURE 4.8: FOMs in function of both $M_{F,em}$ and $N_{C,em}$, with the following parameters fixed: W_{em} =300 µm, L_f =1.5 cm, t_C =2 µm, W_{BSF} = 60 µm, and $W_{C,BSF}$ = 50 µm.

To clarify further these opposite trends, Fig. 4.9 illustrates the extracted dark saturation current density (J_0) and series resistance (R_S) as a function of $M_{F,em}$ for different $N_{C,em}$. There are two competitive mechanisms as $M_{F,em}$ increases: (i) higher J_0 due to the increase of recombination losses at metal/silicon interfaces in the emitter and (ii) lower series resistance losses. The trade-off between these two mechanisms explains the optimum $M_{F,em}$ observed in the plotted curves of efficiency in Fig. 4.8, for different $N_{C,em}$. Moreover, Fig. 4.9 confirms the efficiency improvement viewed in Fig. 4.8, when placing multiple emitter contacts, is mainly related to the reduction of series resistance losses leading to a higher *FF*.

Fig. 4.10 shows that, by increasing the number of emitter contacts from 1 to 4, the observed maximum efficiency (η_{max}) increases from 22.39 % to about 22.6 % and, at the same time, the optimum $M_{F,em}$ decreases from 9.5 % to 3 %. Such a shift of the optimum $M_{F,em}$ can be explained in the following. In general, *FF* degrades when reducing the emitter metallization fraction due to the increase of series resistance losses. However, we have already demonstrated that the introduction of multiple emitter contacts allows reducing the resistive losses related to the carrier transport within the device. Therefore, when the number of emitter contacts increases, the enlargement of series resistance

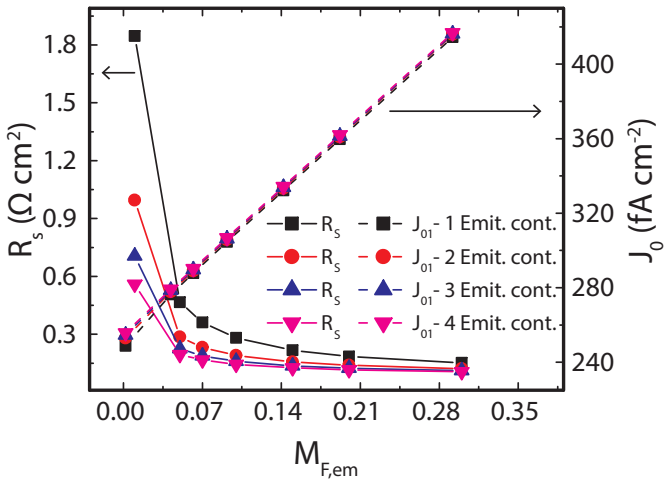

FIGURE 4.9: Series resistance (R_S) (left axis) and total dark saturation current density (J_0) (right axis) as functions of both $M_{F,em}$ and $N_{C,em}$. Each color line represent a number contacts placed on the emitter.

losses due to narrower contacts is counterbalanced by the reduction of resistive losses related to the carrier collection paths along the device. As a consequence, the *FF* degradation occurs at lower $M_{F,em}$ values when considering a higher $N_{C,em}$, as shown in Fig. 4.8. Meaning that the use of a configuration, with multiple emitter contacts, allows employing narrower contacts concerning the case of a single emitter contact's design. Overall, the observed results suggest that higher efficiency can be achieved at lower metal coverage by uniformly increasing the number of metal lines throughout the emitter region. However, technological constraints, related to the minimum allowed contact width, have to be taken into account to reach a smaller metallization fraction. Although aluminum is an inexpensive and abundant metal, the formation of such aluminum contacts can be challenging if existing contact printing methods such as very refined screen-printing cannot be used. Lennon et al., in [158], presents a detailed review of development of metal plating techniques for metallization. In addition, we can note in Fig. 4.10 that the more significant relative η increase is obtained as the number of emitter contacts passes from 1 to 2, while a further increase of $N_{C,em}$ leads to lower relative increments.

After this first investigation, of the impact of $M_{F,em}$, it has been repeated the analysis but only varying the finger length from $1.5\,\mathrm{cm}$ up to $6.5\,\mathrm{cm}$. Fig. 4.11 reports the results in terms of η_{max} and optimum $M_{F,em}$. It can see an almost linear decrease of η_{max} when increasing L_f. This is ascribed to the increase of series resistance caused by the metallization. Conversely, the optimum $M_{F,em}$ increases with L_f. Furthermore, it is worth pointing out that, for longer fingers, a higher efficiency improvement is observed when increasing $N_{C,em}$. At the same time, cell designs with more emitter contacts show a lower increment of the optimum $M_{F,em}$ when increasing L_f.

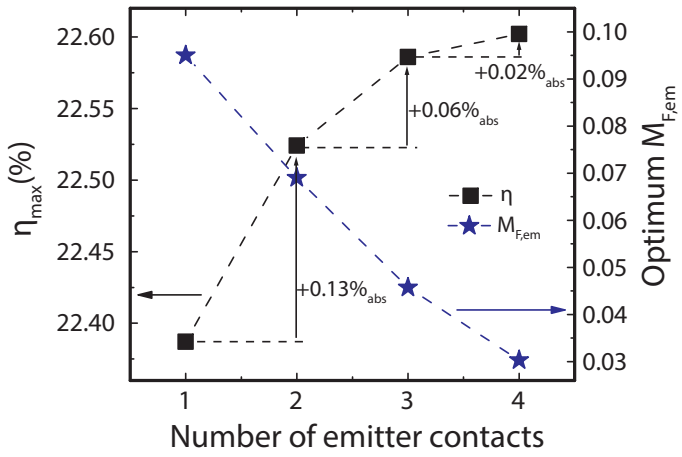

FIGURE 4.10: Maximum efficiency (η_{max}, left axis) and optimal $M_{F,em}$ (right axis) as functions of the number of emitter contacts.

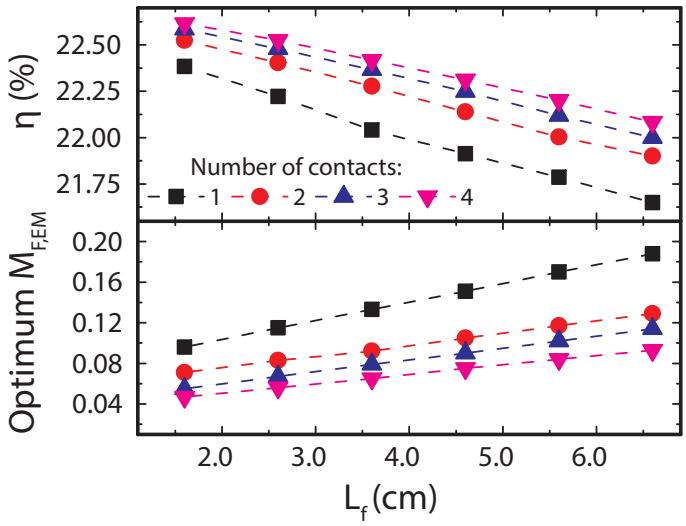

FIGURE 4.11: Maximum efficiency (η_{max}, on top) and optimal $M_{F,em}$ (on bottom) as functions of finger length (L_f). Each color line represent a different $N_{C,em}$ value.

4.2.4 Impact of the emitter metallization on the rear geometry

Continuing with the study, now investigating the impact of the emitter metallization assessing the optimal rear geometry, an extensive analysis has been performed to estimate the η_{max} and the optimum $M_{F,em}$ for distinct W_{em} and, accordingly, rear pitch. Remembering back previous analysis, the results for different W_{em}, shown in Fig. 4.12, refer to W_{BSF} = 60 µm, $W_{C,BSF}$ = 50 µm, $t_C = 2\,\mu m$ and $L_f = 1.5\,cm$. This investigation reveals a linear-like decreasing trend for the optimum $M_{F,em}$ as W_{em} increases. Such an effect results from the trade-off between the series resistance losses related to the carrier lateral

transport inside the device, which increase with W_{em}, and the recombination losses related to the electrical shading, which decrease with W_{em}. Simulation results show an optimum W_{em}, equal to $300\,\mu m$, which is the same for any $N_{C,em}$. Moreover, Fig. 4.12 shows that, when increasing the emitter width from $100\,\mu m$ to $1100\,\mu m$ and, therefore, the series resistance losses due to the carrier lateral transport, the efficiency improvement obtained as the number of emitter contacts passes from 1 to 4 increases from about $0.20\,\%$ up to $0.32\,\%$.

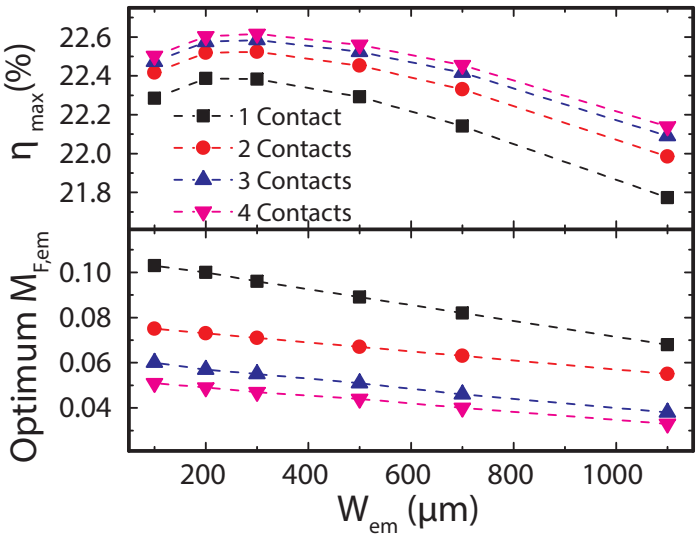

FIGURE 4.12: Maximum efficiency (η_{max}, on top) and optimal $M_{F,em}$ (on bottom) as functions of W_{em}. Each color line represent a different $N_{C,em}$ value.

Finally, to investigate solely the resistive losses' contribution due to the lateral carrier transport when increasing the rear pitch, for distinct $N_{C,em}$, a further analysis has been performed by fixing the metallization fraction of each of two regions, BSF and emitter, to the optimum values through a proportional increase of W_{em}, W_{BSF}, $W_{C,em}$ and $W_{C,BSF}$, in such a way that keeps constant the recombination losses.

As a result of this analysis, it is observable in Fig. 4.13 that a similar η value can be reached with different rear pitch size, increasing the $N_{C,em}$. As matter of fact, the maximum $\eta \approx 22.4\,\%$ obtained in the case of a single emitter contact at a rear pitch of $400\,\mu m$ is competitive when compared to $700\,\mu m$, $800\,\mu m$, $1000\,\mu m$ of rear pitch for 2-, 3- or 4- emitter contacts designs, respectively. Such an effect leads to consider the technological option of increasing the number of emitter contacts when facing pattern resolution troubles, which can force to increase the rear pitch, to avoid the degradation of the conversion efficiency. Moreover, similarly to what previously observed for the W_{em}, Fig. 4.13 also shows that, when increasing the rear pitch from $400\,\mu m$ to $1600\,\mu m$, the efficiency improvement obtained as $N_{C,em}$ passes from 1 to 4 increases from about $0.20\,\%$ up to $0.41\,\%$.

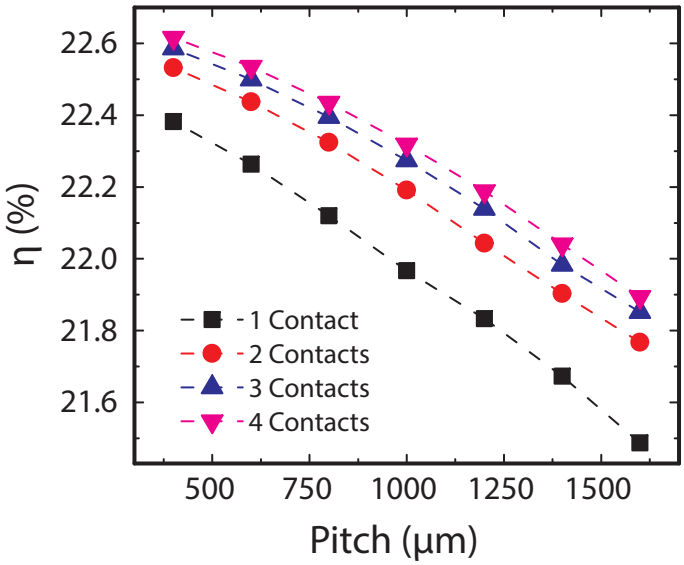

FIGURE 4.13: Efficiency as a function of the rear pitch for different $N_{C,em}$. It has been found that the optimal metallization fraction is almost constant for different rear pitch values.

In this section, it has been presented a detailed study, regarding the impact on the conversion efficiency, of IBC solar cells when using a metallization scheme featuring multiple emitter contact lines. The analysis has been performed by using a 2D electro-optical device model based on a state-of-the-art TCAD simulator. The simulation results reveal that multiple emitter contact lines have to be equidistantly distributed across the emitter region, to reduce the carrier collection path and maximize the efficiency. By the addition of metal contacts over the emitter region, η increases because of the reduction of series resistance losses. A clear optimum $M_{F,em}$ has been found for different $N_{C,em}$ as a result of the trade-off between recombination losses at metal/silicon interfaces and series resistance losses. In particular, by increasing the number of emitter contacts from 1 to 4, the maximum η increases from $22.39\,\%$ up to $22.6\,\%$, while the corresponding optimum $M_{F,em}$ decreases from $9.5\,\%$ to $3\,\%$. Moreover, it has been demonstrated that, by increasing the finger length, the η_{max} linearly decreases and, at the same time, the optimum $M_{F,em}$ increases because of the higher resistive losses. Additionally, the results reveal a linear-like decreasing trend for the optimum $M_{F,em}$ as the emitter width increases and that the value of W_{em} which maximizes the efficiency is quite independent of $N_{C,em}$. Finally, we have also observed an efficiency degradation for larger rear pitch values due to the increase of series resistance losses related to the lateral carrier transport. Nevertheless, such an effect can be relieved by increasing the $N_{C,em}$. In fact, the efficiency improvement obtained by adding multiple contacts on the emitter region increases from $0.2\,\%_{abs}$ up to about $0.4\,\%_{abs}$ for larger rear pitch. This efficiency gain is competitive considering that implementation of the proposed technological solution is feasible and suitable for industrial IBC solar cells fabrication process.

Chapter 5

Conclusions

In general, the most challenging goal within PV community, either industry or Research and development groups, is to design and manufacture devices able to reach high-efficiencies at low-cost, with most reliability as possible. The key to achieving this goal, it is to optimize and polish either the current fabrication processes and the design-models. The modeling of PV devices by means TCAD turned-out to be a powerful and helpful tool that lowers laboratory manufacturing costs and also speeds-up the optimization processes bringing guidelines of how to do it. Furthermore, TCAD modeling is now a strategic partner of PV industry, which tests concept designs before the implementation or just helps to improve the old ones.

The industry is focusing on the development of IBC devices, capable of beating the $15\,\%$ of efficiency that the actual conventional devices feature. According to the investigation presented in the eighth edition of the International technology roadmap for photovoltaic [78], IBC technology will actively increase its participation in the market in the next ten years, because of its improved efficiency that could be still improved. In this context, this Ph.D. thesis employs the electro-optical numerical simulations of IBC *c*-Si solar cells to insight their inner working.

Throughout this work, it has been shown guidelines of the numerical simulation and modeling of IBC solar cells employing Sentaurus TCAD, leaning-on the current state-of-the-art of the physical modeling, focusing mainly on metallization schemes and optimization of design parameters. For the development of this thesis, there was performed a large number of calibrated simulations, sweeping wide ranges of modeling parameters (i.e., playing with the variation of geometric dimensions, doping profiles, resistance and recombination rates) to analyze their influence over the device operation, which allowed identifying some trade-off regarding efficiency improvements. This study leads a better understanding of this kind of solar cells and helps to appraise ways to refine the structures and enhance designs of real devices.

After the introductory concepts to solar cells and how to simulate them, in Chapters 1 and 2, Chapter 3 describes in detail the numerical evaluation of the optical behavior of IBC solar cells by using Sentaurus TCAD. This chapter proposes a simplified methodology to compute $G(\zeta)$, by using the simulated photocurrent, which reduces the computational evaluation time around 10x

in devices featuring upright pyramidal front texturing but it is expandable to other kinds of isometric structures in front. The chapter continues by presenting the results of an optimization of the thicknesses of the front ARC, assuming some different qualities of SiN_x by varying its optic parameters reported in the literature and summarized in Table 3.3. The corresponding optimum thickness sizes are compiled in Table 3.4. This optimization analysis evidences the influence that the nitride has over the photogeneration of the cell. The SiN_x improves the optical properties of the solar cell but it thickness size should be carefully controlled to avoid unnecessary optical looses, especially if it has high absorption coefficient.

Chapter 3 continues with an analysis of front surface texturing shapes, comparing flat, regular pyramids, and random pyramids. When compared to an equivalent structure with a planar front surface, two pyramids forms increase the density of carrier generation in the several microns of the substrate closest to the foremost surface. This effect, illustrated in Fig. 3.16, is because of the reduction in front surface reflectance due to the multiple encounters of the ray with the absorber material (see Fig. 3.1). However, it is also due to the tendency of the texture to refract rays away from the local surface normal. A random array of pyramids causes the largest increase in G within the near-surface region. For $\zeta < 3\,\mu\text{m}$, the generation rate beneath this texture is higher than the rate beneath other morphologies. This effect is attributable to the superior transmittance of the pyramids as well as to the refraction of rays into oblique angles of traversal. At $\zeta = 3 - 5\ \mu\text{m}$, G beneath this morphology decreases steeply because, on average, for a given interval of distance throughout the ray trajectory, ζ increases by a larger amount when that interval is in the bulk region of the cell than in the area of the pyramids.

Chapter 4 presents an analysis of the electrical modeling of IBC solar cells, concerning directly two topics:

- The geometry optimization of the emitter coverage in IBC solar cells.
- Design guidelines for a metallization scheme with multiple emitter contact lines in IBC solar cells.

Regarding the optimization of the emitter coverage, the study describes the high-dependence of R_{opt} to following parameters: doping profiles and width sizes of both emitter and BSF, pitch, and bulk resistivity, in a range from 0.6 to 0.95. From the geometry design perspective, it is more efficient optimizing each width size (BSF and emitter) independently than optimizing R at fixed pitch or BSF width. In the case of a bulk resistivity of $1\,\Omega\,\text{cm}$ ($10\,\Omega\,\text{cm}$), the obtained absolute maximum efficiency is $23.08\,\%$ ($22.96\,\%$) for BSF width of $55\,\mu\text{m}$ ($100\,\mu\text{m}$) and emitter width of $646\,\mu\text{m}$ ($448\,\mu\text{m}$), which give a pitch of $706\,\mu\text{m}$ ($553\,\mu\text{m}$) and R_{opt} of 0.91 (0.81). The represented results in this section are comparable with the experimental values $22.1\,\%$ in [159] and the $22.45\,\%$ presented in [160]. Furthermore, in Table 5.1 is presented a comparison between experimental data from [159] and the same cell simulated in TCAD, showing a good match between both.

	V_{OC} (mV)	J_{SC} (mA cm^{-2})	FF (%)	η (%)
Experimental	681.0	40.9	0.81	22.6
Simulated	679.0	40.5	0.81	22.3

TABLE 5.1: Performance comparison between TCAD simulations and experimental data (from [159]).

Respecting the study for the metallization scheme with multiple emitter contact lines, the analysis reveals that multiple emitter contacts, preferably equidistantly distributed, reduce the carrier collection path improving the efficiency. This improvement is because increasing more contacts decreases the inner series resistance of the device, but, on the other hand, the resistance of Al/Si increases. A clear optimum $M_{F,em}$ has been found for different $N_{C,em}$ as a result of the trade-off between recombination losses at metal/silicon interfaces and series resistance losses. In particular, by increasing the number of emitter contacts from 1 to 4, the maximum η increases from $22.39\,\%$ up to $22.6\,\%$, while the corresponding optimum $M_{F,em}$ decreases from $9.5\,\%$ to $3\,\%$. Furthermore, it has been demonstrated that, by increasing the finger length, the η_{max} linearly decreases and, at the same time, the optimum $M_{F,em}$ increases because of the higher resistive losses. The results reveal a linear-like decreasing trend for the optimum $M_{F,em}$ as the emitter width increases and that the value of W_{em} which maximizes the efficiency is quite independent of the $N_{C,em}$. Lastly, the observed efficiency degradation, for larger rear pitch values due to the increase of series resistance losses, is related to the lateral carrier transport. Nevertheless, such an effect can be relieved by increasing $N_{C,em}$. In fact, the efficiency improvement obtained by adding multiple contacts on the emitter region increases from $0.2\,\%_{abs}$ up to about $0.4\,\%_{abs}$ for larger rear pitch. This efficiency gain is competitive considering that implementation of the proposed technological solution is feasible and suitable for industrial IBC solar cells fabrication process.

Bibliography

[1] R Lindsey, "Under a variable sun", *NASA's Earth Observatory. Accessed June*, vol. 20, p. 2010, 2003.

[2] G. Otmar, *Light sensitive device*, US Patent 2,259,372, Oct. 1941.

[3] D. M. Chapin, C. S. Fuller, and G. L. Pearson, "A New Silicon p-n Junction Photocell for Converting Solar Radiation into Electrical Power", *Journal of Applied Physics*, vol. 25, no. 5, p. 676, 1954, ISSN: 00218979.

[4] R. Schwartz and M. Lammert, "Silicon solar cells for high concentration applications", in *Electron Devices Meeting, 1975 International*, IEEE, vol. 21, 1975, pp. 350–352.

[5] J. Zhao, A. Wang, and M. A. Green, "24· 5% efficiency silicon pert cells on mcz substrates and 24· 7% efficiency perl cells on fz substrates", *Progress in Photovoltaics: Research and Applications*, vol. 7, no. 6, pp. 471–474, 1999.

[6] M. A. Green, "The path to 25% silicon solar cell efficiency: History of silicon cell evolution", *Progress in Photovoltaics: Research and Applications*, vol. 17, no. 3, pp. 183–189, 2009.

[7] K. Masuko, M. Shigematsu, T. Hashiguchi, D. Fujishima, M. Kai, N. Yoshimura, T. Yamaguchi, Y. Ichihashi, T. Mishima, N. Matsubara, *et al.*, "Achievement of more than 25% conversion efficiency with crystalline silicon heterojunction solar cell", *IEEE Journal of Photovoltaics*, vol. 4, no. 6, pp. 1433–1435, 2014.

[8] D. D. Smith, P. Cousins, S. Westerberg, R. De Jesus-Tabajonda, G. Aniero, and Y.-C. Shen, "Toward the practical limits of silicon solar cells", *IEEE Journal of Photovoltaics*, vol. 6, no. 4, pp. 1465–1469, 2014.

[9] K. Yoshikawa, H. Kawasaki, W. Yoshida, T. Irie, K. Konishi, K. Nakano, T. Uto, D. Adachi, M. Kanematsu, H. Uzu, and K. Yamamoto, "Silicon heterojunction solar cell with interdigitated back contacts for a photoconversion efficiency over 26%", *Nature Energy*, vol. 2, p. 17 032, Mar. 2017, ISSN: 2058-7546.

[10] A. Richter, M. Hermle, and S. W. Glunz, "Reassessment of the limiting efficiency for crystalline silicon solar cells", *IEEE journal of photovoltaics*, vol. 3, no. 4, pp. 1184–1191, 2013.

[11] M. A. Green, K. Emery, Y. Hishikawa, W. Warta, and E. D. Dunlop, "Solar cell efficiency tables (version 45)", *Progress in photovoltaics: Research and applications*, vol. 23, no. 1, pp. 1–9, 2015.

[12] D. Adachi, J. L. Hernández, and K. Yamamoto, "Impact of carrier recombination on fill factor for large area heterojunction crystalline silicon solar cell with 25.1% efficiency", *Applied Physics Letters*, vol. 107, no. 23, p. 233 506, 2015.

[13] F Feldmann, M Simon, M Bivour, C Reichel, M Hermle, and S. Glunz, "Carrier-selective contacts for si solar cells", *Applied Physics Letters*, vol. 104, no. 18, p. 181 105, 2014.

[14] S. Glunz, F Feldmann, A Richter, M Bivour, C Reichel, H Steinkemper, J Benick, and M Hermle, "The irresistible charm of a simple current flow pattern—25% with a solar cell featuring a full-area back contact", in *Proceedings of the 31st European Photovoltaic Solar Energy Conference and Exhibition*, 2015, pp. 259–263.

[15] M. A. Green, K. Emery, Y. Hishikawa, W. Warta, and E. D. Dunlop, "Solar cell efficiency tables (version 47)", *Progress in Photovoltaics: Research and Applications*, vol. 24, no. NREL/JA-5J00-65643, 2016.

[16] M. Taguchi, A. Yano, S. Tohoda, K. Matsuyama, Y. Nakamura, T. Nishiwaki, K. Fujita, and E. Maruyama, "24.7% record efficiency hit solar cell on thin silicon wafer", *IEEE Journal of Photovoltaics*, vol. 4, no. 1, pp. 96–99, 2014.

[17] J. Geissbühler, J. Werner, S. M. De Nicolas, L. Barraud, A. Hessler-Wyser, M. Despeisse, S. Nicolay, A. Tomasi, B. Niesen, S. De Wolf, *et al.*, "22.5% efficient silicon heterojunction solar cell with molybdenum oxide hole collector", *Applied Physics Letters*, vol. 107, no. 8, p. 081 601, 2015.

[18] L. Tous, M. Aleman, R. Russell, E. Cornagliotti, P. Choulat, A Uruena, S. Singh, J. John, F. Duerinckx, J. Poortmans, *et al.*, "Evaluation of advanced p-perl and n-pert large area silicon solar cells with 20.5% energy conversion efficiencies", *Progress in Photovoltaics: Research and Applications*, vol. 23, no. 5, pp. 660–670, 2015.

[19] M. R. Payo, F Duerinckx, Y Li, and E Cornagliotti, "Advanced Doping Profiles By Selective Epitaxy Energy Pert Cells in N-Type", in *31st European Photovoltaic Solar Energy Conference and Exhibition*, WIP, 2015, pp. 433–439.

[20] W. Shockley and H. J. Queisser, "Detailed balance limit of efficiency of p-n junction solar cells", *Journal of applied physics*, vol. 32, no. 3, pp. 510–519, 1961.

[21] R. M. Swanson, "Approaching the 29% limit efficiency of silicon solar cells", in *Conference Record of the Thirty-first IEEE Photovoltaic Specialists Conference, 2005.*, IEEE, 2005, pp. 889–894.

[22] G. T. Reed and A. P. Knights, *Silicon photonics: An introduction*. John Wiley & Sons, 2004.

[23] A. Richter, S. W. Glunz, F. Werner, J. Schmidt, and A. Cuevas, "Improved quantitative description of auger recombination in crystalline silicon", *Physical Review B*, vol. 86, no. 16, p. 165 202, 2012.

[24] M. A. Green, "Lambertian light trapping in textured solar cells and light-emitting diodes: Analytical solutions", *Progress in Photovoltaics: Research and Applications*, vol. 10, no. 4, pp. 235–241, 2002.

[25] A. Ingenito, G. Limodio, P. Procel, G. Yang, H. Dijkslag, O. Isabella, and M. Zeman, "Silicon solar cell architecture with front selective and rear full area ion-implanted passivating contacts", *Solar RRL*, vol. 1, no. 7, 2017.

[26] R Hezel and K Jaeger, "Low-temperature surface passivation of silicon for solar cells", *Journal of the Electrochemical Society*, vol. 136, no. 2, pp. 518–523, 1989.

[27] A. G. Aberle, "Surface passivation of crystalline silicon solar cells: A review", *Progress in Photovoltaics: Research and Applications*, vol. 8, no. 5, pp. 473–487, 2000.

[28] B. Richards, "Comparison of tio2 and other dielectric coatings for buried-contact solar cells: A review", *Progress in Photovoltaics: Research and Applications*, vol. 12, no. 4, pp. 253–281, 2004.

[29] E Yablonovitch, D. Allara, C. Chang, T Gmitter, and T. Bright, "Unusually low surface-recombination velocity on silicon and germanium surfaces", *Physical review letters*, vol. 57, no. 2, p. 249, 1986.

[30] D. Fenner, D. Biegelsen, and R. Bringans, "Silicon surface passivation by hydrogen termination: A comparative study of preparation methods", *Journal of Applied Physics*, vol. 66, no. 1, pp. 419–424, 1989.

[31] G. W. Trucks, K. Raghavachari, G. S. Higashi, and Y. J. Chabal, "Mechanism of hf etching of silicon surfaces: A theoretical understanding of hydrogen passivation", *Phys. Rev. Lett.*, vol. 65, pp. 504–507, 4 Jul. 1990.

[32] J. J. Boland, "Scanning tunnelling microscopy of the interaction of hydrogen with silicon surfaces", *Advances in physics*, vol. 42, no. 2, pp. 129–171, 1993.

[33] S. Glunz, D Biro, S Rein, and W Warta, "Field-effect passivation of the sio2si interface", *Journal of Applied Physics*, vol. 86, no. 1, pp. 683–691, 1999.

[34] B Hoex, J. Gielis, M. Van de Sanden, and W. Kessels, "On the c-si surface passivation mechanism by the negative-charge-dielectric al2o3", *Journal of Applied Physics*, vol. 104, no. 11, p. 113 703, 2008.

[35] W. D. Eades and R. M. Swanson, "Calculation of surface generation and recombination velocities at the si-sio2 interface", *Journal of applied Physics*, vol. 58, no. 11, pp. 4267–4276, 1985.

[36] E Yablonovitch, R. Swanson, W. Eades, and B. Weinberger, "Electron-hole recombination at the si-sio2 interface", *Applied Physics Letters*, vol. 48, no. 3, pp. 245–247, 1986.

[37] A. G. Aberle, S. Glunz, and W. Warta, "Impact of illumination level and oxide parameters on shockley–read–hall recombination at the si-sio2 interface", *Journal of Applied Physics*, vol. 71, no. 9, pp. 4422–4431, 1992.

[38] K Yasutake, Z Chen, S. Pang, and A Rohatgi, "Modeling and characterization of interface state parameters and surface recombination velocity at plasma enhanced chemical vapor deposited sio2–si interface", *Journal of applied physics*, vol. 75, no. 4, pp. 2048–2054, 1994.

[39] O Schultz, S. Glunz, and G. Willeke, "Short communication: Accelerated publication: Multicrystalline silicon solar cells exceeding 20% efficiency", *Progress in Photovoltaics: Research and Applications*, vol. 12, no. 7, pp. 553–558, 2004.

[40] T. Lauinger, J. Schmidt, A. G. Aberle, and R. Hezel, "Record low surface recombination velocities on 1 Ω cm p-silicon using remote plasma silicon nitride passivation", *Applied Physics Letters*, vol. 68, no. 9, pp. 1232–1234, 1996.

[41] M. Kerr, J Schmidt, A Cuevas, and J. Bultman, "Surface recombination velocity of phosphorus-diffused silicon solar cell emitters passivated with plasma enhanced chemical vapor deposited silicon nitride and thermal silicon oxide", *Journal of Applied Physics*, vol. 89, no. 7, pp. 3821–3826, 2001.

[42] H Mackel and R Ludemann, "Detailed study of the composition of hydrogenated sinx layers for high-quality silicon surface passivation", *Journal of Applied Physics*, vol. 92, no. 5, pp. 2602–2609, 2002.

[43] A. G. Aberle, "Overview on sin surface passivation of crystalline silicon solar cells", *Solar Energy Materials and Solar Cells*, vol. 65, no. 1, pp. 239–248, 2001.

[44] I Martin, M Vetter, A Orpella, J Puigdollers, A Cuevas, and R Alcubilla, "Surface passivation of p-type crystalline si by plasma enhanced chemical vapor deposited amorphous sicx: H films", *Applied Physics Letters*, vol. 79, no. 14, pp. 2199–2201, 2001.

[45] S Janz, S Riepe, M Hofmann, S Reber, and S Glunz, "Phosphorus-doped sic as an excellent p-type si surface passivation layer", *Applied Physics Letters*, vol. 88, no. 13, 2006.

[46] G Agostinelli, A Delabie, P Vitanov, Z Alexieva, H. Dekkers, S De Wolf, and G Beaucarne, "Very low surface recombination velocities on p-type silicon wafers passivated with a dielectric with fixed negative charge", *Solar Energy Materials and Solar Cells*, vol. 90, no. 18, pp. 3438–3443, 2006.

[47] B. Hoex, J. Schmidt, P Pohl, M. Van de Sanden, and W. Kessels, "Silicon surface passivation by atomic layer deposited al2o3", *Journal of Applied Physics*, vol. 104, no. 4, p. 044 903, 2008.

[48] G. Dingemans and W. Kessels, "Status and prospects of al2o3-based surface passivation schemes for silicon solar cells", *Journal of Vacuum Science & Technology A*, vol. 30, no. 4, p. 040 802, 2012.

[49] J. Pankove and M. Tarng, "Amorphous silicon as a passivant for crystalline silicon", *Applied Physics Letters*, vol. 34, no. 2, pp. 156–157, 1979.

[50] S. Olibet, E. Vallat-Sauvain, and C. Ballif, "Model for a-si: H/c-si interface recombination based on the amphoteric nature of silicon dangling bonds", *Physical Review B*, vol. 76, no. 3, p. 035 326, 2007.

[51] M. Z. Rahman and S. I. Khan, "Advances in surface passivation of c-si solar cells", *Materials for Renewable and Sustainable Energy*, vol. 1, no. 1, p. 1, 2012, ISSN: 2194-1467.

[52] M. Tanaka, M. Taguchi, T. Matsuyama, T. Sawada, S. Tsuda, S. Nakano, H. Hanafusa, and Y. Kuwano, "Development of new a-si/c-si heterojunction solar cells: Acj-hit (artificially constructed junction-heterojunction with intrinsic thin-layer)", *Japanese Journal of Applied Physics*, vol. 31, no. 11R, p. 3518, 1992.

[53] M. Taguchi, K. Kawamoto, S. Tsuge, T. Baba, H. Sakata, M. Morizane, K. Uchihashi, N. Nakamura, S. Kiyama, and O. Oota, "Hittm cells—high-efficiency crystalline si cells with novel structure", *Progress in Photovoltaics: Research and Applications*, vol. 8, no. 5, pp. 503–513, 2000, ISSN: 1099-159X.

[54] S. De Wolf, A. Descoeudres, Z. C. Holman, and C. Ballif, "High-efficiency silicon heterojunction solar cells: A review", *Green*, vol. 2, no. 1, pp. 7–24, 2012.

[55] K. Misiakos and D. Tsamakis, "Accurate measurements of the silicon intrinsic carrier density from 78 to 340 k", *Journal of applied physics*, vol. 74, no. 5, pp. 3293–3297, 1993.

[56] P. P. Altermatt, A. Schenk, F. Geelhaar, and G. Heiser, "Reassessment of the intrinsic carrier density in crystalline silicon in view of band-gap narrowing", *Journal of Applied Physics*, vol. 93, no. 3, pp. 1598–1604, 2003.

[57] P. Würfel and U. Würfel, *Physics of solar cells: From basic principles to advanced concepts*. John Wiley & Sons, 2009.

[58] A. H. Smets, K. Jäger, O. Isabella, R. A. van Swaaij, and M. Zeman, *Solar energy: The physics and engineering of photovoltaic conversion, technologies and systems*. UIT Cambridge Limited, 2016.

[59] O. D. Miller, E. Yablonovitch, and S. R. Kurtz, "Strong internal and external luminescence as solar cells approach the shockley–queisser limit", *IEEE Journal of Photovoltaics*, vol. 2, no. 3, pp. 303–311, 2012.

[60] M. A. Green, J. Zhao, A. Wang, P. J. Reece, and M. Gal, "Efficient silicon light-emitting diodes", *Nature*, vol. 412, no. 6849, pp. 805–808, 2001.

[61] T Trupke, M. A. Green, P Würfel, P. Altermatt, A Wang, J Zhao, and R Corkish, "Temperature dependence of the radiative recombination coefficient of intrinsic crystalline silicon", *Journal of Applied Physics*, vol. 94, no. 8, pp. 4930–4937, 2003.

[62] P. K. Nayak, G. Garcia-Belmonte, A. Kahn, J. Bisquert, and D. Cahen, "Photovoltaic efficiency limits and material disorder", *Energy & Environmental Science*, vol. 5, no. 3, pp. 6022–6039, 2012.

[63] P. P. Altermatt, J. Schmidt, G. Heiser, and A. G. Aberle, "Assessment and parameterisation of coulomb-enhanced auger recombination coefficients in lowly injected crystalline silicon", *Journal of Applied Physics*, vol. 82, no. 10, pp. 4938–4944, 1997.

[64] W. Shockley and W. Read Jr, "Statistics of the recombinations of holes and electrons", *Physical review*, vol. 87, no. 5, p. 835, 1952.

[65] R. N. Hall, "Electron-hole recombination in germanium", *Phys. Rev.*, vol. 87, pp. 387–387, 2 Jul. 1952.

[66] A. Cuevas, "The recombination parameter j 0", *Energy Procedia*, vol. 55, pp. 53–62, 2014.

[67] D. Kane and R. Swanson, "Measurement of the emitter saturation current by a contactless photoconductivity decay method", in *IEEE photovoltaic specialists conference. 18*, 1985, pp. 578–583.

[68] M. A. Green, K. Emery, Y. Hishikawa, W. Warta, E. D. Dunlop, D. H. Levi, and A. W. Ho-Baillie, "Solar cell efficiency tables (version 49)", *Progress in photovoltaics: Research and applications*, vol. 25, no. 1, pp. 3–13, 2017.

[69] I. Mora-Seró, G. Garcia-Belmonte, P. P. Boix, M. A. Vázquez, and J. Bisquert, "Impedance spectroscopy characterisation of highly efficient silicon solar cells under different light illumination intensities", *Energy & Environmental Science*, vol. 2, no. 6, pp. 678–686, 2009.

[70] D. Pysch, A. Mette, and S. W. Glunz, "A review and comparison of different methods to determine the series resistance of solar cells", *Solar Energy Materials and Solar Cells*, vol. 91, no. 18, pp. 1698–1706, 2007.

[71] J Zhao, A Wang, P Altermatt, and M. Green, "Twenty-four percent efficient silicon solar cells with double layer antireflection coatings and reduced resistance loss", *Applied Physics Letters*, vol. 66, no. 26, pp. 3636–3638, 1995.

[72] H. J. Snaith, "The perils of solar cell efficiency measurements", *Nature Photonics*, vol. 6, no. 6, pp. 337–340, 2012.

[73] J Mandelkorn, C McAfee, J Kesperis, L Schwartz, and W Pharo, "Fabrication and characteristics of phosphorous-diffused silicon solar cells", *Journal of the Electrochemical Society*, vol. 109, no. 4, pp. 313–318, 1962.

[74] H Flicker, J. Loferski, and J Scott-Monck, "Radiation defect introduction rates in n-and p-type silicon in the vicinity of the radiation damage threshold", *Physical Review*, vol. 128, no. 6, p. 2557, 1962.

[75] X. Gao, S.-s. Yang, and Z.-z. Feng, "Radiation effects of space solar cells", in *High-Efficiency Solar Cells: Physics, Materials, and Devices*, X. Wang and Z. M. Wang, Eds. Cham: Springer International Publishing, 2014, pp. 597–622, ISBN: 978-3-319-01988-8.

[76] A. Ebong, Y.-H. Wu, L.-L. Chen, J.-R. Wu, *et al.*, "Record high efficiency of screen-printed silicon aluminum back surface field solar cell: 20.29%", *Jpn. J. Appl. Phys*, vol. 56, 08MB25, 2017.

[77] Z. Wang, P. Han, H. Lu, H. Qian, L. Chen, Q. Meng, N. Tang, F. Gao, Y. Jiang, J. Wu, *et al.*, "Advanced perc and perl production cells with 20.3% record efficiency for standard commercial p-type silicon wafers", *Progress in Photovoltaics: Research and Applications*, vol. 20, no. 3, pp. 260–268, 2012.

[78] S. P. Group *et al.*, *International technology roadmap for photovoltaic*, 2016.

[79] A. Khanna, Z. P. Ling, V. Shanmugam, M. B. Boreland, I. Hayashi, D. Kirk, H. Akimoto, A. G. Aberle, and T. Mueller, "Screen printed metallisation for silicon heterojunction solar cells", in *Proc. 28th Eur. Photovoltaic Solar Energy Conf. Exhib*, 2013, pp. 1336–1339.

[80] M. Bivour, S. Schröer, and M. Hermle, "Numerical analysis of electrical tco/a-si: H (p) contact properties for silicon heterojunction solar cells", *Energy Procedia*, vol. 38, pp. 658–669, 2013.

[81] T. P. S. Srinivasan and D. Rajamani, "Solar power renaissance", *International Journal of Supply Chain Management*, vol. 5, no. 1, pp. 63–67, 2016.

[82] P. J. Cousins, D. D. Smith, H.-C. Luan, J. Manning, T. D. Dennis, A. Waldhauer, K. E. Wilson, G. Harley, and W. P. Mulligan, "Generation 3: Improved performance at lower cost", in *Photovoltaic Specialists Conference (PVSC), 2010 35th IEEE*, IEEE, 2010, pp. 000 275–000 278.

[83] O Nichiporuk, A Kaminski, M Lemiti, A Fave, and V Skryshevsky, "Optimisation of interdigitated back contacts solar cells by two-dimensional numerical simulation", *Solar energy materials and solar cells*, vol. 86, no. 4, pp. 517–526, 2005.

[84] A. Fell, K. C. Fong, K. R. McIntosh, E. Franklin, and A. W. Blakers, "3-d simulation of interdigitated-back-contact silicon solar cells with quokka including perimeter losses", *IEEE Journal of Photovoltaics*, vol. 4, no. 4, pp. 1040–1045, 2014.

[85] P. Procel, V. Maccaronio, F. Crupi, G. Cocorullo, M. Zanuccoli, P. Magnone, and C. Fiegna, "Analysis of the impact of doping levels on performance of back contact-back junction solar cells", *Energy Procedia*, vol. 55, pp. 128–132, 2014.

[86] P Procel, M Zanuccoli, V Maccaronio, F Crupi, G Cocorullo, P Magnone, and C Fiegna, "Numerical simulation of the impact of design parameters on the performance of back-contact back-junction solar cell", *Journal of Computational Electronics*, vol. 15, no. 1, pp. 260–268, 2016.

[87] R Swanson, "The silicon photovoltaic roadmap", in *Stanford Energy Seminar Nov*, vol. 14, 2011, p. 2011.

[88] C Reichel, F Granek, M Hermle, and S. Glunz, "Investigation of electrical shading effects in back-contacted back-junction silicon solar cells using the two-dimensional charge collection probability and the reciprocity theorem", *Journal of Applied Physics*, vol. 109, no. 2, p. 024 507, 2011.

[89] M. Zanuccoli, R. De Rose, P. Magnone, E. Sangiorgi, and C. Fiegna, "Performance analysis of rear point contact solar cells by three-dimensional numerical simulation", *IEEE Transactions on Electron Devices*, vol. 59, no. 5, pp. 1311–1319, 2012.

[90] P. Magnone, D. Tonini, R. De Rose, M. Frei, F. Crupi, E. Sangiorgi, and C. Fiegna, "Numerical simulation and modeling of resistive and recombination losses in mwt solar cells", *IEEE Journal of Photovoltaics*, vol. 3, no. 4, pp. 1215–1221, 2013.

[91] R. M. Swanson, S. K. Beckwith, R. A. Crane, W. D. Eades, Y. H. Kwark, R. Sinton, and S. Swirhun, "Point-contact silicon solar cells", *IEEE Transactions on Electron Devices*, vol. 31, no. 5, pp. 661–664, 1984.

[92] C Zechner, P Fath, G Willeke, and E Bucher, "Two-and three-dimensional optical carrier generation determination in crystalline silicon solar cells", *Solar energy materials and solar cells*, vol. 51, no. 3, pp. 255–267, 1998.

[93] R Bisconti and H. Ossenbrink, "Optical modelling of silicon cells in spherical shape", *Solar energy materials and solar cells*, vol. 48, no. 1, pp. 1–6, 1997.

[94] J. Wong, "Griddler: Intelligent computer aided design of complex solar cell metallization patterns", in *Photovoltaic Specialists Conference (PVSC), 2013 IEEE 39th*, IEEE, 2013, pp. 0933–0938.

[95] *Synopsys, Sentaurus Device User Guide. Version I-2014*, Mountain View, CA, 2014.

[96] S. Kluska, F. Granek, M. Rüdiger, M. Hermle, and S. W. Glunz, "Modeling and optimization study of industrial n-type high-efficiency back-contact back-junction silicon solar cells", *Solar Energy Materials and Solar Cells*, vol. 94, no. 3, pp. 568–577, 2010.

[97] F. Granek, M. Hermle, D. M. Huljić, O. Schultz-Wittmann, and S. W. Glunz, "Enhanced lateral current transport via the front n+ diffused layer of n-type high-efficiency back-junction back-contact silicon solar cells", *Progress in photovoltaics: Research and applications*, vol. 17, no. 1, pp. 47–56, 2009.

[98] P. P. Altermatt and G. Heiser, "Development of a three-dimensional numerical model of grain boundaries in highly doped polycrystalline silicon and applications to solar cells", *Journal of applied physics*, vol. 91, no. 7, pp. 4271–4274, 2002.

[99] R. E. Bank, D. J. Rose, and W. Fichtner, "Numerical methods for semiconductor device simulation", *SIAM Journal on Scientific and Statistical Computing*, vol. 4, no. 3, pp. 416–435, 1983.

[100] S Muller, K. Kells, and W. Fichtner, "Automatic rectangle-based adaptive mesh generation without obtuse angles", *IEEE transactions on computer-aided design of integrated circuits and systems*, vol. 11, no. 7, pp. 855–863, 1992.

[101] G. Heiser, C. Pommerell, J. Weis, and W. Fichtner, "Three-dimensional numerical semiconductor device simulation: Algorithms, architectures, results", *IEEE transactions on computer-aided design of integrated circuits and systems*, vol. 10, no. 10, pp. 1218–1230, 1991.

[102] M. A. Green, "The passivated emitter and rear cell (perc): From conception to mass production", *Solar Energy Materials and Solar Cells*, vol. 143, pp. 190–197, 2015.

[103] M Taguchi, M Tanaka, T Matsuyama, T Matsuoka, S Tsuda, S Nakano, Y Kishi, and Y Kuwano, "Improvement of the conversion efficiency of polycrystalline silicon thin film solar cell", in *Proc. Fifth PVSEC*, 1990, pp. 689–692.

[104] A. Fell, K. R. McIntosh, P. P. Altermatt, G. J. M. Janssen, R. Stangl, A. Ho-Baillie, H. Steinkemper, J. Greulich, M. Müller, B. Min, K. C. Fong, M. Hermle, I. G. Romijn, and M. D. Abbott, "Input parameters for the simulation of silicon solar cells in 2014", *IEEE Journal of Photovoltaics*, vol. 5, no. 4, pp. 1250–1263, Jul. 2015, ISSN: 2156-3381.

[105] P. Magnone, M. Debucquoy, D. Giaffreda, N. Posthuma, and C. Fiegna, "Understanding the influence of busbars in large-area ibc solar cells

by distributed spice simulations", *IEEE Journal of Photovoltaics*, vol. 5, no. 2, pp. 552–558, 2015.

[106] A. Schenk, "Finite-temperature full random-phase approximation model of band gap narrowing for silicon device simulation", *Journal of Applied Physics*, vol. 84, no. 7, pp. 3684–3695, 1998, ISSN: 00218979.

[107] D. Klaassen, "A unified mobility model for device simulation—I. Model equations and concentration dependence", *Solid-State Electronics*, vol. 35, no. 7, pp. 953–959, Jul. 1992, ISSN: 00381101.

[108] J. Fossum, R. Mertens, D. Lee, and J. Nijs, "Carrier recombination and lifetime in highly doped silicon", *Solid-State Electronics*, vol. 26, no. 6, pp. 569 –576, 1983, ISSN: 0038-1101.

[109] P. P. Altermatt, J. O. Schumacher, A. Cuevas, M. J. Kerr, S. W. Glunz, R. R. King, G. Heiser, and A. Schenk, "Numerical modeling of highly doped si: P emitters based on fermi–dirac statistics and self-consistent material parameters", *Journal of Applied Physics*, vol. 92, no. 6, pp. 3187–3197, 2002.

[110] P. P. Altermatt, H Plagwitz, R Bock, J. Schmidt, R Brendel, M. J. Kerr, A. Cuevas, *et al.*, "The surface recombination velocity at boron-doped emitters: Comparison between various passivation techniques", in *Proceedings of the 21st European Photovoltaic Solar Energy Conference*, WIP Renewable Energies Dresden, Germany, 2006, pp. 647–650.

[111] E. Franklin, K. Fong, K. McIntosh, A. Fell, A. Blakers, T. Kho, D. Walter, D. Wang, N. Zin, M. Stocks, *et al.*, "Design, fabrication and characterisation of a 24.4% efficient interdigitated back contact solar cell", *Progress in Photovoltaics: Research and applications*, vol. 24, no. 4, pp. 411–427, 2016.

[112] P. D. Desai, H. James, and C. Y. Ho, "Electrical resistivity of aluminum and manganese", *Journal of physical and chemical reference data*, vol. 13, no. 4, pp. 1131–1172, 1984.

[113] I. E. Commission *et al.*, "Photovoltaic devices—part 3: Measurement principles for terrestrial photovoltaic (pv) solar devices with reference spectral irradiance data", *IEC 60904–3 ed2*, 2008.

[114] S. Glunz, S Sterk, R Steeman, W Warta, J Knobloch, and W Wettling, "Emitter dark saturation currents of high-efficiency solar cells with inverted pyramids", in *Proceedings of the 13th European Photovoltaic Solar Energy Conference*, 1995, pp. 409–12.

[115] H.-C. Yuan, V. E. Yost, M. R. Page, P. Stradins, D. L. Meier, and H. M. Branz, "Efficient black silicon solar cell with a density-graded nanoporous surface: Optical properties, performance limitations, and design rules", *Applied Physics Letters*, vol. 95, no. 12, p. 123 501, 2009.

[116] X. Liu, P. R. Coxon, M. Peters, B. Hoex, J. M. Cole, and D. J. Fray, "Black silicon: Fabrication methods, properties and solar energy applications", *Energy & Environmental Science*, vol. 7, no. 10, pp. 3223–3263, 2014.

[117] M. Otto, M. Algasinger, H. Branz, B. Gesemann, T. Gimpel, K. Füchsel, T. Käsebier, S. Kontermann, S. Koynov, X. Li, *et al.*, "Black silicon

photovoltaics", *Advanced optical materials*, vol. 3, no. 2, pp. 147–164, 2015.

[118] H. Savin, P. Repo, G. Von Gastrow, P. Ortega, E. Calle, M. Garín, and R. Alcubilla, "Black silicon solar cells with interdigitated back-contacts achieve 22.1% efficiency", *Nature nanotechnology*, vol. 10, no. 7, pp. 624–628, 2015.

[119] A. Ingenito, O. Isabella, and M. Zeman, "Nano-cones on micro-pyramids: Modulated surface textures for maximal spectral response and high-efficiency solar cells", *Progress in Photovoltaics: Research and Applications*, vol. 23, no. 11, pp. 1649–1659, 2015.

[120] W. P. Mulligan, D. H. Rose, M. J. Cudzinovic, D. M. De Ceuster, K. R. McIntosh, D. D. Smith, and R. M. Swanson, "Manufacture of solar cells with 21% efficiency", *Proc. 19th EPVSEC*, vol. 387, 2004.

[121] M. Hendrichs, M. Padilla, J. Walter, F. Clement, and B. Rech, "Screen-printed metallization concepts for large-area back-contact back-junction silicon solar cells", *IEEE Journal of Photovoltaics*, vol. 6, no. 1, pp. 374–383, 2016.

[122] Z. C. Holman, S. De Wolf, and C. Ballif, "Improving metal reflectors by suppressing surface plasmon polaritons: A priori calculation of the internal reflectance of a solar cell", *Light: Science & Applications*, vol. 2, no. 10, e106, 2013.

[123] R. M. Swanson, *Back side contact solar cell with doped polysilicon regions*, US Patent 7,468,485, Dec. 2008.

[124] D. L. Meier and D. K. Schroder, "Contact resistance: Its measurement and relative importance to power loss in a solar cell", *IEEE transactions on electron devices*, vol. 31, no. 5, pp. 647–653, 1984.

[125] D. K. Schroder and D. L. Meier, "Solar cell contact resistance—a review", *IEEE Transactions on electron devices*, vol. 31, no. 5, pp. 637–647, 1984.

[126] P. P. Altermatt, "Models for numerical device simulations of crystalline silicon solar cells—a review", *Journal of computational electronics*, vol. 10, no. 3, p. 314, 2011.

[127] S. C. Baker-Finch and K. R. McIntosh, "One-dimensional photogeneration profiles in silicon solar cells with pyramidal texture", *Progress in Photovoltaics: Research and Applications*, vol. 20, no. 1, pp. 51–61, 2012.

[128] E. Yablonovitch, "Statistical ray optics", *JOSA*, vol. 72, no. 7, pp. 899–907, 1982.

[129] P. Campbell and M. A. Green, "Light trapping properties of pyramidally textured surfaces", *Journal of Applied Physics*, vol. 62, no. 1, pp. 243–249, 1987.

[130] P Campbell, "Light trapping in textured solar cells", *Solar energy materials*, vol. 21, no. 2-3, pp. 165–172, 1990.

[131] P. Campbell, "Enhancement of light absorption from randomizing and geometric textures", *J. Opt. Soc. Am. B*, vol. 10, no. 12, pp. 2410–2415, Dec. 1993.

[132] V. Moroz, J. Huang, K. Wijekoon, and D. Tanner, "Experimental and theoretical analysis of the optical behavior of textured silicon wafers",

in *2011 37th IEEE Photovoltaic Specialists Conference*, IEEE, Jun. 2011, pp. 002 900–002 905, ISBN: 978-1-4244-9965-6.

[133] T. Yagi, Y. Uraoka, and T. Fuyuki, "Ray-trace simulation of light trapping in silicon solar cell with texture structures", *Solar energy materials and solar cells*, vol. 90, no. 16, pp. 2647–2656, 2006.

[134] P. P. Altermatt, G. Heiser, and M. A. Green, "Numerical quantification and minimization of perimeter losses in high-efficiency silicon solar cells", *Progress in Photovoltaics: Research and Applications*, vol. 4, no. 5, pp. 355–367, 1996, ISSN: 1099-159X.

[135] A. Goetzberger, J. Knobloch, and B. Voss, "Crystalline silicon solar cells", *Editorial John Wiley & Sons Ltd*, vol. 1, 1998.

[136] D. Macdonald, A. Cuevas, M. J. Kerr, C Samundsett, D Ruby, S Winderbaum, and A Leo, "Texturing industrial multicrystalline silicon solar cells", *Solar Energy*, vol. 76, no. 1, pp. 277–283, 2004.

[137] A. John, *Multiple internal reflection structure in a silicon detector which is obtained by sandblasting*, US Patent 3,487,223, Dec. 1969.

[138] K. E. Bean *et al.*, "Anisotropic etching of silicon", *IEEE Transactions on Electron Devices*, vol. 25, no. 10, pp. 1185–1193, 1978.

[139] D Bouhafs, A Moussi, A Chikouche, and J. Ruiz, "Design and simulation of antireflection coating systems for optoelectronic devices: Application to silicon solar cells", *Solar Energy Materials and Solar Cells*, vol. 52, no. 1, pp. 79–93, 1998.

[140] D. N. Wright, E. S. Marstein, and A. Holt, "Double layer anti-reflective coatings for silicon solar cells", in *Photovoltaic Specialists Conference, 2005. Conference Record of the Thirty-first IEEE*, IEEE, 2005, pp. 1237–1240.

[141] C. Gueymard, *Smarts2: A simple model of the atmospheric radiative transfer of sunshine: Algorithms and performance assessment*. Florida Solar Energy Center Cocoa, FL, 1995.

[142] J. Pla, J. Duran, D. Skigin, and R. Depine, "Ray tracing vs. electromagnetic methods in the analysis of antireflective textured surfaces [of solar cells]", in *Photovoltaic Specialists Conference, 1997., Conference Record of the Twenty-Sixth IEEE*, IEEE, 1997, pp. 187–190.

[143] O. Isabella, H. Sai, M. Kondo, and M. Zeman, "Full-wave optoelectrical modeling of optimized flattened light-scattering substrate for high efficiency thin-film silicon solar cells", *Progress in Photovoltaics: Research and Applications*, vol. 22, no. 6, pp. 671–689, 2014.

[144] M. Alayo, I Pereyra, and M. Carreno, "Thick sio x n y and sio 2 films obtained by pecvd technique at low temperatures", *Thin Solid Films*, vol. 332, no. 1, pp. 40–45, 1998.

[145] N. Ravindra and J Narayan, "Optical properties of amorphous silicon and silicon dioxide", *Journal of applied physics*, vol. 60, no. 3, pp. 1139–1146, 1986.

[146] E. D. Palik, *Handbook of optical constants of solids*. Academic press, 1998, vol. 3.

[147] C. Schinke, P Christian Peest, J. Schmidt, R. Brendel, K. Bothe, M. R. Vogt, I. Kröger, S. Winter, A. Schirmacher, S. Lim, *et al.*, "Uncertainty

analysis for the coefficient of band-to-band absorption of crystalline silicon", *AIP Advances*, vol. 5, no. 6, p. 067 168, 2015.

[148] S. Duttagupta, F. Ma, B. Hoex, T. Mueller, and A. G. Aberle, "Optimised antireflection coatings using silicon nitride on textured silicon surfaces based on measurements and multidimensional modelling", *Energy Procedia*, vol. 15, pp. 78–83, 2012.

[149] S. C. Baker-Finch and K. R. McIntosh, "Reflection of normally incident light from silicon solar cells with pyramidal texture", *Progress in Photovoltaics: Research and Applications*, vol. 19, no. 4, pp. 406–416, 2011.

[150] J. Rodriguez, I Tobias, and A Luque, "Random pyramidal texture modelling", *Solar Energy Materials and Solar Cells*, vol. 45, no. 3, pp. 241–253, 1997.

[151] J Renshaw and A Rohatgi, "Device optimization for screen printed interdigitated back contact solar cells", in *Photovoltaic Specialists Conference (PVSC), 2011 37th IEEE*, IEEE, 2011, pp. 002 924–002 927.

[152] M. Zanuccoli, P. Magnone, E. Sangiorgi, and C. Fiegna, "Analysis of the impact of geometrical and technological parameters on recombination losses in interdigitated back-contact solar cells", *Solar Energy*, vol. 116, pp. 37–44, 2015.

[153] M. Hermle, F. Granek, O. Schultz-Wittmann, and S. W. Glunz, "Shading effects in back-junction back-contacted silicon solar cells", in *Photovoltaic Specialists Conference, 2008. PVSC'08. 33rd IEEE*, IEEE, 2008, pp. 1–4.

[154] K. R. McIntosh, M. J. Cudzinovic, D. D. Smith, W. P. Mulligan, and R. M. Swanson, "The choice of silicon wafer for the production of low-cost rear-contact solar cells", in *Photovoltaic Energy Conversion, 2003. Proceedings of 3rd World Conference on*, IEEE, vol. 1, 2003, pp. 971–974.

[155] P. Procel, M. Guevara, V. Maccaronio, N. Guerra, F. Crupi, and G. Cocorullo, "Understanding the Optimization of the Emitter Coverage in BC-BJ Solar Cells", in *Energy Procedia*, vol. 77, Elsevier B.V., Aug. 2015, pp. 149–152.

[156] D. Giaffreda, P. Magnone, M. Meneghini, M. Barbato, G. Meneghesso, E. Zanoni, E. Sangiorgi, and C. Fiegna, "Local Shunting in Multicrystalline Silicon Solar Cells: Distributed Electrical Simulations and Experiments", *IEEE Journal of Photovoltaics*, vol. 4, no. 1, pp. 40–47, Jan. 2014.

[157] M. Guevara, P. Procel, N. Guerra, S. Pierro, V. Maccaronio, F. Crupi, and G. Cocorullo, "Numerical simulation of Back Contact-Back Junction solar cells with emitter double contact", in *2015 Fotonica AEIT Italian Conference on Photonics Technologies*, Turin, Italy, 2015, pp. 1 –4.

[158] A. Lennon, Y. Yao, and S. Wenham, "Evolution of metal plating for silicon solar cell metallisation", *Progress in Photovoltaics: Research and Applications*, vol. 21, no. 7, pp. 1454–1468, 2013.

[159] N. Zin, A. Blakers, E. Franklin, T. Kho, K. Chern, K. McIntosh, J. Wong, T. Mueller, A. G. Aberle, Y. Yang, *et al.*, "Laser-assisted shunt removal

on high-efficiency silicon solar cells", in *Proc. 27th European Photovoltaic Solar Energy Conf*, 2012, pp. 552–556.

[160] N. Zin, A. Blakers, K. R. McIntosh, E. Franklin, T. Kho, K. Chern, J. Wong, T. Mueller, A. G. Aberle, Y. Yang, *et al.*, "Continued development of all-back-contact silicon wafer solar cells at anu", *Energy Procedia*, vol. 33, pp. 50–63, 2013.

List of Publications

Peer-reviewed papers

- N. Guerra, R. De Rose, **M. Guevara**, P. Procel, M. Lanuzza, F. Crupi. "Understanding the impact of point-contact scheme and selective emitter in a c-Si BC-BJ solar cell by full 3D numerical simulations". Accepted by Solar Energy, Elesevier (2017).
- **M. Guevara**, P. Procel, R. De Rose, N. Guerra, F. Crupi, M. Lanuzza. "Design guidelines for a metallization scheme with multiple-emitter contact lines in BC-BJ solar cells". J. Comput. Electron., pp. 1–7, 2016.

Proceedings papers

- S. Pierro, P. Procel, A. Ingenito, O. Isabella, M. Zeman, **M. Guevara**, N. Guerra, F. Crupi, G. Cocorullo. "Strategies of 1D optical profile extraction for bulk Silicon solar cell simulations". EOS (European Optical Society) Topical meetings, Italy (2015).
- **M. Guevara**, P. Procel, N. Guerra, S. Pierro, V. Maccaronio, F. Crupi, G. Cocorullo. "Numerical simulation of back contact-back junction solar cells with emitter double contact". Italian Conference on Photonics Technologies, Fotonica AEIT, Torino 2015.
- P. Procel, **M. Guevara**, V. Maccaronio, N. Guerra, F. Crupi, G. Cocorullo. "Understanding the optimization of the emitter coverage in BC-BJ solar cells". Conference on 140 Crystalline Silicon Photovoltaics, Energy Procedia, Volume 77, pp. 149–152 Konstanz 2015.